

**Preparation of novel composite support materials for CO tolerant and stable anode electrocatalysts**

Thesis

Chemical Engineering Major

**Khirdakhanim Salmanzade**

Supervisor: Dr. András Tompos

Consultant: Dr. Irina Borbáth

Renewable Energy Research Group

Institute of Materials and Environmental Chemistry

Research Centre for Natural Sciences



Internal consultant: Dr. Imre Miklós Szilágyi; Associate Professor



Budapest University of Technology and Economics

Faculty of Chemical Technology and Biotechnology

Department of Inorganic and Analytical Chemistry

**2022**

## Table of Contents

|   |    |
|---|----|
| Thesis Statement .....  | 4  |
| List of abbreviations.....  | 5  |
| 1. Introduction.....  | 6  |
| 2. Literature Review.....   | 8  |
| 2.1. Fuel Cells.....  | 8  |
| 2.2. Polymer Electrolyte Membrane Fuel Cells.....   | 10 |
| 2.3. Electrocatalysts for polymer electrolyte membrane (PEM) fuel cells .....   | 12 |
| 2.3.1. State-of-the-art electrocatalysts for PEM fuel cells .....   | 12 |
| 2.3.4. $TiO_2$ -rutile-based $Ti_{(1-x)}M_xO_2-C$ ( $M$ : W, Mo) composite supported Pt catalysts: previous results .....                     | 16 |
| 3. Objectives of the study.....   | 18 |
| 4. Experimental.....  | 19 |
| 4.1. Materials used.....  | 19 |
| 4.2. Preparation of supports .....  | 19 |
| 4.2.1. Synthesis of the 75 wt.% $Ti_{(1-x)}Sn_xO_2$ - 25 wt.% C ( $x$ : 0.1-0.3) composite materials. 19                                      |    |
| 4.2.2. Synthesis of the 25 wt.% $Ti_{0.8}Sn_{0.2}O_2$ - 75 wt.% C composite materials.....  | 21 |
| 4.3. Preparation of the 20 wt.% Pt/ $Ti_xSn_{(1-x)}O_2-C$ electrocatalysts .....  | 21 |
| 4.4. Physicochemical characterization .....   | 22 |
| 4.4.1. X-Ray Power Diffraction (XRD).....   | 22 |
| 4.4.2. X-ray photoelectron spectroscopy (XPS) .....   | 23 |
| 4.4.3. Nitrogen physisorption measurements .....  | 24 |
| 4.4.4. Transmission Electron Microscopy (TEM) .....   | 24 |
| 4.4.5. Scanning Electron Microscopy (SEM) .....   | 24 |
| 4.4.6. Raman spectroscopic measurements .....   | 24 |
| 4.4.7. Inductively coupled plasma - optical emission spectrometry (ICP-OES) .....   | 24 |
| 4.5. Electrochemical Characterization .....   | 25 |
| 4.5.1. Cyclic Voltammetry (CV).....   | 25 |
| 4.5.2. Characterization by $CO_{ads}$ -stripping voltammetry .....  | 27 |
| 4.5.3. Stability test .....   | 27 |
| 4.5.4. Characterization by rotating disk electrode (RDE) technique .....  | 28 |
| 5. Results and Discussion .....   | 30 |
| 5.1. Route A - physicochemical characterization of the $Ti_{(1-x)}Sn_xO_2-C$ composite support materials and related Pt electrocatalysts..... | 30 |

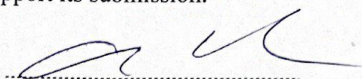
|        |  |    |
|--------|--|----|
| 5.1.1. | <i>Powder X-ray diffraction (XRD) investigations</i> .....   | 30 |
| 5.1.2. | <i>Nitrogen physisorption measurements</i> .....   | 31 |
| 5.1.3. | <i>Transmission electron microscopy (TEM) analysis</i> .....   | 32 |
| 5.1.4. | <i>SEM/EDX measurements</i> .....  | 37 |
| 5.1.5. | <i>Raman spectroscopy measurements</i> .....   | 41 |
| 5.1.6. | <i>X-ray photoelectron spectroscopy (XPS) examination</i> .....  | 42 |
| 5.2.   | <i>Route A - electrochemical characterization of the 20 wt.% Pt/Ti<sub>(1-x)</sub>Sn<sub>x</sub>O<sub>2</sub>-C electrocatalysts</i> .....                                 | 45 |
| 5.3.   | <i>Route B - physicochemical characterization of the Ti<sub>(1-x)</sub>Sn<sub>x</sub>O<sub>2</sub>-C composite support materials and related Pt electrocatalysts</i> ..... | 49 |
| 5.3.1. | <i>X-ray powder diffraction (XRD)</i> .....  | 49 |
| 5.3.2. | <i>Nitrogen physisorption measurements</i> .....   | 51 |
| 5.3.3. | <i>Transmission electron microscopy (TEM) analysis</i> .....   | 52 |
| 5.3.4. | <i>SEM/EDX measurements</i> .....  | 54 |
| 5.3.5. | <i>X-ray photoelectron spectroscopy (XPS) examination</i> .....  | 58 |
| 5.4.   | <i>Route B - electrochemical characterization of the 20 wt.% Pt/Ti<sub>(1-x)</sub>Sn<sub>x</sub>O<sub>2</sub>-C electrocatalysts</i> .....                                 | 60 |
| 5.5.   | <i>Electrochemical performance of the 20 wt.% Pt/Ti<sub>(1-x)</sub>Sn<sub>x</sub>O<sub>2</sub>-C electrocatalysts in the HOR and the ORR</i> .....                         | 63 |
| 6.     | <i>Summary</i> .....   | 67 |
|        | <i>Acknowledgements</i> .....  | 69 |
|        | <i>References</i> .....  | 70 |

## Thesis Statement

### Statement of the internal supervisor

I, Dr. Szilágyi Imre Miklós as internal supervisor, hereby declare that the thesis written by Khirdakhanim Salmanzade, (Neptune code: ERXE3V) titled 'Preparation of novel composite support materials for CO tolerant and stable anode electrocatalysts' is his/her own writing and that I supported his/her work with regular consultations. I also declare that the thesis meets the formal and professional requirements of the Budapest University of Technology and Economics and those of the Faculty of Chemical Technology and Biotechnology, thus I support its submission.

(Date and place)  
Budapest, 2022.05.27

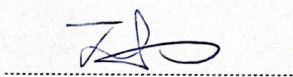


(supervisor, internal)

### Statement of the external supervisor

I, Dr. András Tompos as external supervisor, hereby declare that the thesis written by Khirdakhanim Salmanzade, (Neptune code: ERXE3V) titled Preparation of novel composite support materials for CO tolerant and stable anode electrocatalysts is his/her own writing prepared under my supervision. Based on its professional merits, I support its submission.

(Date and place)  
Budapest, 2022.05.27



(supervisor, external)

### Statement of the student

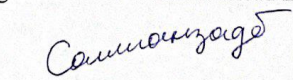
I, Khirdakhanim Salmanzade (Neptun code: ERXE3V) as author of the thesis hereby declare that my thesis titled 'Preparation of novel composite support materials for CO tolerant and stable anode electrocatalysts' is my original writing and I have not plagiarised any other work. All third party materials including published and unpublished sources were referenced.

I acknowledge that the intellectual property rights of the methods used and the results of any research or development described in the thesis belong to the participating researchers and institutions/companies, thus their utilization or publication must not be initiated before the approval of all parties.

I also declare that during the preparation and writing the thesis I did not mislead my supervisor(s) and thesis advisor.

(Date and place)

2022.05.27



(student)

## List of abbreviations

|                   |  |
|-------------------|--|
| <b>AFC</b>        | <b>Alkaline Fuel Cell</b>  |
| <b>BET</b>        | <b>Brunauer–Emmett–Teller</b>  |
| <b>BP</b>         | <b>Black Pearls 2000</b>   |
| <b>CV</b>         | <b>Cyclic Voltammetry / Cyclic Voltammogram</b>                                |
| <b>CNF</b>        | <b>Carbon Nanofibers</b>   |
| <b>DMFC</b>       | <b>Direct Methanol Fuel Cells</b>  |
| <b>ECSA</b>       | <b>Electrochemical Surface Area</b>  |
| <b>EDX</b>        | <b>Energy Dispersive X-ray</b>   |
| <b>EW</b>         | <b>Equivalent Weight</b>   |
| <b>FCEV</b>       | <b>Fuel Cell Electric Vehicle</b>  |
| <b>HOR</b>        | <b>Hydrogen Oxidation Reaction</b>   |
| <b>HTT</b>        | <b>High-Temperature Treatment</b>  |
| <b>ICP-OES</b>    | <b>Inductively Coupled Plasma - Optical Emission Spectrometry</b>              |
| <b>LPG</b>        | <b>Liquefied Petroleum Gases</b>   |
| <b>MA</b>         | <b>Mass Activity</b>   |
| <b>MCFC</b>       | <b>Molten-Carbonate Fuel Cell</b>  |
| <b>NHE</b>        | <b>Normal Hydrogen Electrode</b>   |
| <b>HAADF-STEM</b> | <b>High-Angle Annular Dark-Field Scanning Transmission Electron Microscopy</b> |
| <b>ORR</b>        | <b>Oxygen Reduction Reaction</b>   |
| <b>PAFC</b>       | <b>Phosphoric Acid Fuel Cell</b>   |
| <b>PEM</b>        | <b>Polymer Electrolyte Membrane</b>  |
| <b>PEMFC</b>      | <b>Polymer Electrolyte Membrane Fuel Cell</b>                                  |
| <b>PFSA</b>       | <b>Perfluorosulfonic Acid</b>  |
| <b>PTFE</b>       | <b>Polytetrafluoroethylene</b>   |
| <b>RDE</b>        | <b>Rotating Disk Electrode</b>   |
| <b>RHE</b>        | <b>Reversible Hydrogen Electrode</b>   |
| <b>RT</b>         | <b>Room Temperature</b>  |
| <b>SAED</b>       | <b>Selected Area Electron Diffraction</b>                                      |
| <b>SMSI</b>       | <b>Strong Metal-Support Interaction</b>  |
| <b>SOFC</b>       | <b>Solid Oxide Fuel Cells</b>  |
| <b>SSA</b>        | <b>Specific Surface Area</b>   |
| <b>STEM</b>       | <b>Scanning Transmission Electron Microscopy</b>                               |
| <b>TEM</b>        | <b>Transmission Electron Microscopy</b>  |
| <b>WE</b>         | <b>Working Electrode</b>   |
| <b>XPS</b>        | <b>X-Ray Photoelectron Spectroscopy</b>  |
| <b>XRD</b>        | <b>X-Ray Powder Diffraction</b>  |

## 1. Introduction

Every year, the world's population and industries expand dramatically. As a result, one of the major problems today is to fulfil humanity's ever-increasing energy demands to the maximum degree feasible using renewable energy sources. Solar energy, wind energy, and geothermal energy are just a few of the examples that may be given. However, the availability of all of these renewable energy types varies around the world depending on the climate of the region, such as coastal areas, the tops of rounded hills, open plains, and gaps in mountains - places where the wind is strong and reliable - or the time of year, such as solar energy is not effective in the winter but is effective in the summer, and so on. As a result, the sources of renewable energy and its applications are frequently separated in distance and time.

Converting renewable energy to chemical energies might be one answer to this challenge. Secondary energy sources can be stored and delivered in this manner. Hydrogen is a possible energy carrier because of its high gravimetric energy density, abundance, and storage potential [1]. For such applications, hydrogen can be produced by electrolysis of water utilizing electricity obtained from renewable primary energy sources. On the other hand, hydrogen may be converted into electrical energy in high-efficiency fuel cells as needed. Consequently, hydrogen has the potential to be one of the most promising fuels for the future since it can be produced and used in a clean, ecologically acceptable manner.

Conventional production of hydrogen is steam reforming of methane [2]. The steam reforming process converts hydrocarbons (from natural gas and LPG to liquid fuels such as naphtha and, in some cases, kerosene) into hydrogen, carbon oxides, methane, carbon monoxide, and unconverted steam mixture as main products, and methane, carbon monoxide, and unconverted steam mixture as by-products [3]. As a result, on-site natural gas reforming might be a viable option for fuelling Fuel Cell Electric Vehicles (FCEVs) at filling stations. The key obstacles of this technique are high capital expenditures, high operating and maintenance expenses, and design for production. Because the purity of hydrogen intended for use as a fuel in fuel cells is critical in order to avoid poisoning the platinum-based catalyst of the cell, the produced hydrogen output must be of high purity, or additional purification processes, particularly to remove carbon monoxide, must be integrated [2].

Fuel cells come in a variety of sizes and powers, ranging from small devices that produce a few watts to massive power plants that generate MWs of energy. The design of all fuel cells is the same: two electrodes separated by a solid or liquid electrolyte allowing ion exchange between the cathode and anode. A catalyst is also employed to improve the reactions that take place on the electrodes. Different types of fuel cells can be utilized depending on the purpose and amount of energy to be produced, and they are mostly categorized based on the electrolyte used. Depending on the application, different materials and designs are required for different types of fuel cells.

Fuel cells using Polymer Electrolyte Membrane (PEM) membranes may play a particularly important role among fuel cells due to their small size, low operating temperature, and quick start-up. However, at the moment the PEM fuel cell technology is not cheap, thus improvement in individual fuel cell components, such as in electrocatalysts, is required to optimize the costs, the environmental sustainability and the equipment longevity. If the PEM fuel cell technology competes with other technologies in both price and technical performance, it is expected to play a large role in the market.

Platinum catalysts are used in PEM fuel cells, and their cost is a considerable part of the overall production expenses [4]. Currently, PEM fuel cells employ commercially available platinum catalysts with carbon support. Despite the fact that the amount of platinum used has decreased significantly over the last decade, one area of research and development is to lower the amount of platinum utilized (up to zero, by developing platinum-free electrodes [5]). Improvement of the stability and longevity of catalysts and electrodes generated from them is also at the heart of the advancements. According to the

research, enhancing the stability of the catalyst support is the most effective way to increase electrode stability.

The carbon-based support provides good conductivity but is prone to corrosion, particularly when the electrode's potential swings owing to fast load changes (for example, during operation of a vehicle). Another problem to be handled is the anode catalyst's carbon monoxide sensitivity because of the tendency of platinum towards poisoning by CO. Because a large portion of the hydrogen utilized as fuel still comes from the reforming of hydrocarbons, which invariably includes carbon monoxide, another crucial element of catalyst development is the search for CO-tolerant anode-side catalysts.

The Renewable Energy Research Group (hereinafter: research group) at the Institute of Materials and Environmental Chemistry of the Research Centre of Natural Sciences is striving to answer these issues, and I am contributing my master's thesis to this effort.

## 2. Literature Review

### 2.1. Fuel Cells

Fuel cells are electrochemical devices that consist of an electrolyte and two electrodes and whose primary function is to convert hydrogen, or other readily convertible fuels, to electrical energy through an electrochemical process. The negative electrode, where hydrogen is oxidized (anode), and the positive electrode, where oxygen is reduced (cathode), are the two electrodes separated by an electrolyte, which can be liquid or solid. The only by-products of the process are heat, carbon dioxide (if a hydrocarbon or methanol is used as a fuel), and water, hence there are no negative environmental consequences. The cell's fuel consumption may be adjusted dynamically based on the load. A single fuel cell produces around 0.6 V voltage at a current density of around 2-3 A/cm<sup>2</sup>, however when the cells are coupled in series, larger voltages can be generated [6].

A variety of fuel cells can exist depending on certain characteristics. These variables include: the kind and nature of the fuel utilized; the operating temperature; and whether the fuel cell is processed outside (external reforming) or inside (internal reforming).

However, the most common classification (see Figure 1) is based on the electrolyte utilized in the fuel cell:

- Solid Oxide Fuel Cells (SOFC);
- Direct Methanol Fuel Cells (DMFC);
- Alkaline Fuel Cells (AFC);
- Phosphoric Acid Fuel Cells (PAFC);
- Molten Carbonate Fuel Cells (MCFC);
- Proton Exchange / (Polymer Electrolyte) Membrane Fuel Cells.

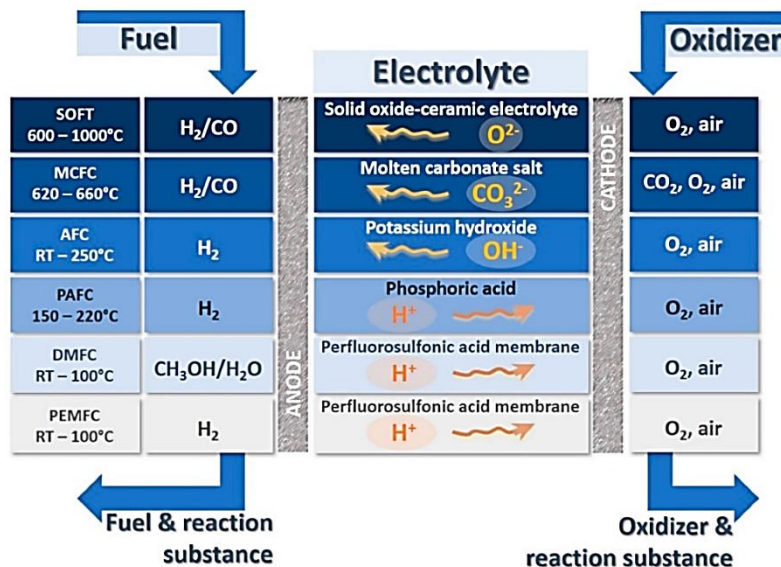


**Figure 1.** Classification of fuel cells based on the type of the electrolyte employed [7]

Internal combustion engines and batteries are commonly used to compare fuel cell systems with other energy converting equipment utilizing chemical energy. Fuel cells provide certain benefits over the technologies outlined above, but they also have significant drawbacks.

The efficiency of fuel cells over heat engines is one of their most significant benefits. The difference between the inlet and outlet temperatures of a combustion engine is connected to its thermodynamic efficiency; however, the inlet temperature is restricted by material considerations in the system, and the output temperature is ambient temperature, which also limits the engine efficiency. Because fuel cells do not rely on combustion, their efficiency is unrelated to their maximum working

temperature. As a result, their power conversion efficiency may be much greater. Figure 2 compares the overall system efficiency characteristics of fuel cells to those of other electric power generation systems.

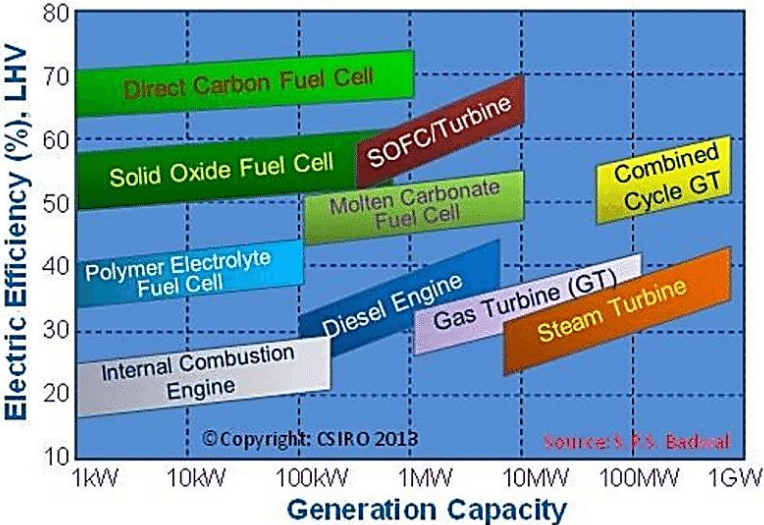


Figure 2. Power Generating Systems Efficiency Comparison [8]

In addition to electrical power, fuel cell systems produce clean hot water and medium-grade heat, both of which can potentially be used in co-generation applications such as domestic or industrial applications. This kind of coupling of different power generation routes can also heighten the overall efficiency of the system [9].

When compared to heat engines, fuel cells or batteries are more suited for electric energy generation rather than mechanical energy generation (Figure 3).

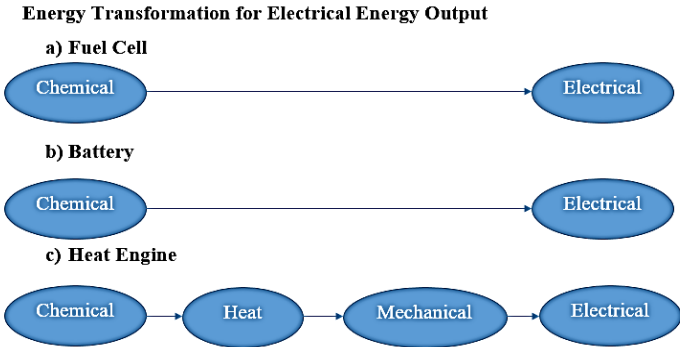


Figure 3. Comparative energy transformations in (a) fuel cells, (b) batteries and (c) heat engines for generation of electrical energy [9]

When compared to batteries, one advantage of fuel cell devices is that they do not require recharging. The hydrogen storage tank connected to fuel cell, on the other hand, must be refuelled, which is a faster process than charging a battery. Furthermore, depending on the size of the storage tank, this functionality can extend the application's range [9].

Fuel cells that use hydrogen as a fuel have additional advantages in that they do not emit pollutants; the only byproducts are clean water and heat. Some toxic emissions can be produced by

fuel cells that run on hydrogen-rich reformat gas combinations, although they are substantially lower than those produced by internal combustion engines that run on traditional fossil fuels.

PEMFCs and DMFCs are two types of fuel cells that function at low temperatures. These fuel cells are particularly well suited to low-temperature devices. Low-temperature operation cuts warm-up time in half, eliminates high-temperature risks, and improves the thermodynamic efficiency of the electrochemical process.

## 2.2. Polymer Electrolyte Membrane Fuel Cells

The PEM fuel cell technology is the most often utilized technology nowadays. It was the first form of fuel cell to be used as a source of transportation power, small-scale power generation, and portable electricity. The fundamental feature that distinguishes PEMFC from other types of fuel cells is the presence of a solid proton conducting electrolyte. The following qualities of PEMFC can be identified as its advantages: its ability to run at low temperatures (303°K -353°K); generation of a high specific power (ca. 2-3°kW/kg) and high power density (ca. 2-3 kW/dm<sup>3</sup>); quick start up. The PEMFC's sensitivity to fuel contaminants, on the other hand, is a drawback [6]. Considering these features, transportation is the primary application sector for PEM fuel cells due to their high power density, light weight compact structure, higher sensitivity characteristic, rapid start-up process, small size, lack of maintenance requirements, and lack of greenhouse gas emissions to the atmosphere when compared to other types of fuel cells [10-12].

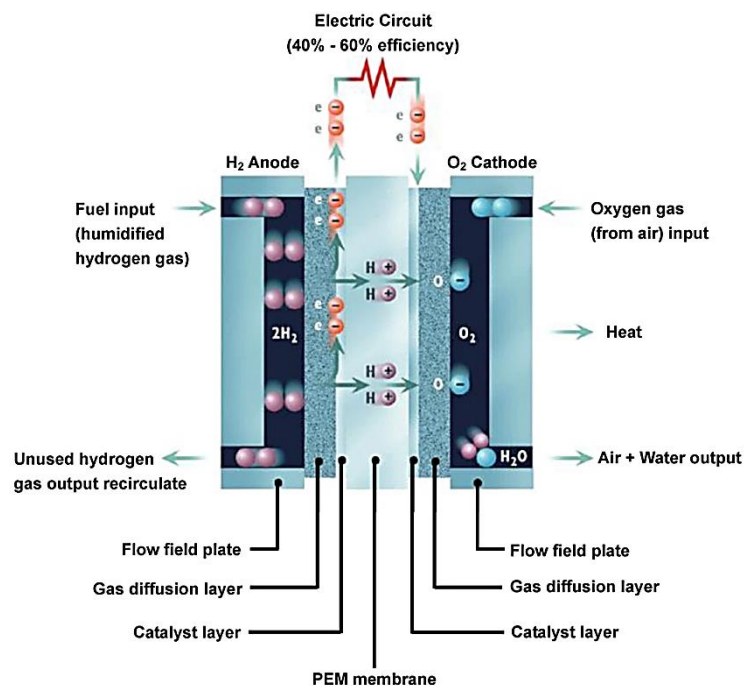


**Figure 4.** Cross-sectional view of polymer electrolyte membrane fuel cell [13]

A proton containing membrane is an important part of a PEMFC because it allows protons to travel between the two electrodes while preventing electron and gas transmission (see Fig. 4). Protons diffuse from the anode to the cathode via this solid, thin (~25°µm) membrane. The following compounds can be used as examples for these membranes [6]:

- a) Polystyrene sulfonic acid: excellent proton conductivity and good water absorption capacity;
- b) Phenolic membranes (polymerization of phenol-sulfonic acid with formaldehyde): mechanically unstable membranes;

- c) Partly sulfonated polystyrene sulfonic acid (sulfonated at room temperature after dissolving polystyrene sulfonic acid in ethanol-stabilized chloroform): brittle in the dry state;
- d) Perfluorosulfonic acid (PFSA) is often utilized nowadays.

The PFSA can be divided into three sections, which are: a polytetrafluoroethylene (PTFE, a.k.a. DuPont's Teflon™)-like backbone;  $-O-CF_2-CF-O-CF_2-CF_2-$  side-chains that connect the molecular backbone to the third area and the sulfonic acid ion clusters.

The following are the two key benefits of PFSA membranes for usage in PEMFC:

- PFSA membranes are robust and durable in both oxidative and reductive conditions (durability up to 60 000 h has been observed) [14], thanks to the PTFE backbone.
- At fuel cell working temperatures, the protonic conductivities attained in a well-humidified PFSA membrane can be high (up to 0.2 S/cm) [6].

PFSA membranes, on the other hand, have several drawbacks:

- The most significant disadvantage of PFSA in PEMFCs is its high cost, which is due to the costly fluorination step and lengthy preparation period required for PFSA membrane manufacture (~ US\$ 700/m<sup>2</sup>; thus, for a PEMFC operating at the desired power density of about 0.6 W/cm<sup>2</sup>, the cost of just the membrane will be around US\$ 120/kW) [15].
- Other downsides of PSFA membranes include expense, safety concerns, supporting equipment requirements, and temperature-related limits (toxic and corrosive gases liberated at temperatures above 423 K).

DuPont's Nafion® polymer membrane is now the most extensively used polymer membrane (see Figure 5). Nafion fits this role well because it meets at least in part the numerous requirements such as good proton conduction, electrical insulation, thermal, mechanical, and chemical stability. Typically the Nafion membrane separates the electrodes loaded by platinum-based catalysts, although in many recent projects the catalysts are deposited on the proton conducting membrane [6,10,11].

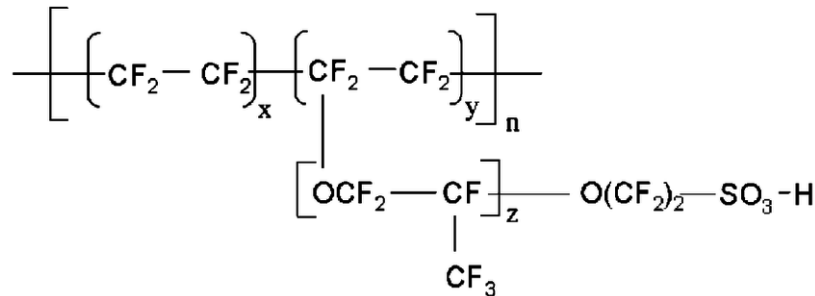


**Figure 5.** Polymer Structure of Nafion® (perfluorosulfonic acid) [16]

The hydrogen is supplied to the anode side of the hydrogen polymer electrolyte membrane fuel cell, where it is oxidized. Protons and electrons are formed as a result of oxidation. Protons go through the ionic conductor, whereas electrons travel to the cathode side through an external circuit. The injected oxygen is reduced by the electrons on the cathode side, resulting in the production of water [17]. The chemical processes that take place at each electrode (hydrogen oxidation in anode and oxygen reduction in cathode); as well as the total redox reaction are demonstrated in equations (1), (2), and (3) [6,11,12,18,19]:



The electrocatalyst's job is to promote electrocatalytic reactions on both the anode and cathode sides. In order to construct a stable, effective catalyst, the conditions within the cell should be addressed while creating catalysts.

### ***2.3. Electrocatalysts for polymer electrolyte membrane (PEM) fuel cells***

Platinum catalysts are supported on activated carbon in the most typical PEM fuel cells. The support must be electrically conductive, have a large enough specific surface area, be stable in the pH and potential ranges employed, and have a porous structure that allows the catalyst to touch the fuel or oxidant and release reaction products [20]. Another prerequisite is for the active metal nanoparticles and the support to form a strong bond. Platinum is the most significant component of the catalysts since it is a noble metal with the highest catalytic activity in hydrogen oxidation and oxygen reduction processes [21,22] under PEM fuel cell conditions. It is critical that the precious metal be evenly spread over the support surface, since this will increase the catalyst's activity. Researchers must work to minimize the cost of the electrocatalyst by reducing the amount of Pt in it and by increasing the utilization of Pt [23]. Increasing the dispersion of Pt nanoparticles and their stabilization on a correctly selected support is one of the most promising ways to achieve this aim.

#### ***2.3.1. State-of-the-art electrocatalysts for PEM fuel cells***

An optimal anode and cathode electrocatalysts should be highly active both in hydrogen oxidation and oxygen reduction, respectively, and should also have good long-term stability and adequate electrical conductivity at an affordable price. At present, Pt/C catalysts represent the most widespread choice for PEM fuel cells even if they are prone to electrocorrosion under the working conditions of the cell, especially during start/stop cycles. Corrosion results in either Pt dissolution or oxidation of the carbon support leading to detachment, Ostwald ripening and agglomeration of platinum nanoparticles [10,24,25]. Moreover, the presence of Pt nanoparticles could also accelerate the corrosion of carbon [26]. The consequence of both processes is the loss of the active surface of the catalysts. In practice this activity loss is compensated by very high Pt loadings.

It should be noted that at potentials encountered in normal PEM fuel cell operation (0.6–0.9 V) the kinetics of the support oxidation is sluggish, while under dynamic processes, such as start-up and shut down, it is accelerated as a direct consequence of high potential values reached by the cathode, for example due to local fuel starvation ( $\geq 1.2$  V) [27].

Another problem of the traditional Pt/C catalysts is their sensitivity to carbon monoxide poisoning, which renders reformed hydrogen fuel unsuitable for PEM cells without further purification [28]. Thus, although carbon black supported Pt catalysts are commercially available in large quantities with reliable quality, it is important to explore alternative materials that can provide improved stability and increased CO tolerance.

Recent investigations suggest that some of the CO-poisoning-related issues of the Pt/C electrocatalysts recommended for PEM fuel cells can be overcome by applying a second oxophilic surface metal. In general, reactive hydroxyl species form more easily on the oxophilic additive than on Pt, which not only enhances the reaction rate at the anode [29,30] but is also beneficial in the much slower process at the cathode [31,32], and also facilitates easy oxidation of the CO contaminant via the so-called bifunctional mechanism [33,34], supposed that an intimate contact between the oxophilic sites and Pt is ensured. Since numerous studies have shown that ruthenium is one of the best promoter [35], the state-of-the-art commercial CO-tolerant electrocatalyst, containing Pt-Ru alloy nanoparticles on active carbon support, is also commercially available. By incorporating ruthenium into platinum,

alloy catalysts are found to be very active and tolerant to CO poisoning at lower potentials, owing to introduced beneficial electronic and geometric effects [36-40].

Although reducible oxides of oxophilic metals are indeed valuable co-catalysts or supports for PEM fuel cell electrocatalysts, their dissolution under the working conditions of the cell is always a concern, as dissolved metal cations can absorb in the polymer membrane, resulting in the loss of its proton conducting property [41]. The leaching problems may be avoided by using the oxide of the oxophilic component as support or support modifier, if it is stable in the expected potential window. Indeed, ruthenium oxides are electrochemically stable within the hydrogen and oxygen evolution region compared to Ru metal, which is irreversibly oxidized at potentials higher than 0.8 V vs. RHE [20]. It has been demonstrated that under certain fuel cell operating conditions (e.g., during an air/air start-up/shut down or fuel starvation) the Ru instability is greatly increased when the anode potential rises above the Ru dissolution limit of ~450 mV vs. RHE [42]. The crossover of dissolved Ru through the membrane and further deposition at the cathode Pt catalyst suppresses the rate of the cathode oxygen reduction reaction (ORR) by blocking Pt sites, and it can also promote a faster oxidation and de-activation of the cathode catalyst [43].

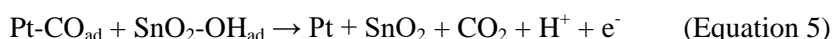
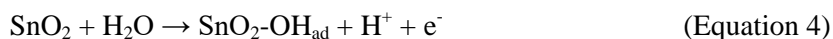
In addition, since the price of the widely used Pt/C catalyst is a significant part of the cost of fuel cell devices (roughly 40%), it is very important to reduce the Pt content and to decrease the corrosion of the active metal [4]. In order to achieve these goals, the development of the novel support materials seems to be one of a useful tool. The recent advances on this aspect are presented further.

### 2.3.2. Application of metal oxides as electrocatalyst supports

One of the key research questions in this area is the choice of new types of electrocatalysts that can replace commercial carbon black supported Pt-based catalysts in fuel cell both on the anode and cathode sides, and what properties the new materials can provide.

Therefore, it would be desirable to use more stable carbon-free metal oxide-based supports to improve the stability of the catalyst. As a consequence, numerous studies have been carried out to develop metal oxides (e.g., TiO<sub>2</sub> [44,45], WO<sub>3</sub>/WO<sub>x</sub> [46-49], MoO<sub>x</sub> [31,50-51] and SnO<sub>2</sub> [52-54]) with high resistance to corrosion as potential support materials for electrocatalysts, which, in addition, can act as co-catalysts to enhance the catalytic activity.

Among transition metal oxides, the catalytic function of SnO<sub>2</sub> is attracting the interest of researchers. Tin oxide is usually regarded as oxygen deficient n-type semiconductor [55-57]. Moreover, it has good corrosion resistance in acidic media and thus is expected to be stable under the working conditions of PEM fuel cells. It also has the ability to adsorb OH species at low potentials, which can potentially suppress CO poisoning based on the bifunctional mechanism as shown in the Eqns. (4) and (5) [20,58-59]:



The increase in the catalytic activity attributed to the decrease of poisoning effect, which resulted from synergic effects of the metal oxide-platinum nanoparticles composites, and the ability of the oxide to induce electronic effect with Pt have make it possible to consider SnO<sub>2</sub> as a promising support for fuel cell electrocatalysts [20,60]. It was revealed in Ref. [61] by CO pulse titration that the SnO<sub>2</sub>-containing catalysts adsorbed CO more weakly than the other catalysts without SnO<sub>2</sub> nanoparticles. This phenomenon was derived from the interaction between active metal atoms (Pt or Pd) and SnO<sub>2</sub> nanoparticles, since these catalysts mixed with carbon did not exhibit intermetallic compounds. It has

been proposed [62] that the interaction between platinum and tin oxide in Pt/SnO<sub>2</sub> catalysts became stronger as the Pt particle density decreased.

Due to the strong interaction between Pt and SnO<sub>2</sub>, the electrochemical stability of Pt/SnO<sub>2</sub> is generally greatly improved over commercial Pt/C catalysts, while exhibiting similar catalytic activity to that of Pt/C [63,64]. It has been reported by Masao *et al.* [65] that Pt electrocatalysts supported on semiconducting SnO<sub>2</sub> had significant tolerance against potential cycling up to +1.3 V vs. RHE even after 10,000 cycles. This carbon-free Pt/SnO<sub>2</sub> catalyst exhibited current-voltage characteristics comparable to conventional Pt electrocatalysts and significant long-term stability against voltage cycling up to higher potentials, which is a possible fundamental solution to the problem of PEM fuel cell degradation caused by carbon support corrosion.

It has been demonstrated by Cs-corrected STEM coupled with geometric phase analysis [66] that Pt formed spheroidal nanoparticles on carbon, whilst Pt hemispheres were formed on SnO<sub>2</sub> due to the strong metal-support interaction (SMSI). The variation in lattice parameter in the Pt/SnO<sub>2</sub> system was significantly higher than that in Pt/C, especially near an atomic step in the SnO<sub>2</sub> terrace. It was shown by DFT analysis that the activation energy for oxygen dissociation was decreased when the Pt surface is under strain. These results suggest that it will be possible to tailor catalytic activity by taking advantage of the SMSI between platinum and metal oxides.

It has been demonstrated [67] that SnO<sub>2</sub> nanocluster with parallel nanorods synthesized via a hard template method can be considered as a promising alternative anode catalyst support for PEM fuel cells. Electrochemical measurements showed that Pt/SnO<sub>2</sub> exhibited significantly enhanced electrochemical stability than Pt/C under high potential electrooxidation and potential cycling. The Pt/SnO<sub>2</sub> catalyst reserved most of its electrochemically active surface area (ECSA) under 10 h potential hold at 1.6 V while its ECSA degradation rate was one order of magnitude lower than Pt/C under potential cycling between 0.6 and 1.2 V.

Okanishi *et al.* [68] investigated the adsorption and catalytic properties of Pt/SnO<sub>2</sub> as a model system undergoing strong chemical interaction when subjected to oxidation-reduction treatments. The reduced nanoparticles reportedly existed in a core-shell structure with Pt in the core enveloped in the oxide shell. The study also identified that the Pt/SnO<sub>2</sub> system is highly sensitive to the reduction-oxidation atmosphere and the surface is reversibly converted between two states, namely the between "Pt + tin oxide" and the "Pt-Sn intermetallic compound" states.

Unfortunately, it should be noted that replacing carbon with traditional metal oxides is difficult, due to their low electric conductivity. Typically, methods for improving the electronic conductivity of metal oxides are as follows: (i) reducing pure oxide by producing oxygen vacancies, (ii) introducing an appropriate dopant by cation substitution, (iii) adding conducting materials (e.g., active carbon).

The simplest and most frequently used method for increasing the conductivity of oxide-based supported catalysts is both their mixing with carbon powder [69] and the preparation of carbon-containing oxide-based (e.g., SnO<sub>2</sub>-based [70-78] and TiO<sub>2</sub>-based [79-84]) composite support materials. Thus, it was demonstrated [85] that a promising composite support material based on electrically conductive carbon nanofibers (CFs) decorated with non-conductive stabilizing SnO<sub>2</sub> provides high catalyst stability to the SnO<sub>2</sub>/Pt/CFs electrocatalyst.

However, the most attractive new oxide-type support materials are sub-stoichiometric metal oxides, such as reduced oxidation state titania (e.g., Ti<sub>4</sub>O<sub>7</sub> and Ebonex), nanostructured metal oxides, such as SnO<sub>2</sub> nanowires [86] and nanofibers [87,88], and doped metal oxides such as doped TiO<sub>2</sub> and SnO<sub>2</sub>, which have been proposed as electrically conductive support materials with high corrosion-resistant properties [60]. Among the listed methods for improving electrical conductivity, the most widespread is the introduction of an appropriate dopant by cationic substitution, assuming that doping does not radically change the chemical stability of the host lattice. Based on metal-doped oxide, which can be both electrically conductive and kinetically stable under fuel cell conditions, a novel class of

electrocatalysts has been developed for use in fuel cells, including Pt supported on different transition metals (M)-doped TiO<sub>2</sub> (M: W [89], Mo [90,91], Nb [92-94], Ta [95,96], Sn [97], etc.), M-doped SnO<sub>2</sub> (M: In [98,99], Sb [100-102], Ru [103], Al [104-106], Nb [107,108], Zn [109], etc.), Sn-doped CeO<sub>2</sub> [110], etc. These catalysts are developed to overcome the inherent limitations of the traditional active carbon-supported Pt catalysts.

### 2.3.3. Sn-doped TiO<sub>2</sub>: properties and use as support for PEM fuel cells

Titania and tin oxide have attracted extensive attention as promising support materials for fuel cell applications. In this regard, the combination of these oxides in Ti-Sn mixed oxide composite materials can be very interesting from many points of view. Well-established sensing properties of SnO<sub>2</sub> for reducing gases, combined with the good chemical stability of TiO<sub>2</sub> at high temperatures, stimulate the research on the application of TiO<sub>2</sub>-SnO<sub>2</sub> solid solutions, for example, in gas detection [111].

To overcome the leaching of oxophilic metals in acidic electrolyte, a composite support is proposed, in which the co-catalyst metal can be stabilized by substitution into the rutile phase titanium-dioxide lattice.

Ti<sub>0.7</sub>Sn<sub>0.3</sub>O<sub>2</sub> nanoparticles NPs with high surface area of 125.7 m<sup>2</sup>/g and electronic conductivity of about 1.07×10<sup>-4</sup> S/cm, which is significant higher than that of the undoped TiO<sub>2</sub> NPs (1.42×10<sup>-7</sup> S/cm), were successfully used as the cathode catalyst support for oxygen reduction reaction (ORR) in PEM fuel cells [97]. Compared with the Pt/C (C: Vulcan XC-72), the Pt/Ti<sub>0.7</sub>Sn<sub>0.3</sub>O<sub>2</sub> catalyst shows excellent stability under both high potential hold (at 1.4 V for 10 h) and potential cycling between 0.6 and 1.2 V vs. NHE.

In Ref. [112] Sn/Ti ratios in the Ti<sub>1-x</sub>Sn<sub>x</sub>O<sub>2</sub> (x: 0.1-0.3) solid-solution and Ti<sub>1-x</sub>Sn<sub>x</sub>O<sub>2</sub>/C (C: Vulcan XC-72) ratios in hybrid Ti<sub>1-x</sub>Sn<sub>x</sub>O<sub>2</sub>-C support materials were systematically optimized in terms of their performance as supports for methanol oxidation. The best characteristics were obtained on the 20 wt.% Pt/Ti<sub>0.9</sub>Sn<sub>0.1</sub>O<sub>2</sub>-C electrocatalyst, which exhibits higher activity and durability compared to Pt/TiO<sub>2</sub>-C and commercial Pt/C. It is well known that the electrical conductivity of the catalyst decreases with an increase of oxide content in the support. However, if the content of oxide in the support was too low, the promotional role of the Ti<sub>0.9</sub>Sn<sub>0.1</sub>O<sub>2</sub> was not observed. Due to the balance, the Pt catalysts supported on the support with a Ti<sub>0.9</sub>Sn<sub>0.1</sub>O<sub>2</sub>/C= 30/70 ratio exhibited the highest methanol electrooxidation activity.

In principle, the poisoning of Pt catalysts by CO-like intermediates produced during the methanol electrooxidation process is the main reason that leads to sluggish methanol oxidation. It should be emphasized that although OH groups exist on both TiO<sub>2</sub> and Ti<sub>0.9</sub>Sn<sub>0.1</sub>O<sub>2</sub> surface, doping of Sn element into TiO<sub>2</sub> is able to significantly increase the concentration of absorbing oxygen groups on the oxide surface. In the literature [113,114], this was explained by the fact that the promotion mechanism is associated with a more favourable thermodynamic formation of SnO<sub>2</sub> compared to TiO<sub>2</sub>. The richness of OH groups resulting from Sn<sup>4+</sup> doping will therefore likely facilitate the oxidation of poisoning CO intermediates absorbed on Pt sites, thereby significantly promoting the methanol electrooxidation reaction according to the well-known bifunctional mechanism [115,116]. Thus, it is not surprising that the catalytic activity of Pt/Ti<sub>0.9</sub>Sn<sub>0.1</sub>O<sub>2</sub>-C with respect to methanol oxidation is higher than that of Pt/TiO<sub>2</sub>-C.

It is important to note that the successful Sn doping into the TiO<sub>2</sub> lattice with a replacement of the Ti<sup>4+</sup> position led to a phase transition from anatase to rutile for TiO<sub>2</sub> samples. In turn, this also provides indirect evidence of Sn doping into TiO<sub>2</sub> [117,118].

In the literature there are numerous variants of methods for obtaining Sn-doped TiO<sub>2</sub> materials by the sol-gel [119-123], co-precipitation [124], solvothermal synthesis method [125], mechanochemical synthesis [126,127], the citric acid complexing method [128], plasma-enhanced chemical vapor deposition [129], template-based liquid phase deposition method [130] and fluoride-mediated

chemically induced self-transformation strategy [131]. Upon preparation of tin-containing materials by sol-gel synthesis  $\text{SnCl}_2 \times 2\text{H}_2\text{O}$  is often used as tin precursor compound. However, the use of oxalate is also recommended in the literature, since oxalate is a low molecular weight organic salt with carboxyl groups, which can be easily removed by calcination at a lower temperature, especially in a thin film process (e.g., in the synthesis of  $\text{SnO}_2$  nanowires (see Refs. [132,133])).

The sol-gel synthesis of linear Sn-doped  $\text{TiO}_2$  nanostructures with high aspect ratios resulting in the formation of nanofibers upon calcination was reported in Ref. [134]. The molecular intermediates that form during the early stages of the reaction were monitored using electrospray-ionization mass spectrometry to confirm the presence of metal-oxide clusters containing both Sn and Ti ions. These intermediates then undergo polycondensation reactions to form the final linear product, thereby indicating the homogeneous incorporation of Sn into the  $\text{TiO}_2$  lattice and rules out the possibility of independent  $\text{SnO}_2$  and  $\text{TiO}_2$  aggregates. It has been demonstrated that calcination at  $400^\circ\text{C}$  yielded mainly an amorphous mixed oxide; thus, heating needed to be carried out at  $500^\circ\text{C}$  to obtain the desired crystalline phases. Powder X-ray diffraction data indicate that pure  $\text{TiO}_2$  nanostructures are anatase when calcined at  $500^\circ\text{C}$ , but show a propensity to adopt the rutile phase at progressively higher Sn concentrations.

The results obtained in Ref. [135] suggest that both rutile and anatase doping is occurring, although the effect of the dopant cation is different for both phases. The study of single-phase doped samples suggests a random substitution of  $\text{Sn}^{4+}$  for  $\text{Ti}^{4+}$  in rutile, while for anatase some kind of ordering or surface accumulation of  $\text{Sn}^{4+}$  ions is possible.

The effect of doping with Sn on the phase transition of anatase to rutile has also been investigated on high area powders prepared by a sol-gel route involving alkoxide precursors [136]. It has been demonstrated that Sn doping facilitates conversion of anatase to rutile at lower temperatures than observed for undoped material. At the same time Sn-doping inhibits sintering as gauged by line widths in XRD and gas-adsorption surface area measurements. These observations are linked to the finding of pronounced segregation of Sn to the surface of rutile  $\text{TiO}_2$  observed in X-ray photoemission spectra.

It should be noted that the compositions of Sn-doped  $\text{TiO}_2$  materials can also be estimated using the molten-salt method employed by Naidu and Virkar [137]. In Ref. [138] the effect of Sn doping on the geometrical and electronic properties of  $\text{TiO}_2$  by means of first-principles electronic structure calculations was systemically investigated. These results provide explanations not only for the red-shift and blue-shift of the optical absorption edge in different experiments, but also for the different electronic properties between Sn-doped anatase and rutile  $\text{TiO}_2$ , with a certain Sn content resulting in the transformation of the two phases.

#### ***2.3.4. $\text{TiO}_2$ -rutile-based $\text{Ti}_{(1-x)}\text{M}_x\text{O}_2$ -C (M: W, Mo) composite supported Pt catalysts: previous results***

The concept of transition metal doped  $\text{TiO}_2$  – active carbon composite supports is based on the idea of bringing together the excellent stability and nanoparticle-stabilizing ability of  $\text{TiO}_2$  with the good co-catalytic properties of oxophilic metal and with the good conductivity and large surface area of active carbon in a unique material system.

A practical realization of such a material is a mixed oxide – active carbon composite support, in which W or Mo ions are introduced into substitutional sites of the  $\text{TiO}_2$  lattice. Under such circumstances the  $\text{TiO}_2$  lattice protects the doping metals from dissolution while they can still provide CO tolerance. The acceptable surface area and good conductivity are ensured by the active carbon backbone.

Recent studies of the research group have demonstrated the feasibility of this idea. Slightly different multistep sol-gel-based synthesis procedures were optimized for the Mo- and the W-doped

composites [139,140]. Previous studies of the research group also revealed that (i) complete incorporation of the oxophilic metal can be achieved only into the TiO<sub>2</sub>-rutile lattice and (ii) the formation of the rutile phase TiO<sub>2</sub> nucleus before the high-temperature treatment is prerequisite [141-143].

A correlation was found between the extent of dopant incorporation and the stability of the electrocatalysts: composites with lower amount of segregated oxides of doping element showed better stability. Thus, for example, Ti<sub>0.8</sub>Mo<sub>0.2</sub>O<sub>2</sub>-C composites with Ti/Mo= 80/20 atomic ratio was proved to be an optimal composition, as complete incorporation of the Mo dopant was observed, i.e. no free MoO<sub>x</sub> was detected [144].

The electrochemical stability tests revealed that the degradation rate of the composite supported electrocatalysts was much smaller than that of the Pt/C and PtRu/C catalysts [145]. Better performance of the Pt/Ti<sub>0.7</sub>M<sub>0.3</sub>O<sub>2</sub>-C (M= W, Mo) catalysts in a single cell test device using hydrogen containing 100 ppm CO compared to the reference Pt/C and PtRu/C catalysts was also demonstrated [146].

In recent study [147] good CO tolerance of the catalyst was demonstrated by investigation of the impact of catalyst loading, pressure and composition of reformat gas on the PEM fuel cell performance of Ti<sub>0.8</sub>Mo<sub>0.2</sub>O<sub>2</sub>-C composite supported Pt anode catalyst with 20 wt.% loading. It was found [147] that dilution of hydrogen with CO<sub>2</sub> and CH<sub>4</sub> in reformat gas had negligible negative impact on the fuel cell performance. Switching gas composition between hydrogen and reformat shows recovery of potential after CO poisoning.

### 3. Objectives of the study

According to a review of the literature and the previous experience of the research team, it has been revealed that oxophilic metal-doped  $\text{TiO}_2$ -rutile-based mixed oxide–carbon composite supported Pt catalysts are attractive catalytic systems with increased resistance to carbon monoxide and stability for use in PEM fuel cell.

The goal of my research has been to develop a composite support consisting of corrosion-resistant  $\text{Ti}_{(1-x)}\text{Sn}_x\text{O}_2$  mixed oxide coating over the activated carbon backbone. An important purpose was to maximize the number of active sites associated with the interfacial contacts between the Pt particles and the mixed oxide layer by optimizing the oxide and carbon content of the support along with the amount of the tin dopant.

To design the intended electrocatalysts, 20 wt.% platinum has been planned to load onto  $\text{Ti}_{(1-x)}\text{Sn}_x\text{O}_2\text{-C}$  ( $x= 0.1\text{-}0.3$ ) composite type catalyst supports with high and low mixed oxide content (75 and 25 wt.%) with respect to the carbon content. Specific goal of my research is to investigate the influence of this ratio on the CO tolerance and stability of the 20 wt.% Pt/ $\text{Ti}_{(1-x)}\text{Sn}_x\text{O}_2\text{-C}$  electrocatalysts.

The catalytic properties of the new electrocatalysts have to be compared to those of commercially available 20 wt.% Pt/C Quintech catalyst, which is the state-of-the-art catalyst for PEM fuel cell application. The new types of composites and related Pt catalysts have to be characterized by physicochemical methods such as XRD, TEM, SEM, EDX and XPS techniques.

To find correlation between the electrochemical behaviour (carbon monoxide tolerance, activity, long-term stability) and the structure of the novel Sn-containing composite supported Pt electrocatalysts is one of the important missions.

## 4. Experimental

### 4.1. Materials used

**Table 1.** Chemicals used for preparation of composite support materials

| Material                    | Chemical Formula                       | Supplier          | Purity              |
|-----------------------------|--|-------------------|---------------------|
| Milli-Q Water               | H <sub>2</sub> O                       | MTA TTK AKI       | Millipore, 18 MΩ cm |
| Nitric acid                 | HNO <sub>3</sub>                       | Molar Chemicals   | a.r.                |
| Titanium-isopropoxide       | Ti(O- <i>i-Pr</i> ) <sub>4</sub>       | Sigma-Aldich      | 97 %                |
| Activated carbon            | Black Pearls 2000                      | Cabot Corporation |                     |
| Tin (IV) chloride-5-hydrate | SnCl <sub>4</sub> x 5 H <sub>2</sub> O | Riedel-de Haen    | 98 %                |

**Table 2.** Chemicals used in platinum loading

| Material                        | Chemical Formula                                     | Supplier        | Purity    |
|---------------------------------|--|-----------------|-----------|
| Chloroplatinic acid hexahydrate | H <sub>2</sub> PtCl <sub>6</sub> x 6H <sub>2</sub> O | Sigma-Aldrich   | 37.5 % Pt |
| Ethanol                         | C <sub>2</sub> H <sub>5</sub> OH                     | Molar Chemicals | 99.95 %   |
| Sodium borohydride              | NaBH <sub>4</sub>                                    | Molar Chemicals | 99.99%    |
| Ethylene glycol                 | (CH <sub>2</sub> OH) <sub>2</sub>                    | Molar Chemicals | 99.8%     |
| Hydrochloric acid (37%)         | HCl  | Molar Chemicals | -         |

**Table 3.** Chemicals used in electrochemical testing

| Material                                 | Chemical Formula                           | Supplier                   | Purity                                       |
|--|--|----------------------------|--|
| Argon (gas)                              | Ar   | Linde Gas Hungary Co       | 5.0  |
| Hydrogen (gas)                           | H <sub>2</sub>                             | Linde Gas Hungary Co       | 5.0  |
| Carbon monoxide (gas)                    | CO   | Messer Hungarogas          | 4.7  |
| Oxygen (gas)                             | O <sub>2</sub>                             | Linde Gas Hungary Co       | 5.0  |
| Milli-Q Water                            | H <sub>2</sub> O                           | MTA TTK AKI                | Millipore, 18.2 MΩ cm                        |
| Sulphuric acid (96%)                     | H <sub>2</sub> SO <sub>4</sub>             | Merck                      | PA   |
| 2-propanol                               | <i>i</i> -C <sub>3</sub> H <sub>5</sub> OH | Molar Chemicals            | 99.9%  |
| Nafion solution (D520 Nafion Dispersion) | -  | Quintech (DuPont™ Nafion®) | Alcohol based 1000 EW <sup>1</sup> at 5 wt.% |

<sup>1</sup>EW: equivalent weight

### 4.2. Preparation of supports

#### 4.2.1. Synthesis of the 75 wt.% Ti<sub>(1-x)</sub>Sn<sub>x</sub>O<sub>2</sub> - 25 wt.% C (x: 0.1-0.3) composite materials

##### Route A

For the preparation of new type of tin-containing composites with different compositions the technique we have developed for Ti<sub>0.8</sub>Mo<sub>0.2</sub>O<sub>2</sub>-C materials was adapted [144]. The synthesis of novel Ti<sub>(1-x)</sub>Sn<sub>x</sub>O<sub>2</sub>-C (x: 0.1-0.3) composite supports was performed using tin (IV) chloride pentahydrate, as Sn precursor compound, and carbon black (BP: Black Pearls 2000, Cabot Corporation). First, the

composite support materials with mass ratio of the  $Ti_{(1-x)}Sn_xO_2/C = 75:25$  were prepared by multistep sol-gel synthesis followed by high-temperature treatment (HTT) as shown in Figure 6 (route A).

As shown in Table 4 the samples were identified by a unique identifier, which contains the nominal composition of the composite materials denoted by the nominal weight percentage of the mixed oxide with respect to the carbon content, along with the nominal content of Sn in mixed oxide: e.g., 75Sn01 means the composite of 75 wt.%  $Ti_{0.9}Sn_{0.1}O_2 - 25$  wt.% C.

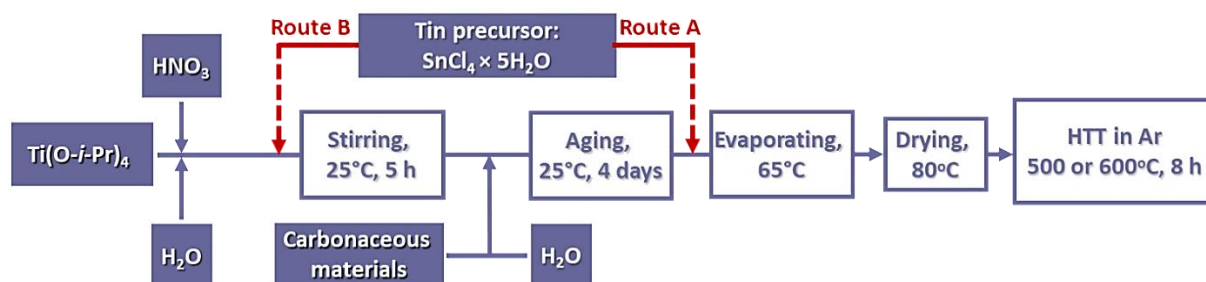


**Figure 6.** Preparation steps of  $Ti_{(1-x)}Sn_xO_2-C$  composites ( $Ti_{(1-x)}Sn_xO_2/C = 75/25$  wt.%/wt.%; HTT: high-temperature treatment).

**Table 4.** Nominal composition and preparation details of the  $Ti_{(1-x)}Sn_xO_2-C$  (C: Black Pearls 2000) samples with the different Ti/Sn and  $Ti_{(1-x)}Sn_xO_2/C$  ratios

| Sample                 | Samples nominal composition                               | TiO <sub>2</sub> sol  |                       |                             | Suspension of carbon |                       |                       | Sn prec. <sup>b)</sup> (g) |
|------------------------|---|-----------------------|-----------------------|-----------------------------|----------------------|-----------------------|-----------------------|----------------------------|
|                        |   | H <sub>2</sub> O (ml) | HNO <sub>3</sub> (ml) | Ti prec. <sup>a)</sup> (ml) | C (g)                | H <sub>2</sub> O (ml) | HNO <sub>3</sub> (ml) |                            |
| 75Sn01                 | 75Ti <sub>0.9</sub> Sn <sub>0.1</sub> O <sub>2</sub> -25C | 23.47                 | 2.628                 | 2.298                       | 0.25                 | 10.0                  | -                     | 0.3024                     |
| 75Sn02                 | 75Ti <sub>0.8</sub> Sn <sub>0.2</sub> O <sub>2</sub> -25C | 19.29                 | 2.160                 | 1.889                       | 0.25                 | 10.0                  | -                     | 0.5593                     |
| 75Sn03                 | 75Ti <sub>0.7</sub> Sn <sub>0.3</sub> O <sub>2</sub> -25C | 15.18                 | 1.760                 | 1.539                       | 0.25                 | 10.0                  | 0.090                 | 0.7501                     |
| 25Sn02                 | 25Ti <sub>0.8</sub> Sn <sub>0.2</sub> O <sub>2</sub> -75C | 6.43                  | 0.72                  | 0.630                       | 0.75                 | 24.1                  | 1.441                 | 0.1864                     |
| 25Sn02-7 <sup>c)</sup> | 25Ti <sub>0.8</sub> Sn <sub>0.2</sub> O <sub>2</sub> -75C | 6.43                  | 0.72                  | 0.630                       | 0.75                 | 24.1                  | 1.441                 | 0.1864                     |

<sup>a)</sup> Ti precursor compound: titanium-isopropoxide ( $Ti(O-i-Pr)_4$ , Aldrich, 97%);

<sup>b)</sup> Sn precursor compound: tin (IV) chloride pentahydrate ( $SnCl_4 \times 5H_2O$ , Riedel-de Haen, 98%);

<sup>c)</sup> the duration of the aging step was 7 days.

The preparation of the mixed oxide – carbon composites consisted of three main steps (see Figure 6, route A): i) low temperature deposition of TiO<sub>2</sub>-rutile nuclei on the carbon black completed by an aging step, ii) introduction of the Sn precursor and iii) incorporation of the Sn into the TiO<sub>2</sub>-rutile crystallites using a high-temperature treatment step (HTT: Ar, 600 °C, 8 hours). Table 4 summarizes the quantities of the titanium and tin precursors as well as amount of the carbonaceous material used in the synthesis of support materials.

### Route B

In comparison to route A, the main difference in the preparation of composite materials via route B is that the precursor of Sn was introduced immediately after the formation of the transparent Ti-sol, before the addition of the carbon and the aging step (Figure 6, route B).

Moreover, in synthesis route **B**, the final temperature of the HTT in Ar was 500 °C, the duration was 8 hours.

#### 4.2.2. Synthesis of the 25 wt.% $Ti_{0.8}Sn_{0.2}O_2$ - 75 wt.% C composite materials

The difference between the preparations of two 25Sn02 and 25Sn02-7 samples with high carbon content was the duration of the aging step, which was 4 and 7 days, respectively (see Figure 7). It should be noted that in preparation composites with a carbon content of 75 wt.%, it is important to load additional cc.  $HNO_3$  before starting the aging procedure to maintain the appropriate acidity of the synthesis mixture (for more details see Table 4).

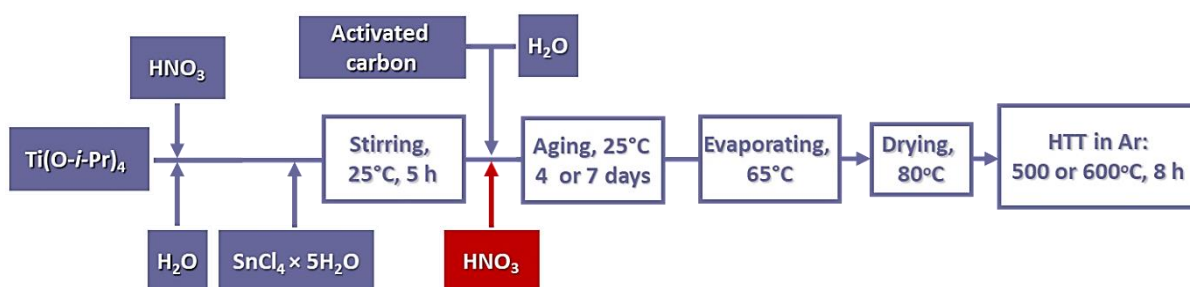


**Figure 7.** Preparation steps of 25 wt.%  $Ti_{0.8}Sn_{0.2}O_2$ - 75 wt.% C composites via route **B** (HTT: high-temperature treatment)

#### 4.3. Preparation of the 20 wt.% Pt/ $Ti_xSn_{(1-x)}O_2$ -C electrocatalysts

By employing a modified  $NaBH_4$ -assisted ethylene-glycol (EG) reduction-precipitation technique, as shown schematically in the Figure 8 [144],  $Ti_xSn_{(1-x)}O_2$ -C composite materials were loaded with 20 wt.% Pt.

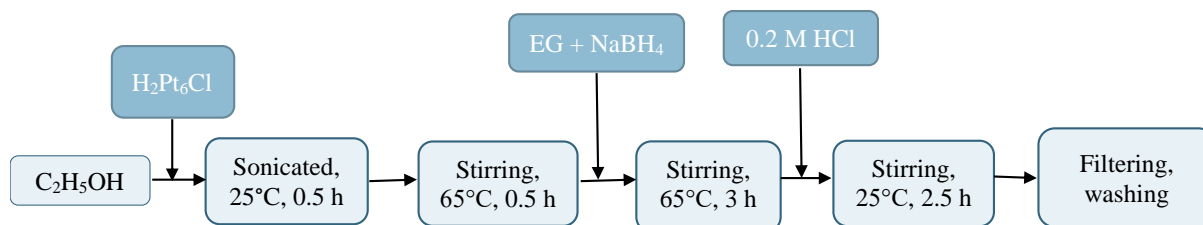


**Figure 8.** Synthesis of  $Ti_xSn_{(1-x)}O_2$ -C electrocatalysts

In each case, 0.643 mmol  $H_2PtCl_6 \times 6H_2O$  was dissolved in 50 ml of ethanol, and 200 mg of the samples were suspended in the solution to get the desired results (see Table 5). Dropwise additions of a solution made by combining 7.8 mmol  $NaBH_4$  with 3.7 ml EG were made to the suspension at 65 °C while it was being continuously stirred. Using a stirrer at 65 °C for 3 hours, 15 ml of 0.2 M HCl was added to the suspension, which was then agitated for a further 2.5 hours at room temperature to deposit the platinum particles onto the support material. It was necessary to wash the materials three times with 50 mL water and filter them by centrifuge to remove the chloride ions before drying them at 80 °C in an oven for a whole night.

**Table 5.** Addition of Pt to catalyst support via NaBH<sub>4</sub> reduction method

| Amounts             | Substance   | Characteristics, comments                                  |                     |
|---------------------|---|--|---------------------|
| 134 mg              | H <sub>2</sub> PtCl <sub>6</sub> ×6H <sub>2</sub> O | M <sub>H<sub>2</sub>PtCl<sub>6</sub>×6H<sub>2</sub>O</sub> | 517.891 g/mol       |
| 50 ml               | abs. EtOH   | M <sub>Pt</sub>  | 195,078 g/mol       |
| 200 mg              | catalyst support                                    | V <sub>added NaBH<sub>4</sub> solution</sub>               | 3.7 cm <sup>3</sup> |
| 596 mg              | NaBH <sub>4</sub>                                   | t <sub>added NaBH<sub>4</sub> solution</sub>               | 30 min              |
| 7.4 cm <sup>3</sup> | EG  | ID <sub>10ml syringe</sub>                                 | 16.10 mm            |
| 15 cm <sup>3</sup>  | 0.2 M HCl   | ID <sub>5ml syringe</sub>                                  | 12.35 mm            |

To summarize the synthesis work, Table 6 contains abbreviation and nominal composition details of the Ti<sub>(1-x)</sub>Sn<sub>x</sub>O<sub>2</sub>-C composite supported 20 wt.% Pt electrocatalysts studied. The abbreviation of catalysts additionally indicates the catalyst synthesis route (**A** or **B**), as well as the final temperature of the high-temperature treatment in Ar (500 or 600 °C): e.g., Pt/75Sn01/B/500 means Pt catalyst supported on 75 wt.% Ti<sub>0.9</sub>Sn<sub>0.1</sub>O<sub>2</sub> - 25 wt.% C composite, which was prepared by synthesis route **B** and then annealed in Ar at 500 °C for 8 hours.

**Table 6.** Abbreviation and nominal composition details of the Ti<sub>(1-x)</sub>Sn<sub>x</sub>O<sub>2</sub>-C composite supported 20 wt.% Pt electrocatalysts.

| Sample ID                       | Nominal composition  | Ti/Sn | HTT,<br>°C |
|---------------------------------|--|-------|------------|
| Pt/75Sn01/A/600                 | Pt/75 wt.% Ti <sub>0.9</sub> Sn <sub>0.1</sub> O <sub>2</sub> -25 wt.% C | 90/10 | 600        |
| Pt/75Sn02/A/600                 | Pt/75 wt.% Ti <sub>0.8</sub> Sn <sub>0.2</sub> O <sub>2</sub> -25 wt.% C | 80/20 | 600        |
| Pt/75Sn03/A/600                 | Pt/75 wt.% Ti <sub>0.7</sub> Sn <sub>0.3</sub> O <sub>2</sub> -25 wt.% C | 70/30 | 600        |
| Pt/75Sn01/B/500                 | Pt/75 wt.% Ti <sub>0.9</sub> Sn <sub>0.1</sub> O <sub>2</sub> -25 wt.% C | 90/10 | 500        |
| Pt/75Sn02/B/500                 | Pt/75 wt.% Ti <sub>0.8</sub> Sn <sub>0.2</sub> O <sub>2</sub> -25 wt.% C | 80/20 | 500        |
| Pt/75Sn03/B/500                 | Pt/75 wt.% Ti <sub>0.7</sub> Sn <sub>0.3</sub> O <sub>2</sub> -25 wt.% C | 70/30 | 500        |
| Pt/25Sn02/B/500                 | Pt/25 wt.% Ti <sub>0.8</sub> Sn <sub>0.2</sub> O <sub>2</sub> -75 wt.% C | 80/20 | 500        |
| Pt/25Sn02/B-7/500 <sup>a)</sup> | Pt/25 wt.% Ti <sub>0.8</sub> Sn <sub>0.2</sub> O <sub>2</sub> -75 wt.% C | 80/20 | 500        |

<sup>a)</sup> Aging step: 7 days.

Preliminary results of the research group demonstrate [143] that when preparing composite materials with the Ti<sub>0.8</sub>Mo<sub>0.2</sub>O<sub>2</sub>/C= 25/75 ratio, aging the synthesis mixture at room temperature for 4 days is not always sufficient to prepare a pure TiO<sub>2</sub>-rutile phase. The difference between the two high carbon composites (25Sn02) was the length of the aging step: 4 or 7 days. Thus, the indication in the abbreviation of the catalyst Pt/25Sn02/B-7/500 means that the aging step is not the commonly used 4 days, but it is 7 days.

#### 4.4. Physicochemical characterization

##### 4.4.1. X-Ray Power Diffraction (XRD)

X-ray powder diffraction (XRD) patterns were obtained in a Philips model PW 3710 based PW 1050 Bragg-Brentano parafocusing goniometer (Figure 9) using CuK $\alpha$  radiation ( $\lambda$ = 0.15418 nm),

graphite monochromator and proportional counter. Silicon powder (NIST SRM 640) was used as an internal standard and the scans were evaluated with profile fitting methods. The cell parameters of the crystalline phases were determined from the fitted values.



**Figure 9.** XRD Equipment

#### **4.4.2. X-ray photoelectron spectroscopy (XPS)**

XPS measurements were performed with the use of a spectrometer made by OMICRON Nanotechnology GmbH, Germany (Figure 10). The photoelectrons were excited by MgK $\alpha$  radiation (with an energy of 1253.6 eV). When using the Constant Analyser Energy mode of the EA125 energy analyser, spectra were recorded with a pass energy of 30 eV, which resulted in a spectral resolution of around 1 eV.

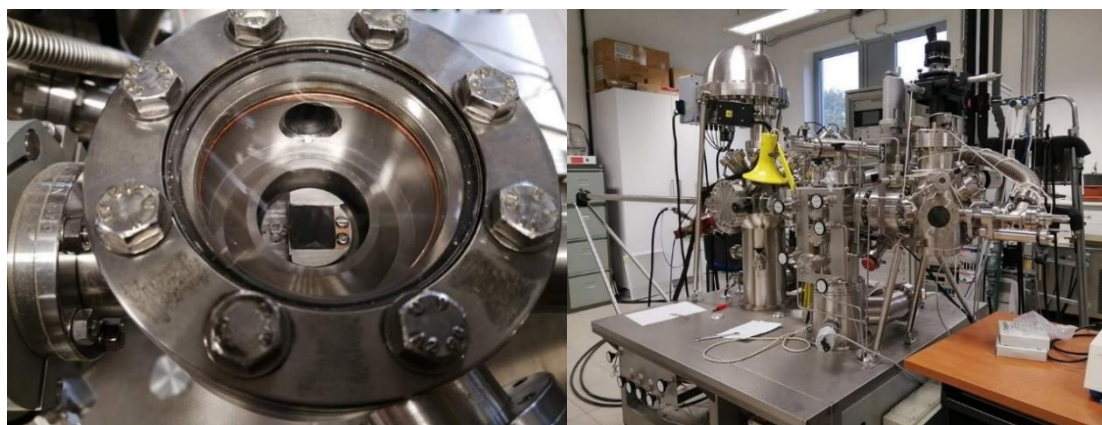


**Figure 10.** XPS Equipment

The powdered composite support and electrocatalyst samples were suspended in isopropanol, and droplets of this suspension were dried in the open air on standard stainless steel Omicron sample plate. For the samples studied here, this approach provided excellent mechanical stability and good electrical contact.

Spectra from the regions of interest (typically Ti 2p, Sn 3d, Pt 4f, C 1s, O 1s) were gathered after a survey spectrum had been measured. During the data collecting process, a circular region with a diameter of approximately 6 mm was sampled.

In this study, spectra were processed using the CasaXPS software [148], and quantitative assessment of the data was conducted using the XPSMultiQuant package [149,150], with the assumption that all components had a homogenous depth distribution.

In order to identify chemical states, we used the NIST database [151], the database [152], or other relevant literature as stated. The binding energy scale was referenced to the lowest binding energy contribution of the C 1s envelope, which arose from graphite-like ( $sp^2$ -hybridized) carbon in the active carbon backbone at 284.4 eV binding energy [146-150].

#### **4.4.3. Nitrogen physisorption measurements**

Nitrogen physisorption measurements were carried out at  $-196\text{ }^\circ\text{C}$  using Thermo Scientific Surfer automatic volumetric adsorption analyzer (Thermo Fischer Scientific, Berlin, Germany). The specific surface area was calculated by the BET method in the range of relative pressures from 0.05 to 0.30.

#### **4.4.4. Transmission Electron Microscopy (TEM)**

Transmission Electron Microscopy (TEM) studies of the samples were made by use of a JEOL 3010 high resolution transmission electron microscope (Tokyo, Japan) operating at 300 kV. The structure has been identified by Selected Area Electron Diffraction (SAED) and the compositional homogeneity has been checked by Scanning Transmission Electron Microscopy (STEM) coupled with Energy Dispersive X-Ray Spectroscopy (EDS). The samples for TEM analysis were prepared by dripping a few drops from the material suspension of the powder in ethanol on a microscopy grid with a carbon membrane. These measurements were made in cooperation with Romanian colleagues at National Institute of Materials Physics (405A Atomistilor Street, 077125, Magurele, Romania).

#### **4.4.5. Scanning Electron Microscopy (SEM)**

Recordings of scanning electron micrographs of the samples were made using a scanning electron microscope Vega II LMU model from Tescan (Brno, Czech Republic), which was equipped with an energy dispersive X-ray spectrometer (EDX) Bruker Quantax 200 (Bruker Physik-AG, Karlsruhe, Germany), at the following operational parameters: accelerating voltage 30 kV, measuring time 1200 s, working distance around 17 mm, counting rate. These measurements were made in cooperation with Romanian colleagues at National Institute of Materials Physics (405A Atomistilor Street, 077125, Magurele, Romania).

#### **4.4.6. Raman spectroscopic measurements**

Raman spectra were obtained on a LabRAM HR Evolution spectrometer from Horiba Jobin Ivon, with a laser radiation at wavelength of 633 nm. All spectra were recorded at room temperature in the extended scan mode in the 50 and 2000  $\text{cm}^{-1}$  range. The Raman spectroscopic measurements were made in cooperation with Romanian colleagues at National Institute of Materials Physics (405A Atomistilor Street, 077125, Magurele, Romania).

#### **4.4.7. Inductively coupled plasma - optical emission spectrometry (ICP-OES)**

After being dissolved with the assistance of a microwave in 1:8 mixes of concentrated nitric acid and hydrofluoric acid, the electrocatalysts were put through a process called inductively coupled plasma - optical emission spectrometry (ICP-OES) so that the platinum concentration could be determined. In order to carry out the measurements, a simultaneous SPECTRO GENESIS equipment (manufactured by SPECTRO Analytical Instruments GmbH in Kleve, Germany) with axial plasma observation was utilized.

#### 4.5. Electrochemical Characterization

In a three-electrode electrochemical device, the produced materials were subjected to cyclic voltammetry and  $\text{CO}_{\text{ads}}$ -stripping voltammetry tests. The measurements were carried out with the help of a BioLogic SP 150 potentiostat and the EC Lab V10.02 software.

Figure 11 depicts the three-electrode electrochemical cell that I used for my tests, and shows how it was constructed.

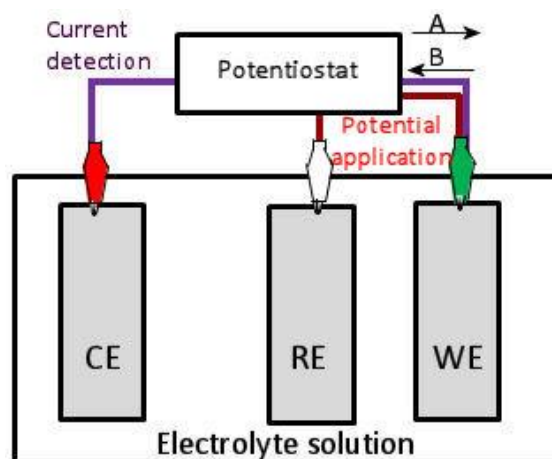


**Figure 11.** Three electrode electrochemical cell and the direction of current diagram [153]

The working electrode (WE) is a glassy carbon electrode with a diameter of 3 mm and an area of  $0.0707 \text{ cm}^2$ . Surface impurities were removed from the electrode by polishing in isopropanol. To analyse the sample, it was powdered, and an ink was made by dispersing 2 mg of the catalyst samples in 2 ml of 1.592 ml of MilliQ water, 0.4 ml of isopropanol, and 8 ml of 5% Nafion<sup>®</sup> solution. The suspension was subjected to 30 minutes of sonication. A drop ( $3.6 \mu\text{L}$ ) of this suspension was pipetted onto a dry mirror-polished GC and allowed to dry at room temperature for 20 minutes before use (see Figure 12). The electrode was loaded with Pt at a rate of  $10 \mu\text{g}/\text{cm}^2$  in all cases.

The hydrogen electrode served as the reference electrode in the cell, while the counter electrode was a spiral platinum fiber, and the electrolyte was a 0.5 M  $\text{H}_2\text{SO}_4$  solution.

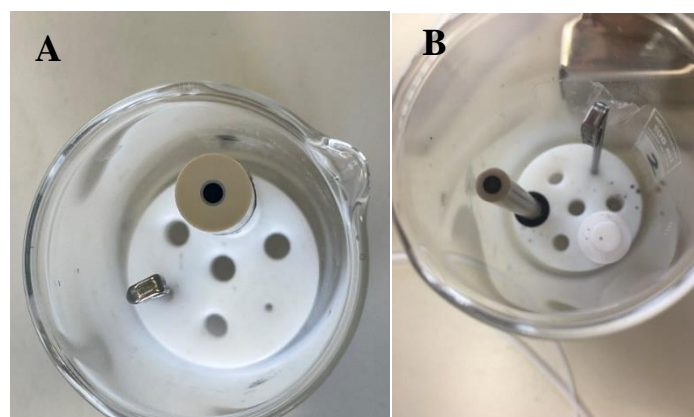


**Figure 12.** Working electrode with dry ink: (A) rotating disk electrode and (B) static electrode.

##### 4.5.1. Cyclic Voltammetry (CV)

CV stands for cyclic voltammetry, which is a potentiodynamic electrochemical measurement. The working electrode potential is increased linearly as a function time in a cyclic voltammetry

experiment; after reaching the maximum potential, the polarization of the working electrode is reversed and the potential returns to initial value. The working electrode is polarized, or its potential is altered relative to the reference electrode, using a potentiostat. The current flowing between the counter and the working electrodes is monitored continuously. During the measurements, the potential of the reference electrode is assumed to be constant.

The electrolyte was purged with argon 30 minutes before the commencement of the cyclic voltammometry measurement to remove any air (oxygen) that might affect the measurement. Voltammograms were obtained between 50 and 1000 mV at polarization rates of 100 mV/s and 10 mV/s during the measurements.

A cyclic voltammogram of a platinum electrode is shown in Figure 13, which may be separated into three distinct sections:

- hydrogen adsorption/desorption;
- electrochemical double layer area;
- platinum oxide formation/reduction.

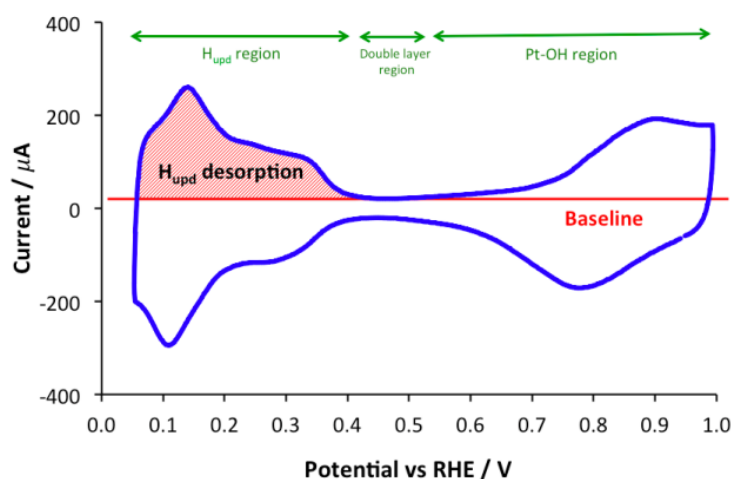


Figure 13. Cyclic voltammogram of a platinum electrode [154]

The electrochemically active surface area of a high surface area catalyst is an important property that is crucial when determining the mass activity as well as the specific activity. It can be calculated from the charge it takes to adsorb/desorb a layer of hydrogen in the so-called H<sub>upd</sub> region in a cyclic voltammograms [155]:



Using the equation (6) [156], the electrochemically active Pt surface area (ECSA<sub>H<sub>upd</sub></sub>) may be derived from the monolayer hydrogen oxidation charge:

$$\text{ECSA}_{\text{H}_{\text{upd}}} (\text{cm}^2) = Q_{\text{oxH}_{\text{upd}}} (\mu\text{C}) / 210 (\mu\text{C}/\text{cm}^2) \quad (\text{Equation 7})$$

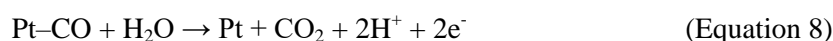
where ECSA<sub>H<sub>upd</sub></sub> is the electrochemical surface area determined from the amount of underpotentially deposited hydrogen on the platinum surface; Q<sub>oxH<sub>upd</sub></sub> is the oxidation charge of underpotentially deposited hydrogen obtained from the CV experiment; and 210 (C/cm<sup>2</sup>) is the amount of charge required to oxidize monolayer.

#### 4.5.2. Characterization by $CO_{ads}$ -stripping voltammetry

The electrolyte was purged with Ar for at least 20 minutes before each electrochemical test, and 10 CVs were recorded with a 100 mV/s sweep rate between 50 and 1000 mV to condition the catalysts.

The working electrode potential was decreased from open circuit potential to 50 mV at a polarization rate of 10 mV/s during the  $CO_{ads}$ -stripping voltammetry study. The electrolyte was then saturated with carbon monoxide for 20 minutes, causing carbon monoxide to adsorb on the Pt surface. Following that, the solution was purged with argon for 20 minutes to eliminate any carbon monoxide dissolved in the electrolyte or physisorbed carbon monoxide, leaving only the chemisorbed CO on the platinum surface. The working electrode potential was held constant at 50 mV during this period. After that, two cyclic voltammograms were recorded: the potential was raised at a rate of 10 mV/s from 50 mV to 1000 mV, then restored to 50 mV, and the operation was repeated.

Because it has significant benefits over the  $H_{upd}$  approach, CO-stripping voltammetry has been frequently employed for surface area measurements of Pt-based fuel cell catalysts. The proper selection of integration limits and the elimination of background currents that are unrelated to CO oxidation provide a difficulty for CO-stripping surface area measurement (see Fig. 14, Ref. [157]). The production of Pt–O and double-layer charging are the principal sources of these currents (H). After background adjustment, the residual charge (Equation 7) comes primarily from CO oxidation:



A charge of  $420 \text{ C/cm}_{Pt}^2$  is often employed in CO-stripping voltammetry of Pt/C catalysts. Equation 6 may be used to compute the electrochemically active surface of the catalyst ( $ECSA_{CO}$ ) using the area of the CO oxidation peak ( $Q_{oxCO}$ : the CO oxidation charge).

$$ECSA_{CO} (\text{cm}^2) = Q_{oxCO} (\mu\text{C}) / 420 (\mu\text{C/cm}^2) \quad (\text{Equation 9})$$

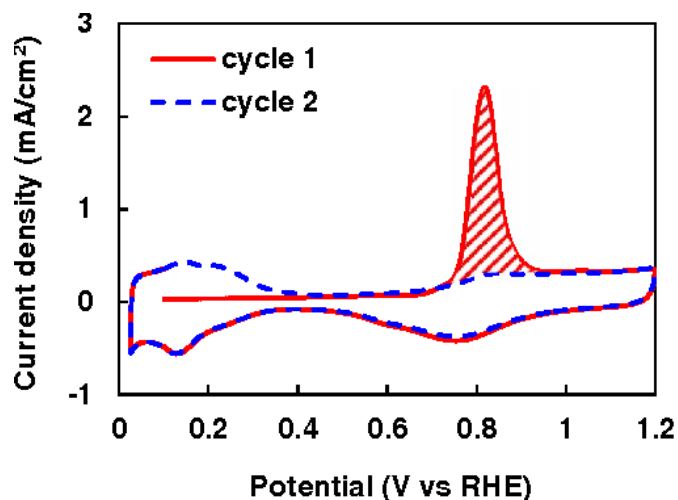


**Figure 14.** CO stripping voltammogram for Pt/HSC catalyst in  $N_2$ -purged 0.1 M  $HClO_4$  at 20 mV/s: first curve obtained after saturation of Pt surfaces with CO (solid red line), second sweep (blue dotted line) [157]

#### 4.5.3. Stability test

Polarizing the working electrode in the 50 to 1000 mV potential range at a scan rate of 100 mV/s for 500 and 10,000 cycles was used to test electrochemical stability. Using traditional baseline correction, the  $Q_{H-UPD}$  charges associated with hydrogen adsorption/desorption were estimated. Results concerning on the change of the electrochemically active Pt surface area upon the N-cycle stability test

are presented as  $ECSA_N$  (N: 500, 2,500, 5,000 and 10,000) normalized to  $ECSA_1$  measured in the first cycle on the same sample. Another measure of the change of the electrochemically active Pt surface area is the  $\Delta ECSA$  value defined in Equation 10:

$$\Delta ECSA_N = \{1 - (ECSA_N / ECSA_1)\} \times 100\% \quad (\text{Equation 10})$$

To avoid re-deposition of the dissolved metals, the electrolyte was replaced after each stability test. After the stability test, the second Ar-purged  $CO_{ads}$ -stripping voltammetric measurement was performed.

#### 4.5.4. Characterization by rotating disk electrode (RDE) technique

ORR measurements were carried out using a rotating disk electrode (RDE). This is required in order to accurately adjust the oxygen diffusion conditions from the interior of the solution to the electrode surface during the measurement. A laminar flow forms in the vicinity of the electrode as a result of the rotation, which forms a film between the electrode surface and the electrolyte bulk phase with an adjustable layer thickness between the electrode surface and the electrolyte bulk phase, through which the material transport can only take place by diffusion, i.e. there is no turbulent mixing directly on the electrode surface, only inside the solution. Figure 15 depicts the creation of the surface laminar layer.

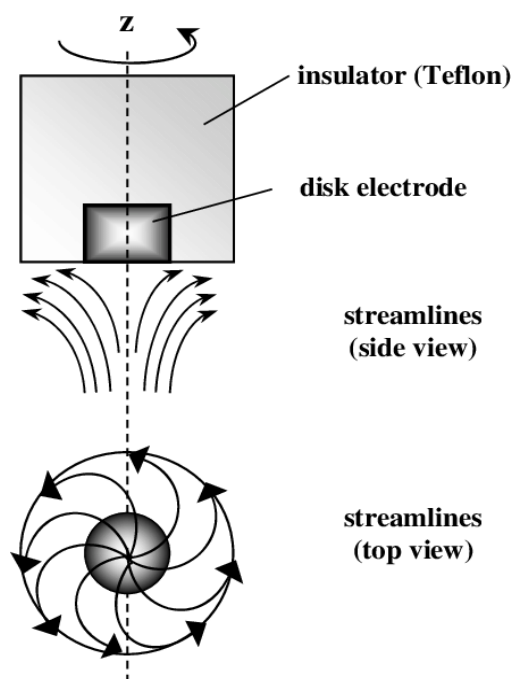


**Figure 15.** Streamlines for flow of fluid velocity near a rotating disk electrode [158]

A diffusion boundary layer will form at the electrode-electrolyte interface as a result of the electrode's rotation, where the oxygen only moves by diffusion [159]. It is reasonable to suppose that the distribution of the various species within the solution is homogeneous. The rotating movement of the electrode also contributes to perfect mixing. In this scenario, Fick's law dictates that the oxygen concentration in the surface film between the bulk phase and the surface fluctuates. As the speed of the rotation increases, the thickness of the diffusion boundary layer decreases, requiring the oxygen to travel a shorter distance (the diffusion route length decreases), resulting in diffusion acceleration [160].

The electrolyte was saturated with oxygen for 30 minutes before to the measurement, after which the oxygen reduction curves were recorded at various rotating speeds (225, 400, 625, 900, 1225 rpm). At a polarization rate of 10 mV/s, oxygen reduction curves were observed between 1000 and 200 mV.

Figure 16 shows the ORR curve for a commercially available 20 wt.% Pt/C catalyst (Quintech). There are three sections to the curve: a kinetically controlled region, a mixed region, and a diffusion-controlled region.

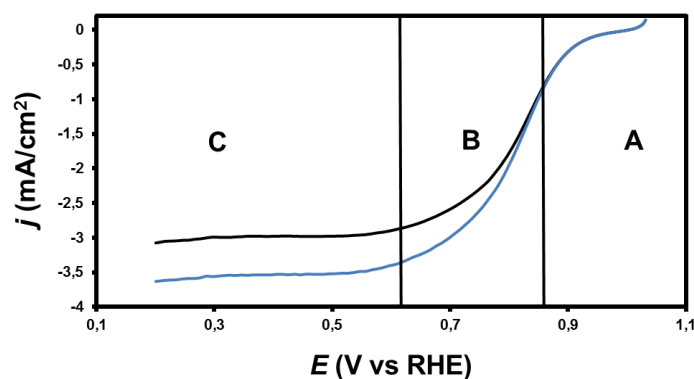


**Figure 16.** Curve of a commercially available 20 wt.% Pt/C (Quintech) catalyst in an ORR in 0.5 M  $\text{H}_2\text{SO}_4$ , after oxygen saturation at 80 ml/min for 30 minutes at various speeds (black: 625 rpm, blue: 900 rpm), between 1000 and 200 mV at a polarization rate of 20 mV/s. The current density is a number that has been scaled to fit the geometric surface. **A:** kinetically controlled region, **B:** mixed region, **C:** diffusion determined region.

*Kinetically controlled region (A):* At this stage, the overvoltage is small compared to the equilibrium potential of thermodynamics (1.23 V), the mass transport limitations do not play a decisive role. Diffusion through the diffusion film is significantly faster than the oxygen reduction reaction at the surface. As a result, there is no difference in the obtained reduction currents due to the rotation speed, as can be seen in the figure above. Oxygen depletion is determined by kinetics and not by diffusion [161].

*Mixed Region (B):* This part of the curve is affected by both mass transport and reaction kinetics. As a result of the two processes, the relative oxygen coverage on the surface is not complete, i.e., not all adsorbed oxygen is present at the active site. At this stage, oxygen supply through the diffusion layer is already partially inhibited [162].

*Region defined by mass transport (C):* As the overvoltage increases, a significant but saturable increase in current density values is observed due to the mass transport processes that come to the fore [162]. The surface relative oxygen coverage is virtually zero. All oxygen species reaching the surface are also reduced at the moment of adsorption. The reaction rate is higher than the diffusion rate. In this case, the oxygen supply from the solution and the correspondingly higher current density can only be achieved by increasing the oxygen concentration of the solution or by reducing the diffusion boundary layer (higher speed). It can be observed in Figure 16 that the so-called ultimate current density is significantly higher at 900 rpm than at 625 rpm.

Catalytic activity in the hydrogen oxidation reaction (HOR) was also investigated by RDE method in hydrogen saturated 0.5 M  $\text{H}_2\text{SO}_4$  solution at 400, 625, 900, 1225 and 1600 rpm. Polarization curves were recorded by anodic scan sweeping the potential between 0 and 300 mV with 10 mV/s sweep rate. The diameter of RDE electrode and Pt loading used in these experiments was the same as during CV and ORR measurements.

## 5. Results and Discussion

### 5.1. Route A - physicochemical characterization of the $Ti_{(1-x)}Sn_xO_2-C$ composite support materials and related Pt electrocatalysts

For the preparation of new type of tin-containing composites with different compositions the technique we have developed for  $Ti_{0.8}Mo_{0.2}O_2-C$  materials was adapted [143]. The synthesis of novel  $Ti_{(1-x)}Sn_xO_2-C$  ( $x$ : 0.1-0.3) composite supports was performed using tin (IV) chloride pentahydrate, as Sn precursor compound, and carbon black (BP: Black Pearls 2000, CABOT).

First, the composite support materials with mass ratio of the  $Ti_{(1-x)}Sn_xO_2/C=75/25$  were prepared by multistep sol-gel synthesis followed by high-temperature treatment (HTT) as shown in Figure 6 (route A). XRD, nitrogen adsorption measurements, TEM, SEM/EDX, XPS and Raman spectroscopy were used to characterize the bulk and surface microstructure.

#### 5.1.1. Powder X-ray diffraction (XRD) investigations

The success of the synthesis of the Sn-doped composites with different Ti/Sn ratios was confirmed by XRD measurements, which provide information on the phase composition of the samples. After 600 °C HTT the changes in the lattice parameters measured by XRD confirmed the incorporation of tin into the  $TiO_2$ -rutile unit cell (see Table 7). The degree of Sn incorporation correlated with the amount of tin precursor (for  $Ti_{(1-x)}Sn_xO_2-C$  with  $x=0.1, 0.2$  and  $0.3$  it was  $Sn_{subst}=7, 14$  and  $23\%$ ).

**Table 7.** Structural properties of the  $Ti_{(1-x)}Sn_xO_2-C$  composite materials determined by XRD analysis

| Sample ID           | HTT<br>(Phase, %) |              | Lattice parameters, Å <sup>a)</sup> | $Sn_{subst}$ ,<br>% |
|---------------------|-------------------|--------------|-------------------------------------|---------------------|
|                     | R/nm              | $Sn^0/SnO_2$ |                                     |                     |
| <b>75Sn01/A/600</b> | 99/29             | 1/0          | $a=4.610, c=2.970$                  | 7-8                 |
| <b>75Sn02/A/600</b> | 99/22             | 1/0          | $a=4.620, c=2.985$                  | 14                  |
| <b>75Sn03/A/600</b> | 95/20             | 2/3          | $a=4.625, c=2.988$                  | 23                  |

<sup>a)</sup> Lattice parameters of the rutile phase obtained after HTT (pure rutile  $TiO_2$ :  $a=4.593$  Å,  $c=2.959$  Å).

Nevertheless, as shown in Figure 17, the presence a very small amount of metallic Sn (1-2%) was revealed in all samples. In the samples with less nominal Sn content the reflections characteristic to metallic Sn phase were almost negligible. Metallic tin can be formed as a result of carbothermal reduction of tin oxide [163]. It should be noted that small reflections characteristic to Sn oxide were found only in the composite with the highest Sn nominal content.

The composite-supported 20 wt.% Pt catalysts were prepared by a modified  $NaBH_4$ -assisted ethylene glycol reduction-precipitation method [144]. As shown in Figure 17, after the deposition of Pt, the reflections of the  $Sn^0$  phase completely disappear; in all Pt catalysts, platinum is present in nanodispersed form.

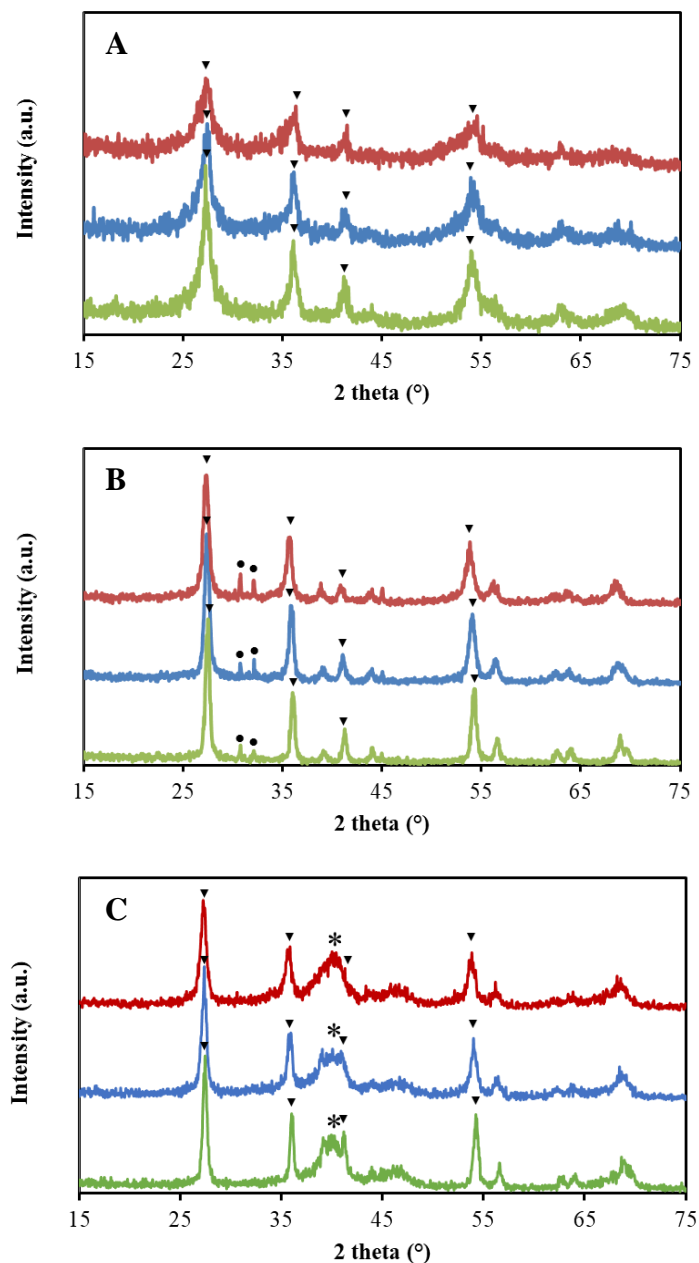


**Figure 17.** XRD patterns of 75Sn01/A/600 (green), 75Sn02/A/600 (blue) and 75Sn03/A/600 (red-brown) composite materials before (A) and after (B) HTT as well as after Pt loading (C). ▼- Rutile, ●- Sn<sup>0</sup>, \*- Pt.

### 5.1.2. Nitrogen physisorption measurements

One of the main requirements for the promising electrocatalyst supports is to have a specific surface area not less than 100 m<sup>2</sup>/g [20]. The results of nitrogen physisorption measurements were presented in Table 8. It should be noted that the specific surface area of these Sn-containing samples was higher compared to the similar Mo-containing composites (for 75 wt.% Ti<sub>0.8</sub>Mo<sub>0.2</sub>O<sub>2</sub>-25 wt.% C composite specific surface area ( $S_{\text{BET}}$ ) was 248 m<sup>2</sup>/g [143]).

**Table 8.** Results of nitrogen adsorption measurements

| Sample ID    | Ti/Sn | Surface area<br>(m <sup>2</sup> /g)      | Total pore volume<br>(cm <sup>3</sup> /g) |
|--------------|-------|--|---|
| 75Sn01/A/600 | 90/10 | 373.74                                   | 0.95                                      |
| 75Sn02/A/600 | 80/20 | 438.19                                   | 1.24                                      |
| 75Sn03/A/600 | 70/30 | 390.28                                   | 0.66                                      |
| BP (parent)  | -     | 1635 <sup>a)</sup><br>1485 <sup>b)</sup> | n.d.                                      |

n.d.: no data, **BP**: Black Pearls 2000 (Cabot);

<sup>a)</sup> from ref. [164];

<sup>b)</sup> from ref. [165].

### 5.1.3. Transmission electron microscopy (TEM) analysis

For microstructural investigations a Transmission Electron Microscope has been used. The compositional homogeneity has been checked by Scanning Transmission Electron Microscopy (STEM) coupled with Energy Dispersive X-Ray Spectroscopy (EDS): elemental mapping reveals the distribution of elements within the sample. The EDS unit has the capability of mapping elements present on a sample and superimposing a colored “map” of the location and concentration of various elements on top of a captured electron image.

Conventional bright field TEM images of the Sn-containing composite materials containing 75 wt.% Ti<sub>(1-x)</sub>Sn<sub>x</sub>O<sub>2</sub> and 25 wt.% C with various Ti/Sn ratios are compared in Figure 18. As the micrographs reveal, the morphology of the samples was relatively similar: in all cases the mixed oxide probably appeared in several morphologies. Nanorod-type larger crystallites (with length around 50-80 nm and width around 20 nm) often grouped into flower-like agglomerates, while small quasi-spherical oxide particles with sizes around 5 nm were more or less homogeneously mixed with carbon. The onion-like structure of the carbon material can also be well recognized. The co-existence of large oxide crystallites and small oxide particles, resulting in a certain structural inhomogeneity of the composite, was also documented for the Ti<sub>(1-x)</sub>Mo<sub>x</sub>O<sub>2</sub>-containing systems, especially for those containing higher amount of mixed oxide [143]. Interestingly, this inhomogeneity seemed to be less evident for the composite with the highest nominal Sn content.

HAADF-STEM micrographs and elemental maps of these composite materials are presented in Figure 19. The patterns of Ti, Sn, and O almost coincide, indicating the success of the mixed oxide preparation. In particular, Ti/Sn ratios measured on the nanorod-like crystallites or their flower-like agglomerates coincided very well with the nominal composition data (9:1 for 75Sn01/A/600, 4:1 for 75Sn02/A/600 and 2-2.5:1 for 75Sn03/A/600). However, it is not excluded that certain amount of tin is also distributed over the carbon.

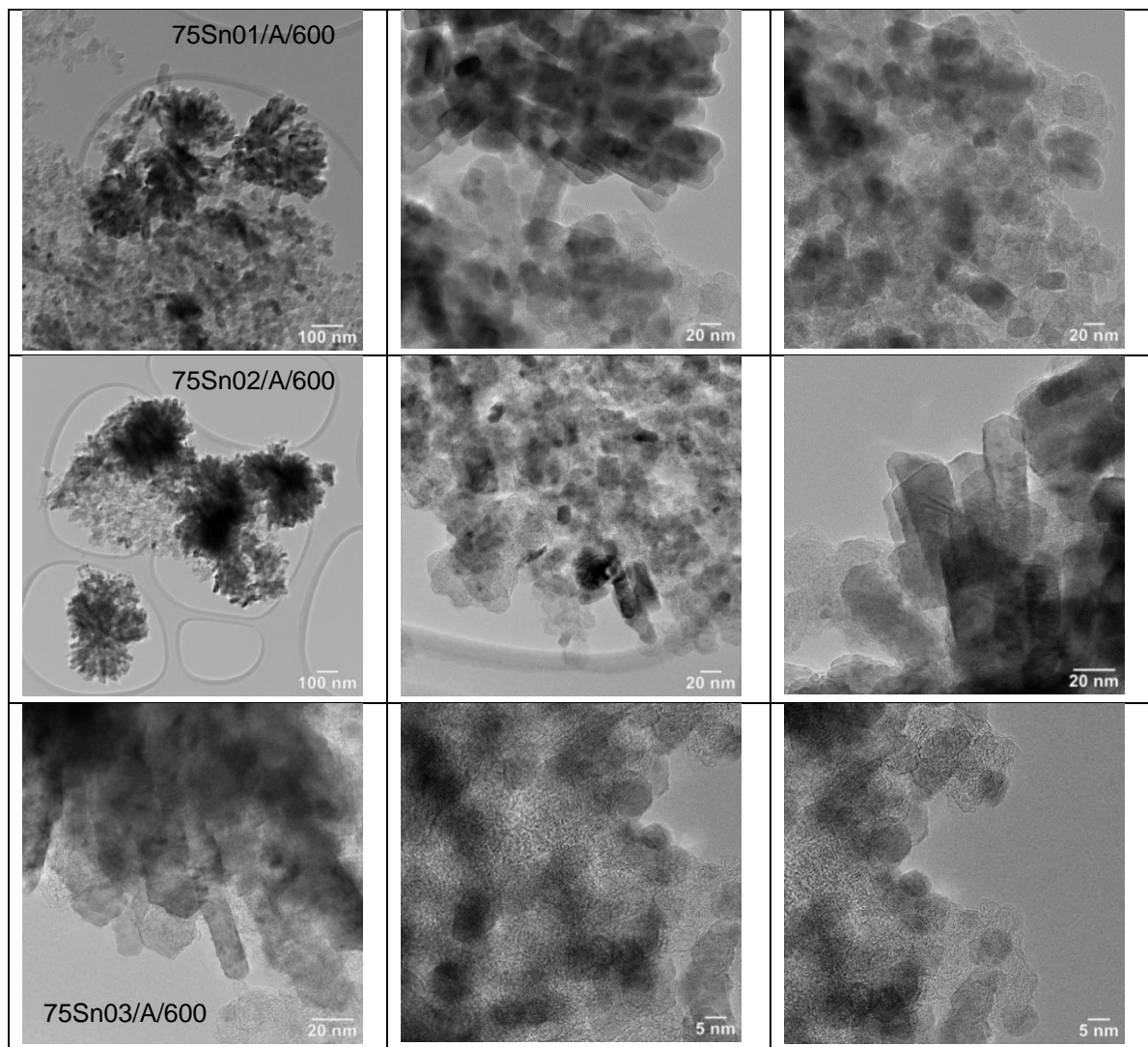


**Figure 18.** TEM images of the 75 wt.%  $\text{Ti}_{(1-x)}\text{Sn}_x\text{O}_2$ -25 wt.% C composite materials: 75Sn01/A/600 (at the top), 75Sn02/A/600 (in the middle) and 75Sn03/A/600 (at the bottom).

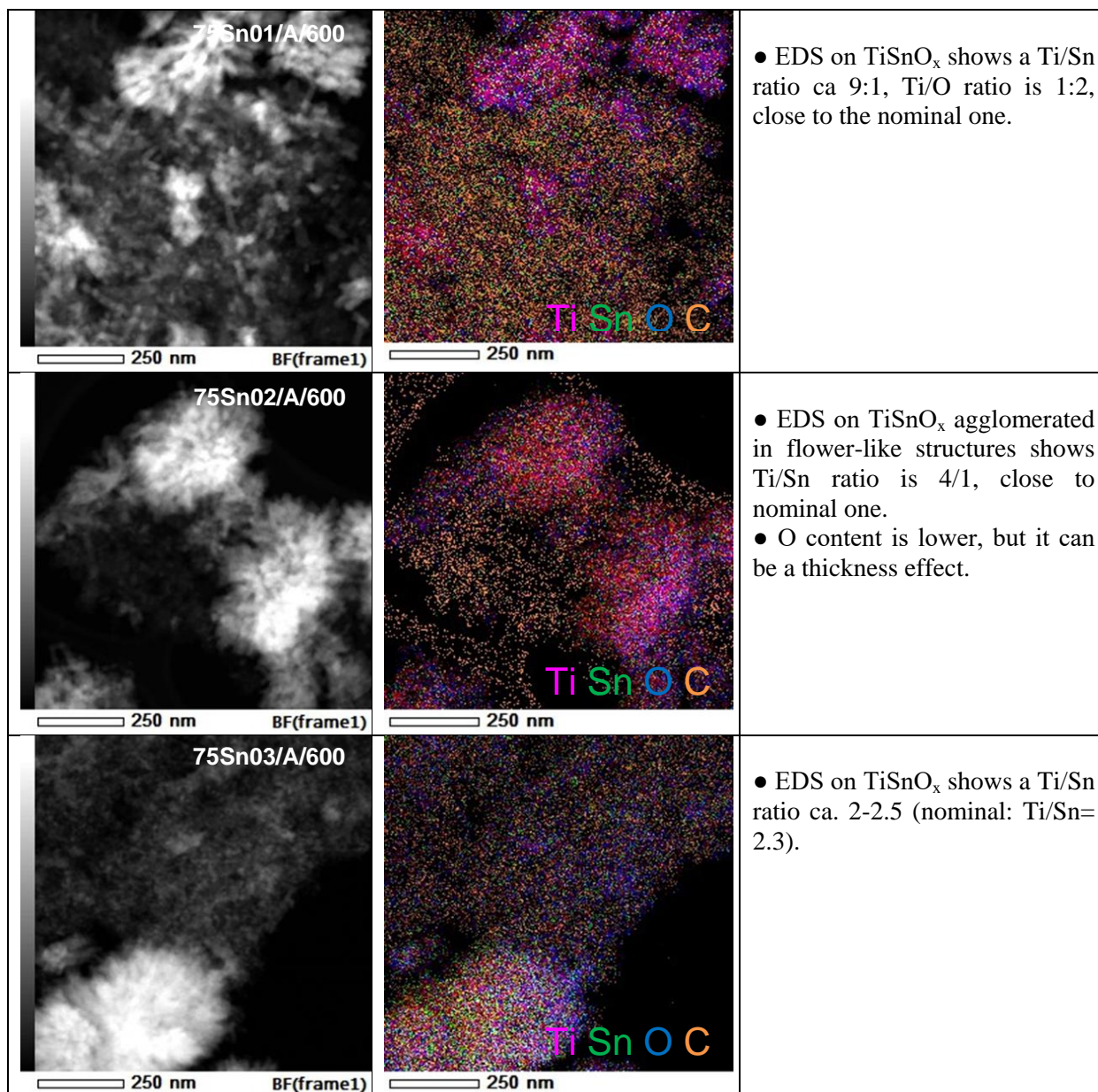


**Figure 19.** HAADF STEM micrographs and overview images of the 75 wt.%  $\text{Ti}_{(1-x)}\text{Sn}_x\text{O}_2$ -25 wt.% C composite materials: 75Sn01/A/600 (at the top), 75Sn02/A/600 (in the middle) and 75Sn03/A/600 (at the bottom).

TEM images of the  $\text{Pt/Ti}_{(1-x)}\text{Sn}_x\text{O}_2$ -C ( $x$ : 0.1-0.3) electrocatalysts are presented in Figure 20. The morphological features of the non-platinized composites were well recognizable: the anisotropic rod-like oxide crystallites and the flower-like agglomerates were easily observable, while EDS analysis (Figure 21) demonstrated the presence of tin and titanium also in areas not covered by these large oxide assemblies. The latter regions can be identified as those containing the relatively homogeneous oxide-carbon mixture. The appearance of well dispersed, uniformly distributed 2-4 nm sized Pt particles on the surface of all catalysts studied was evidenced (see Figure 20) consistent with XRD results (Figure 17.C). According to electron diffraction, these Pt features are metallic nanoparticles. The Pt particles are present on both the large oxide features and between them, where they are in contact with the smaller, more homogeneously distributed oxide particles. Sometimes, especially in connection with the  $\text{TiSnO}_x$  nanorods, raspberry-like aggregations or larger clusters formed from

agglomerated Pt nanoparticles were also observed. The elemental distribution pattern of Pt shown in Figure 21 confirmed that Pt settled on both the large mixed oxide features and on the more homogeneous parts of the composite support. Nevertheless, as shown in Figure 21, areas exist where Pt and the Sn doping element is in close proximity to each other providing the favourable interaction for bifunctional mechanism.

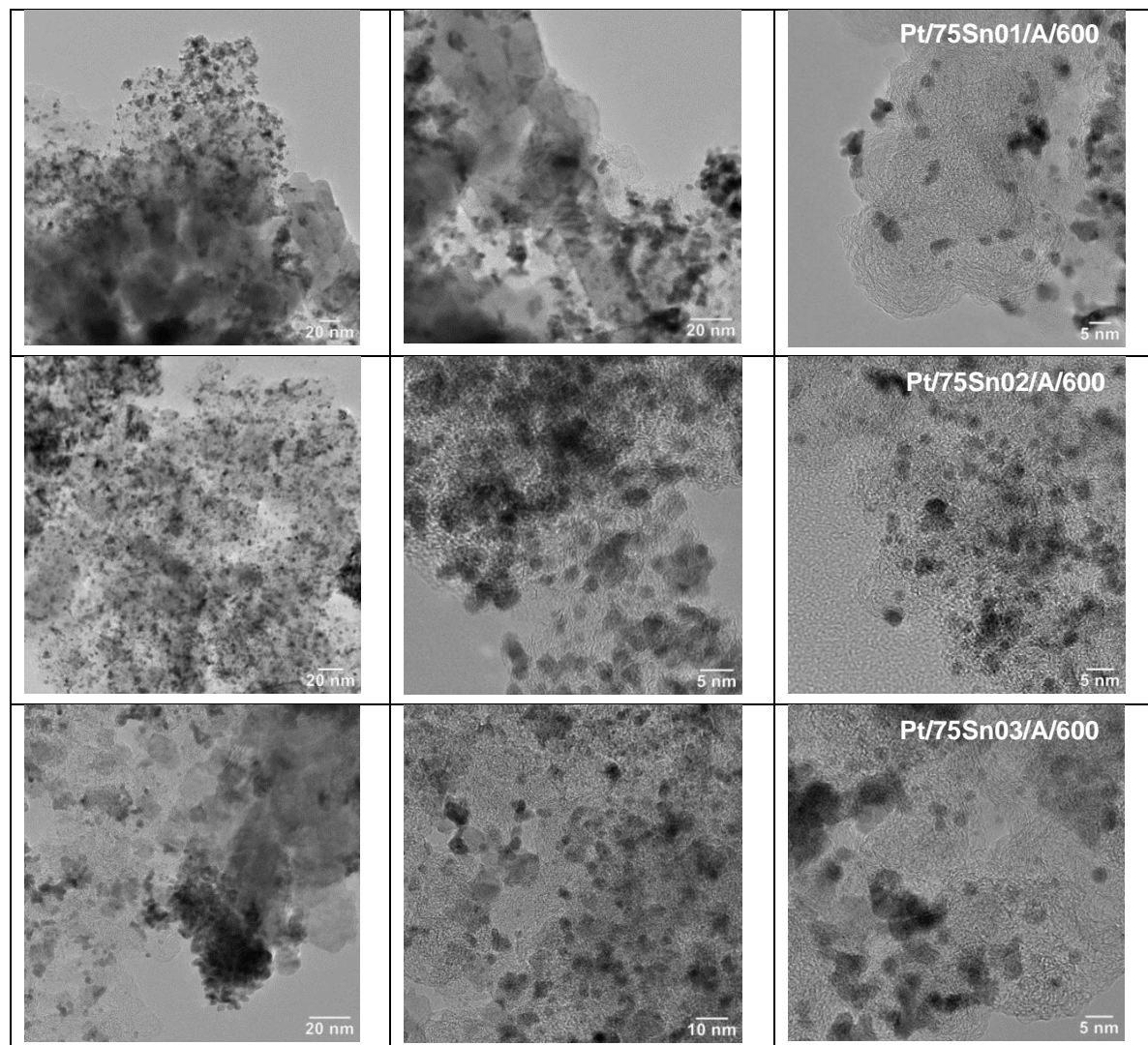


**Figure 20.** TEM images of the 20 wt. Pt/75 wt.%  $\text{Ti}_{(1-x)}\text{Sn}_x\text{O}_2$ -25 wt.% C electrocatalysts: Pt/75Sn01/A/600 (at the top), Pt/75Sn02/A/600 (in the middle) and Pt/75Sn03/A/600 (at the bottom).

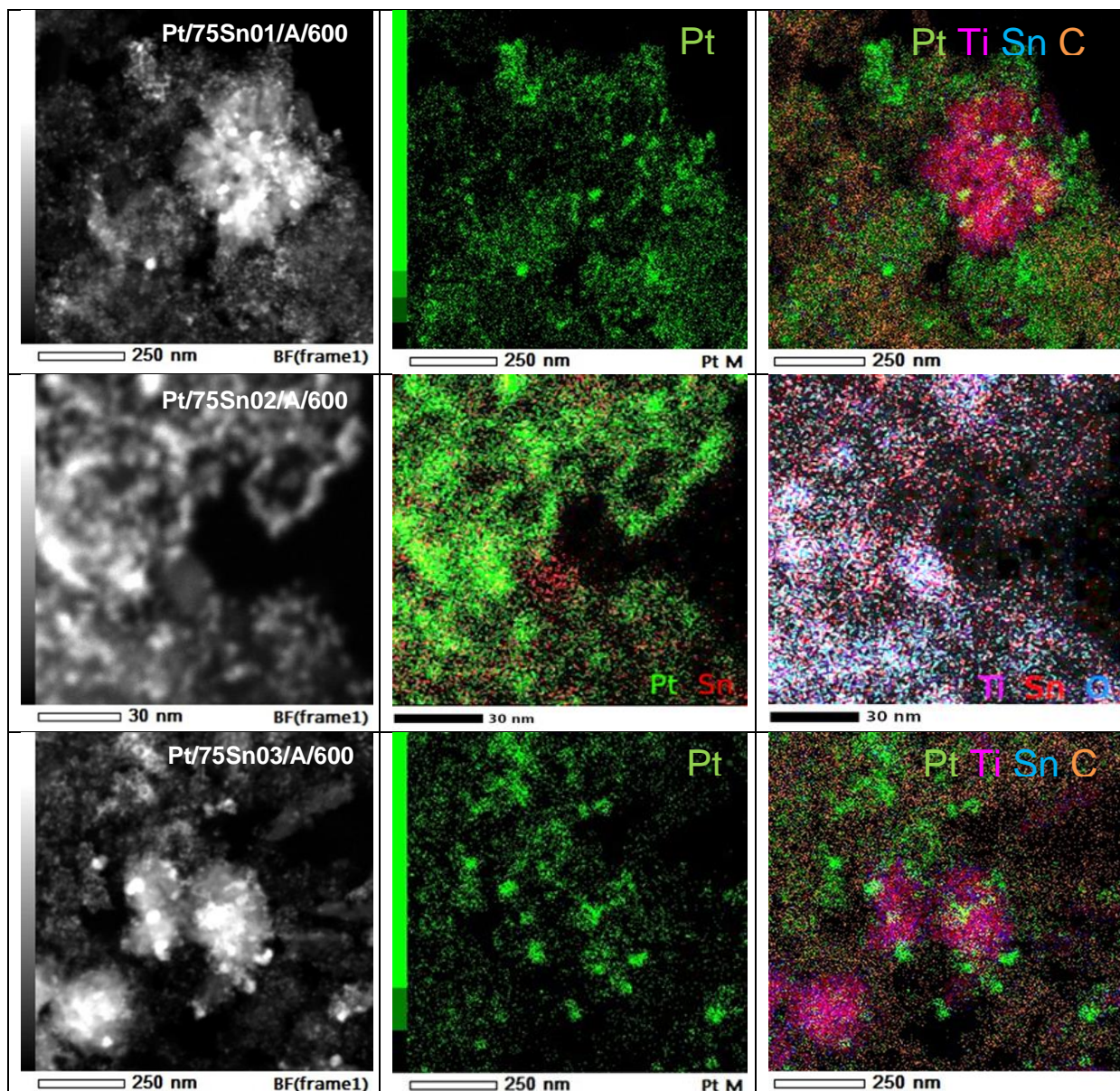


**Figure 21.** HAADF STEM micrographs and overview images of the 20 wt. Pt/75 wt.%  $\text{Ti}_{(1-x)}\text{Sn}_x\text{O}_2$ –25 wt.% C composite materials: Pt/75Sn01/A/600 (at the top), Pt/75Sn02/A/600 (in the middle) and Pt/75Sn03/A/600 (at the bottom).

An overview over the data obtained from TEM analysis is summarized below:

- all samples contain carbon and mixed oxide  $\text{TiSnO}_x$  crystals;
- amorphous carbon is present in the form of spherical balls;
- $\text{TiSnO}_x$  crystals usually grouped in big formations (mostly flower-like), while small, quasi-spherical oxide particles form a more homogeneous coverage on carbon between them;
- The morphology of the Pt-loaded catalysts is similar to their bare composite counterparts. Pt is present as ~2-4 nm nanoparticles, uniformly distributed on both the large oxide features and on the more homogeneous regions. Sometimes Pt particles have a tendency to cluster on the large mixed oxide  $\text{TiSnO}_x$  formations;
- $\text{TiSnO}_x$  have the expected Ti/Sn stoichiometry. Usually the  $\text{TiSnO}_x$  is O-deficient, but it can be only a detection effect due to thickness.

### 5.1.4. SEM/EDX measurements

Scanning electron micrographs of the samples were recorded with a scanning electron microscope, equipped with an energy dispersive X-ray spectrometer (EDX).

The morphology of the composite materials and related Pt electrocatalyst was investigated by SEM technique (Figures 22-25). The thin film of the sample exhibited a granular structure. The different nanograins on the surface did not have large size variations and a porous structure between different grains was also evident. The elemental composition of these materials was evaluated by analysing different sample regions by EDX technique. SEM micrographs and EDX results obtained on the selected areas of the composite materials and Pt electrocatalysts are shown in Figure 22-23 and 24-25, respectively. EDX results are summarized in Tables 9 and 10.

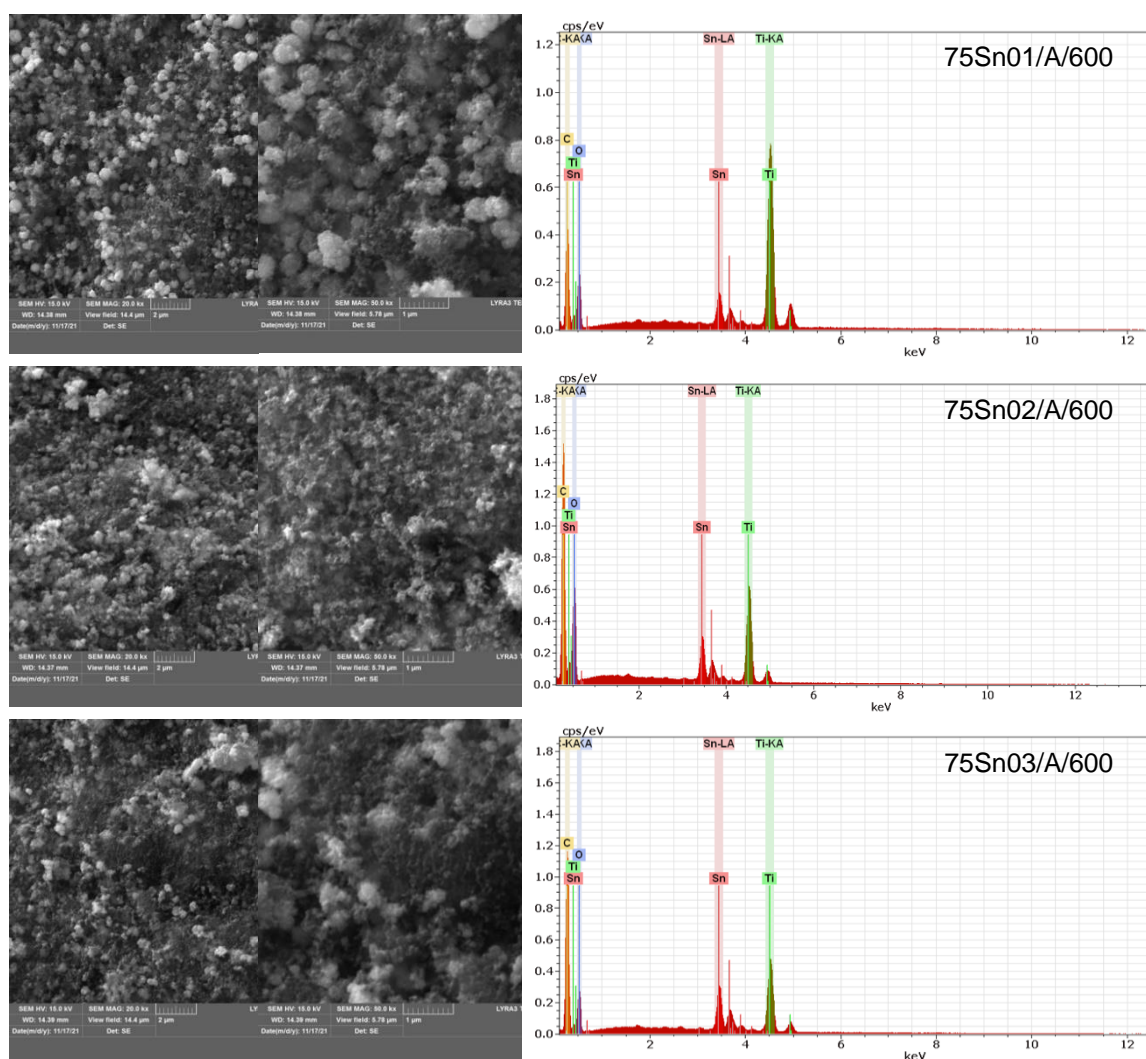


**Figure 22.** SEM micrographs and EDX elemental analysis of the 75 wt.%  $Ti_{(1-x)}Sn_xO_2$ -25 wt.% C composite materials: 75Sn01/A/600 (at the top), 75Sn02/A/600 (in the middle) and 75Sn03/A/600 (at the bottom).

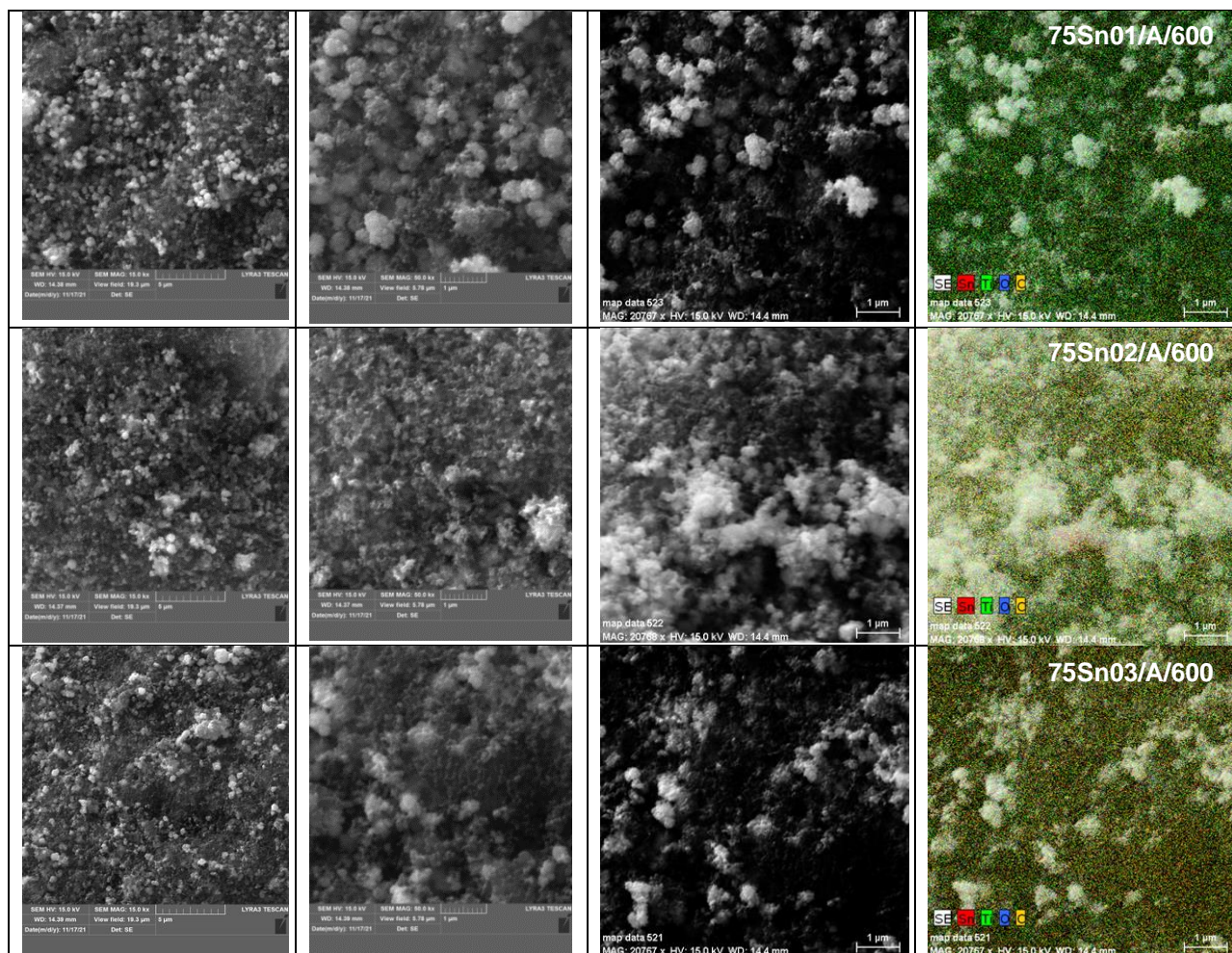


**Figure 23.** SEM micrographs and EDX elemental analysis of the 75 wt.%  $Ti_{(1-x)}Sn_xO_2$ -25 wt.% C composite materials: 75Sn01/A/600 (at the top), 75Sn02/A/600 (in the middle) and 75Sn03/A/600 (at the bottom).

**Table 9.** Characterization of selected areas of the 75 wt.%  $Ti_{(1-x)}Sn_xO_2$ -25 wt.% C composite materials and related Pt catalysts by EDX; the nominal composition is given for comparison.

| Ti/Sn  | Ti (wt.%) |      | Sn (wt.%) |      | O (wt.%) |      | C (wt.%) |      | Pt (wt.%) |      |
|--|-----------|------|-----------|------|----------|------|----------|------|-----------|------|
|  | Nominal   | EDX  | Nominal   | EDX  | Nominal  | EDX  | Nominal  | EDX  | Nominal   | EDX  |
| <b>75 wt.% <math>Ti_{(1-x)}Sn_xO_2</math>-25 wt.% C</b>            |           |      |           |      |          |      |          |      |           |      |
| <b>90/10</b>   | 37.2      | 33.4 | 10.2      | 6.9  | 27.6     | 25.8 | 25.0     | 33.9 | -         | -    |
| <b>80/20</b>   | 30.5      | 26.4 | 18.9      | 11.3 | 25.5     | 21.4 | 25.0     | 40.8 | -         | -    |
| <b>70/30</b>   | 24.9      | 33.8 | 26.4      | 28.1 | 23.7     | 15.5 | 25.0     | 22.6 | -         | -    |
| <b>20 wt.% Pt/75 wt.% <math>Ti_{(1-x)}Sn_xO_2</math>-25 wt.% C</b> |           |      |           |      |          |      |          |      |           |      |
| <b>90/10</b>   | 29.7      | 40.8 | 8.2       | 8.6  | 22.1     | 14.2 | 20,0     | 14.2 | 20.0      | 22.1 |
| <b>80/20</b>   | 24.4      | 24.3 | 15.1      | 11.1 | 20.4     | 33.2 | 20,0     | 12.9 | 20.0      | 18.6 |
| <b>70/30</b>   | 19.9      | 14.5 | 21.1      | 10.7 | 19.0     | 30.6 | 20,0     | 33.7 | 20.0      | 10.6 |

As shown in Table 9, the nominal and measured values of the Pt content for two catalysts with Ti/Sn ratio of 90/10 and 80/20 were in good agreement, but for Pt/75Sn03/A/600 sample the lower

value was determined (see Table 9). However, ICP-OES measurements showed that the content of Pt in the Pt/75Sn03/A/600 sample (Pt= 19.1 wt.%) also fits well to the nominal value.

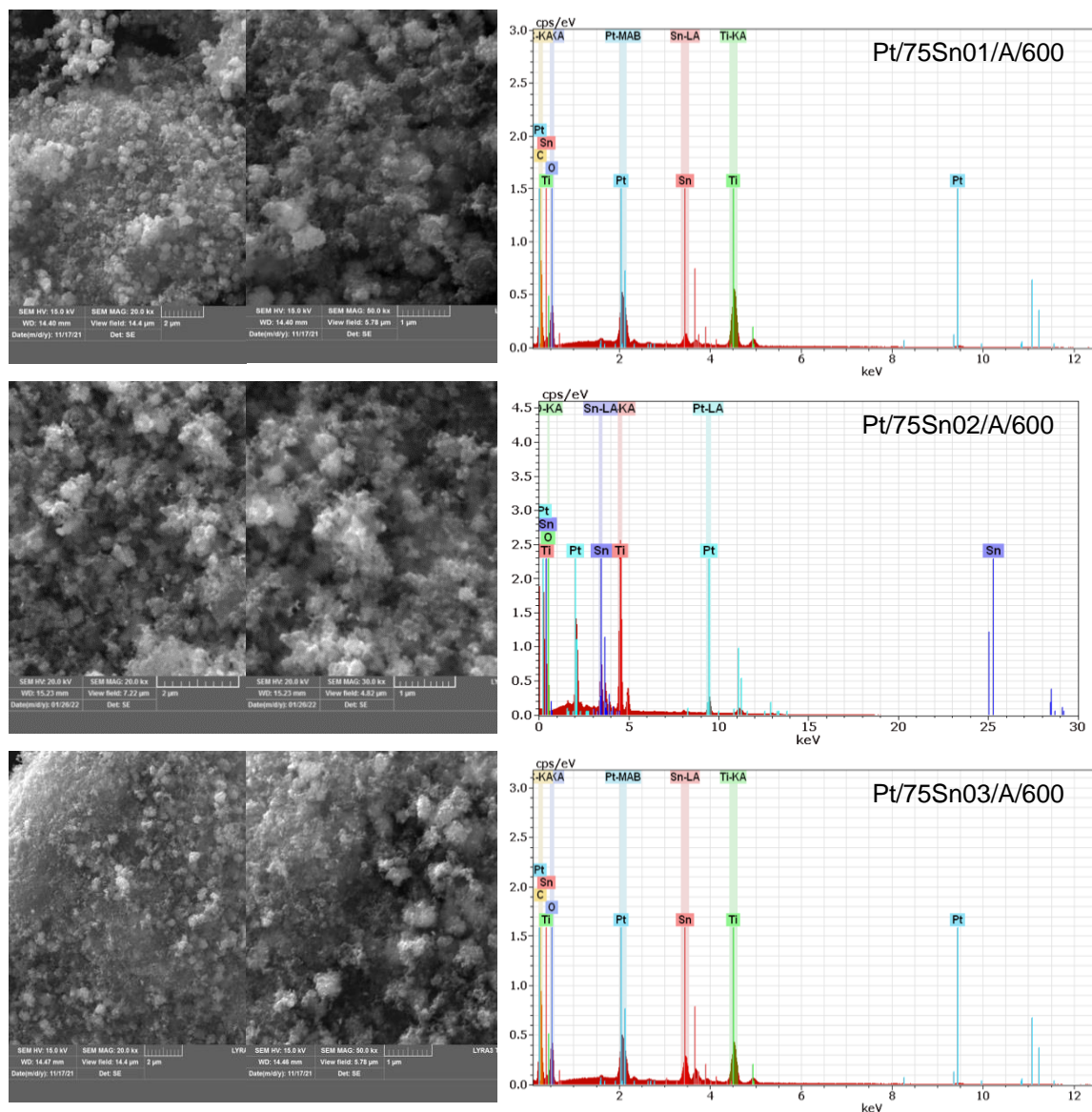


**Figure 24.** SEM micrographs and EDX elemental analysis of the 20 wt.% Pt/75 wt.%  $Ti_{(1-x)}Sn_xO_2$ –25 wt.% C catalysts: Pt/75Sn01/A/600 (at the top), Pt/75Sn02/A/600 (in the middle) and Pt/75Sn03/A/600 (at the bottom).

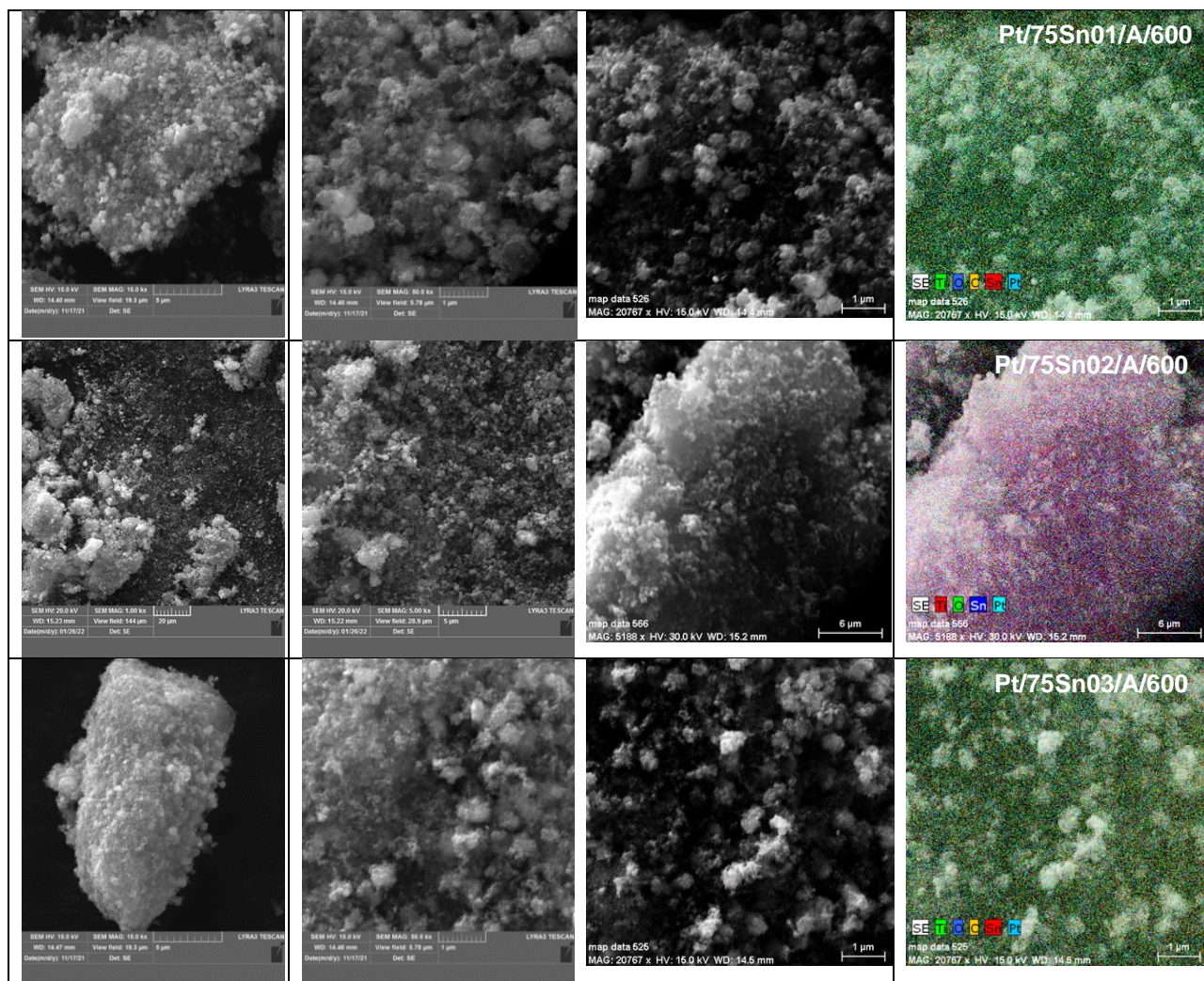


**Figure 25.** SEM micrographs and EDX elemental analysis of the 20 wt.% Pt/75 wt.%  $Ti_{(1-x)}Sn_xO_2$ –25 wt.% C catalysts: Pt/75Sn01/A/600 (at the top), Pt/75Sn02/A/600 (in the middle) and Pt/75Sn03/A/600 (at the bottom).

**Table 10.** Composition of Sn-containing composite materials and 20 wt.% Pt electrocatalysts measured by EDX (in comparison with nominal values).

| Sample ID       | Nominal composition <sup>a,b)</sup>                      | Ti/Sn (at/at) |           | TiSnO <sub>x</sub> /C (wt/wt) EDX | Pt (wt.%)          |
|-----------------|--|---------------|-----------|-----------------------------------|--------------------|
|                 |  | Nominal       | EDX       |                                   |                    |
| 75Sn01/A/600    | Ti <sub>0.9</sub> Sn <sub>0.1</sub> O <sub>2</sub> -C    | 90/10         | 92.3/7.7  | 66.1/33.9                         | -                  |
| 75Sn02/A/600    | Ti <sub>0.8</sub> Sn <sub>0.2</sub> O <sub>2</sub> -C    | 80/20         | 85.3/14.7 | 59.2/40.8                         | -                  |
| 75Sn03/A/600    | Ti <sub>0.7</sub> Sn <sub>0.3</sub> O <sub>2</sub> -C    | 70/30         | 74.9/25.1 | 77.4/22.6                         | -                  |
| Pt/75Sn01/A/600 | Pt/Ti <sub>0.9</sub> Sn <sub>0.1</sub> O <sub>2</sub> -C | 90/10         | 92.2/7.8  | 81.7/18.3                         | 22.1               |
| Pt/75Sn02/A/600 | Pt/Ti <sub>0.8</sub> Sn <sub>0.2</sub> O <sub>2</sub> -C | 80/20         | 84.5/15.5 | 84.2/15.8                         | 18.6               |
| Pt/75Sn03/A/600 | Pt/Ti <sub>0.7</sub> Sn <sub>0.3</sub> O <sub>2</sub> -C | 70/30         | 77.1/22.9 | 62.3/37.7                         | 10.6 <sup>c)</sup> |

<sup>a)</sup> Expected composition of  $Ti_{(1-x)}Sn_xO_2$  mixed oxide reflects desired Ti/Sn atomic ratio;

<sup>b)</sup> In all cases the mass ratio of the mixed oxide to the activated carbon  $Ti_{(1-x)}Sn_xO_2/C$  was 75/25;

<sup>c)</sup> The Pt content is verified by ICP-OES measurements and is 19.1 wt.%.

Ti/Sn ratios calculated from the results of EDX measurements slightly differed from the nominal values. As shown in Table 10, there is some increase in the Ti/Sn ratios when measured values are compared to nominal ones.

This phenomenon is quite unexpected as Sn addition to the samples was a simple impregnation which was followed by a high temperature treatment. Similar loss of doping metal was observed in a case of Mo-containing composite materials; the loss was explained by acidic experimental conditions upon Pt loading [144]. It has been proposed that the decrease of the relative molybdenum content is presumably the consequence of partial dissolution of the less stable Mo species, not incorporated into the lattice, upon Pt deposition. However, as it follows from Table 10, in the case of samples containing tin, there is no significant difference in the Ti/Sn ratios measured by EDX before and after the loading of Pt. A possible reason for the decrease in the Sn content may be the formation of volatile tin compounds during decomposition of tin (IV) chloride pentahydrate during the high temperature treatment.

However, SEM micrographs and EDX measurements confirm the success of uniform deposition of Pt nanoparticles on  $Ti_{(1-x)}Sn_xO_2-C$  composite materials, as already demonstrated on the TEM images.

### 5.1.5. Raman spectroscopy measurements

Figure 26 shows the Raman spectra of the “as prepared” composite materials and selected Pt electrocatalysts with the lowest (Pt/75Sn01/A/600) and the highest Sn content (Pt/75Sn03/A/600) used in this study.

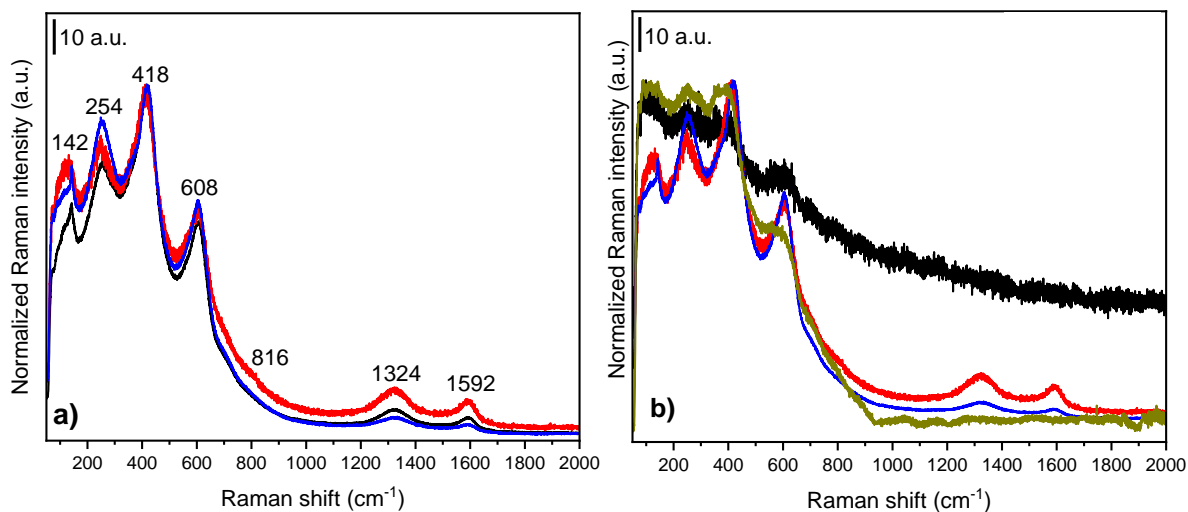


**Figure 26.** Results of Raman spectroscopic measurements: (a) Raman spectra of the tin-containing composite supports: 75Sn01/A/600 (■), 75Sn02/A/600 (■) and 75Sn03/A/600 (■) samples; (b) Comparison of Raman spectra of selected support and supported Pt catalyst pairs: the 75Sn01/A/600 (■), 75Sn03/A/600 (■), Pt/75Sn01/A/600 (■) and Pt/75Sn03/A/600 (■) samples. The used conductive carbon black material was the commercially available Black Pearls 2000 provided by Cabot.

The composites containing 75 wt.% of mixed oxides with different Ti/Sn ratios (see Figure 26.a) and 25 wt.% Black Pearls 2000 carbon present distinct Raman signatures for both Ti–O–Ti and C–C=C bonds. Thus, all spectra show the typical  $TiO_2$  rutile type Raman-active optical phonon modes centered at 142, 418 and 608  $cm^{-1}$  attributed to the  $B_{1g}$ ,  $E_g$  and  $A_{1g}$  modes, respectively. The band located at 254  $cm^{-1}$ , fully developed also in all our Raman spectra, represents a combined line typically

appearing when the degree of distortion is high [166]. The weak high-frequency line of the  $B_{2g}$  symmetry, centered at  $816\text{ cm}^{-1}$ , are poorly observed in our measurements. There are no lines corresponding to the  $\text{SnO}_2$  present in the Raman spectra of these materials. However, the presence of  $\text{SnO}_2$  could not be excluded even if the Raman experiments carried out involved the measurement in several points of each sample.

On the other hand, the presence of graphitic C in the composites has been demonstrated clearly by the corresponding D and G bands for the carbon materials, all spectra showing the first-order Raman lines at  $1324$  and  $1592\text{ cm}^{-1}$  [167,168]. The D band corresponds to the disordered graphitic lattices usually assigned to K-point phonons of  $A_{1g}$  symmetry, while the G band is a signature of an ideal graphitic lattice, this former band being assigned to the Raman-active  $E_{2g}$  mode for the tangential in-plane stretching vibrations of the  $sp^2$ -hybridized bond [169]. As known, the  $I_D/I_G$  ratio is a measure of the degree of defects present in the sample and the in-plane crystalline size of the sample [170]. Thus, the calculated  $I_D/I_G$  ratios of 75Sn01/A/600 ( $\text{Ti}_{0.9}\text{Sn}_{0.1}\text{O}_2\text{-C}$ : 1.41) and 75Sn02/A/600 ( $\text{Ti}_{0.8}\text{Sn}_{0.2}\text{O}_2\text{-C}$ : 1.34) are higher than that of the 75Sn03/A/600 ( $\text{Ti}_{0.7}\text{Sn}_{0.3}\text{O}_2\text{-C}$ : 1.29), suggesting that the former sample has a higher degree of disorder, it possessing more defects and dislocations than the other two materials. It is important to observe that all samples show a high degree of disorder that normally is characterized by a broader G band as well as a broader D band of higher relative intensity compared to that of the G band [168]. The in-plane crystallite size ( $L_a$ ) of the samples calculated from the Tuinstra-Koenig relation [170] ( $L_a\text{ (nm)} = (2.4 \times 10^{-10}) \lambda^4 (I_D/I_G)^{-1}$ ), where  $\lambda$  is the Raman excitation wavelength ( $633\text{ nm}$  in our case), were found to be  $27\text{ nm}$ ,  $29\text{ nm}$  and  $30\text{ nm}$  for the 75Sn01/A/600, 75Sn02/A/600 and 75Sn03/A/600, respectively.

As shown in Figure 26.b, the introduction of metallic Pt onto the composites dramatically changed the Raman spectra, the C-based signature almost disappearing. It can be imagined that Pt settled not only on the  $\text{Ti}_{(1-x)}\text{Sn}_x\text{O}_2$  mixed oxides but also on the carbonaceous part, disturbing its symmetry. Another, less likely option is that local hydrogenation of the aromatic system occurred when the metal Pt was formed during the reduction step.

#### **5.1.6. X-ray photoelectron spectroscopy (XPS) examination**

To complete the described investigations, XPS studies were performed on selected composite support and electrocatalyst samples. Comparison of the results from bulk-sensitive measurements and surface specific XPS allows to explore further details of the microstructure of the composite supports and catalysts.

Figure 27 shows the X-ray photoelectron survey spectrum of the Pt/75Sn01/A/600 electrocatalyst.

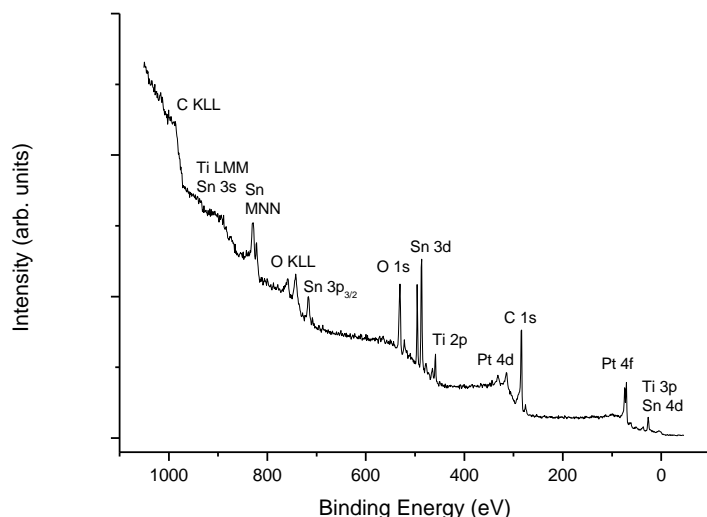


**Figure 27.** Survey spectrum of the Pt/75Sn01/A/600 electrocatalyst

The sample – similarly to all of the studied  $\text{TiSnO}_x\text{-C}$  composites and Pt-loaded electrocatalysts supported on them – contained only the expected elements Ti, Sn, O, C and Pt.

The chemical states of the components were also rather similar in all studied samples, therefore their brief description is given here. The Pt content of the catalysts was always predominantly metallic as indicated by the Pt  $4f_{7/2}$  binding energy around 71.2-71.3 eV. The literature binding energy for metallic Pt is around 71.1-71.3 eV [151]. Only traces of ionic Pt were detected:  $\text{Pt}^{2+}$  around 72.6 eV and  $\text{Pt}^{4+}$  around 75 eV, arising from the air exposure of the catalysts. Their amount was not larger than 2-3% of the total Pt content. The Ti content of all samples was always fully oxidized with the Ti  $2p_{3/2}$  peak around 459.0-459.1 eV, which corresponds to literature data for  $\text{Ti}^{4+}$  in oxide [151]. The C 1s spectrum of the samples was predominantly similar to that of the Black Pearls 2000 carbon backbone: a graphite-like asymmetric line shape (main peak at 284.4 eV) was accompanied by small contributions from oxygen-containing functional groups (carbon singly bound to oxygen like in C-OH, C-O-C arrangements around 286 eV and strongly oxidized carbon species like carboxylic groups around 289 eV). The amount of oxidized carbon species was around 3-5% of the total carbon content. The O 1s spectrum was consistent with the spectra of the other components. The main component was observed around 530.3-530.5 eV binding energy, due to lattice oxygen in metal oxides. A high binding energy tail region to this peak contained contributions from -OH groups on the metal oxide and/or from the C-O-C type environments located around 531-532 eV binding energy. Another component around 532.5-533 eV was tentatively assigned to C-OH groups and moisture adsorbed on the surface from atmospheric exposure. On the other hand, the Sn 3d spectra were a little more complex and varied somewhat between the samples. The dominant Sn  $3d_{5/2}$  contribution was always observed around 487.0 eV binding energy, which pointed to the presence of  $\text{Sn}^{4+}$  species in oxide environment [151]. The 431.6-431.8 eV kinetic energy of the Sn  $\text{M}_4\text{N}_{45}\text{N}_{45}$  Auger peak, and the 918.7-918.9 eV value of the resulting Auger parameter (the sum of the Sn  $3d_{5/2}$  binding energy and the Sn  $\text{M}_4\text{N}_{45}\text{N}_{45}$  kinetic energy) confirmed this assignment, as they were exactly the same as observed previously for  $\text{Sn}^{4+}$  in native tin oxide or electrochemically formed tin oxide. Nevertheless, the Sn 3d peaks often contained a certain asymmetry on their low binding energy side, which suggested the presence of more reduced tin species. For separation of this contribution, a careful removal of the satellite feature arising from the Sn  $3d_{3/2}$  peak excited by the  $\text{MgK}\alpha_{3,4}$  X-ray satellite was performed, which increased the unreliability of the intensity of this reduced component. Accordingly, often it seemed to be more

appropriate to give an upper limit for this contribution, as it is shown in the tables detailing the results. Curve fitting revealed that this low binding energy contribution typically arises around 485 eV binding energy, which indicated the presence of metallic tin [151].

Because of the general similarity of the chemical states for C, O, Ti and Pt, they will not be further discussed, while the behavior of Sn will be mentioned when describing the properties of the particular samples.

In contrast with the chemical states, the surface concentration of the components varied in a characteristic way indicating the influence of the preparation route on the microstructure of the composite supports.

Table 11 summarizes the composition results obtained on supports and electrocatalysts by preparation route A. A general feature of all samples was that the oxide/carbon ratio strongly deviated from the nominal value: the apparent carbon content deduced from the XPS spectra was much higher than expected. EDX data (Table 10) indicated the same tendency although to a somewhat smaller extent. The phenomenon of unexpectedly high apparent carbon content was also observed in the case of Mo-doped titania-carbon composites, especially at high nominal oxide contents and was traced to the co-existence of large, flower-like oxide agglomerates with much more dispersed ones, i.e., to the significant inhomogeneity of the composite [143,171]. TEM analysis of the composites prepared by route A convincingly demonstrated this kind of inhomogeneity also in the  $Ti_{(1-x)}Sn_xO_2-C$  systems. In a supporting experiment, a simulated high temperature treatment was carried out on the 75Sn02/A composite between 300 °C and 600 °C in Ar in the preparation chamber of the electron spectrometer. Thus, surface chemistry changes of the composite were followed without air exposure. In this experiment the gradual increase of the apparent carbon content with increasing temperature of HTT was observed, which confirms that the high carbon content deduced from XPS data is the result of oxide sintering.

**Table 11.** Surface composition data obtained on selected samples containing composites prepared by route A.

| Sample ID                  | Nominal composition     | Nominal Ox/C <sup>a)</sup> | XPS Ox/C <sup>b)</sup> | XPS Ti/Sn | Metallic Sn fraction <sup>c)</sup> | XPS Pt/support ratio <sup>d)</sup> |
|----------------------------|-------------------------|----------------------------|------------------------|-----------|------------------------------------|------------------------------------|
| 75Sn02/A/600 <sup>e)</sup> | $Ti_{0.8}Sn_{0.2}O_2-C$ | 75/25                      | 52/48                  | 1.17:1    | 10%                                | --                                 |
| Pt/75Sn01/A/600            | $Ti_{0.9}Sn_{0.1}O_2-C$ | 75/25                      | 55/45                  | 0.75:1    | 3%                                 | 27/73                              |
| Pt/75Sn02/A/600            | $Ti_{0.8}Sn_{0.2}O_2-C$ | 75/25                      | 57/43                  | 0.57:1    | 3%                                 | 31/68                              |

<sup>a)</sup> Ox/C:  $Ti_{(1-x)}Sn_xO_2/C$  mass ratio (wt.%/wt.%);

<sup>b)</sup> calculated without the Pt content;

<sup>c)</sup> with respect to the total tin content;

<sup>d)</sup> Pt/support ratio: Pt/ $Ti_{(1-x)}Sn_xO_2-C$  mass ratio (wt.%/wt.%);

<sup>e)</sup> data estimated from the results of the 600 °C step of the *in situ* simulated HTT series in the electron spectrometer.

Another common feature of the composites prepared by route A was the very high surface tin content. While Ti/Sn ratios measured by EDX were close to the nominal values, the apparent Sn content found by XPS was the same or even significantly higher than the Ti content. It can be explained by the surface enrichment of tin, i.e. a tin oxide-rich overlayer covering relatively high areas of the support. Data on the 75Sn02/A/600 composite and its platinized counterpart suggested that instead of tin dissolution, some further surface enrichment may have occurred during Pt loading. This

result is in qualitative agreement with the SEM/EDX data which also indicated lack of tin dissolution upon Pt loading. As a result of the high surface concentration of Sn in these systems, significant influence of the Sn-Pt interactions on the electrocatalytic behavior can be expected.

Although the vast majority of tin was in the Sn<sup>4+</sup> state both in the 75Sn02/A/600 composite and the two electrocatalysts, a small metallic contribution was evident in all cases. It must be noted that the data for the non-platinized composite were collected during the simulated HTT experiment, thus they represent a different situation than the air-exposed case obtained after the regular HTT. While the XPS results on the presence of metallic tin are in qualitative agreement with XRD observations made on the non-platinized composites, the much larger metallic Sn content found by XPS is probably due to the lack of air exposure. Formation of metallic tin was observed already after the 400 °C annealing step in the simulated HTT experiment, confirming that tin reduction is indeed the by-product of the HTT in these systems. As metallic tin was present already in the non-platinized composites, it is difficult to determine how appearance of metallic tin in the Pt-loaded electrocatalysts is related to direct Pt-Sn interactions.

## 5.2. Route A - electrochemical characterization of the 20 wt.% Pt/Ti<sub>(1-x)</sub>Sn<sub>x</sub>O<sub>2</sub>-C electrocatalysts

Electrocatalytic performance of the catalysts was studied by cyclic voltammetry and CO<sub>ads</sub>-stripping voltammetry measurements combined with stability test involving 500 and 10,000 polarization cycles (see Table 12 and Figure 28-32).

**Table 12.** Electrochemical performance of the reference Pt/C and Pt/75 wt.% Ti<sub>(1-x)</sub>Sn<sub>x</sub>O<sub>2</sub>-25 wt.% C electrocatalysts.

| Sample          | E <sub>CO,onset</sub> , <sup>a)</sup><br>mV | E <sub>CO,max</sub> , <sup>b)</sup> mV | ECSA <sub>1</sub> , <sup>c)</sup><br>m <sup>2</sup> /g <sub>Pt</sub> | ΔECSA <sub>500</sub> ,<br>% <sup>d)</sup> | ΔECSA <sub>10,000</sub> ,<br>% <sup>d)</sup> |
|-----------------|---|--|--|---|--|
| Pt/75Sn01/A/600 | 245   | 765 ( <i>sh</i> : 705)                 | 32.7 ± 2.5   | 7.8                                       | 39.0   |
| Pt/75Sn02/A/600 | 245   | 775 ( <i>sh</i> : 705)                 | 33.6 ± 2.4   | 9.9                                       | -  |
| Pt/75Sn03/A/600 | 245   | 765 ( <i>sh</i> : 705)                 | 31.6 ± 2.7   | 15.9                                      | -  |
| Pt/C            | 625   | 795                                    | 87.2 ± 2.3   | 12.7 <sup>e)</sup>                        | 47.8   |

<sup>a)</sup> The onset potential for the CO electrooxidation;

<sup>b)</sup> The position of the main CO stripping peak measured on fresh catalysts;

<sup>c)</sup> The average ECSA value obtained on fresh catalysts in four parallel measurements;

<sup>d)</sup> ΔECSA<sub>500</sub> and ΔECSA<sub>10,000</sub> were calculated from the charges originated from the hydrogen desorption in the 1<sup>st</sup> and 500<sup>th</sup> or 10,000<sup>th</sup> cycles according to the Equation 10 (see Experimental part);

<sup>e)</sup> ΔECSA<sub>500</sub> value was calculated from the 10,000-cycle stability measurements;

*sh*= shoulder.

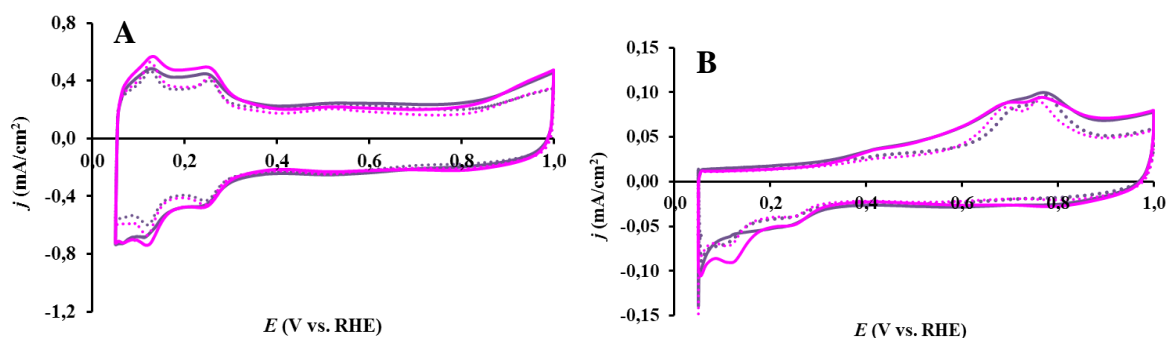


**Figure 28.** Cyclic voltammograms (A) and  $\text{CO}_{\text{ads}}$  stripping voltammograms (B) of the Pt/75Sn01/A/600 catalyst obtained on fresh catalysts (solid lines) and after stability test (dotted lines) in 0.5 M  $\text{H}_2\text{SO}_4$ . The reproducibility of the measurements was demonstrated by different colors. Pt loading of the electrodes was  $10 \mu\text{g}/\text{cm}^2$ . Sweep rate: (A) 100 mV/s and (B) 10 mV/s,  $T = 25^\circ\text{C}$ .

An example of good reproducibility of the measurements obtained on Sn-containing composite supported Pt catalysts is shown in Figure 28.

Electrochemical performance of the catalysts with different Sn content in  $\text{Ti}_{(1-x)}\text{Sn}_x\text{O}_2\text{-C}$  ( $x$ : 0.1-0.3) composite supports was demonstrated in Figure 29. In the cyclic voltammograms of Figure 29.A the region between 50 to 350 mV contains the typical adsorption/desorption peaks of underpotentially deposited hydrogen on the Pt surface. As can be seen from Figure 29.A the 500-cycle stability test results in only a minimal decrease of the current density associated with adsorption/desorption of underpotentially deposited hydrogen. Despite a slight decrease of the electrochemically active Pt surface area (ECSA), the electrochemical double-layer region remained practically unchanged, indicating good stability of the Sn-containing composite support materials.

As shown in Figure 29.B,  $\text{Ti}_{(1-x)}\text{Sn}_x\text{O}_2\text{-C}$  composite supported Pt electrocatalyst shows enhanced CO tolerance: the CO started to be oxidized at about  $E_{\text{CO, onset}} = 245 \text{ mV}$ . The position of the maximum of the main CO oxidation peak observed on the  $\text{CO}_{\text{ads}}$  stripping curves for various Pt/ $\text{Ti}_{(1-x)}\text{Sn}_x\text{O}_2\text{-C}$  electrocatalysts is summarized in Table 12. On Sn-containing composite supported catalysts two overlapping  $\text{CO}_{\text{ads}}$ -electrooxidation peaks at around 705 and 765-775 mV were observed (see Figure 29.B and Table 12). It should be noted that in the case of the reference Pt/C catalyst, the corresponding peak was at about 795 mV (see Table 12) [143].

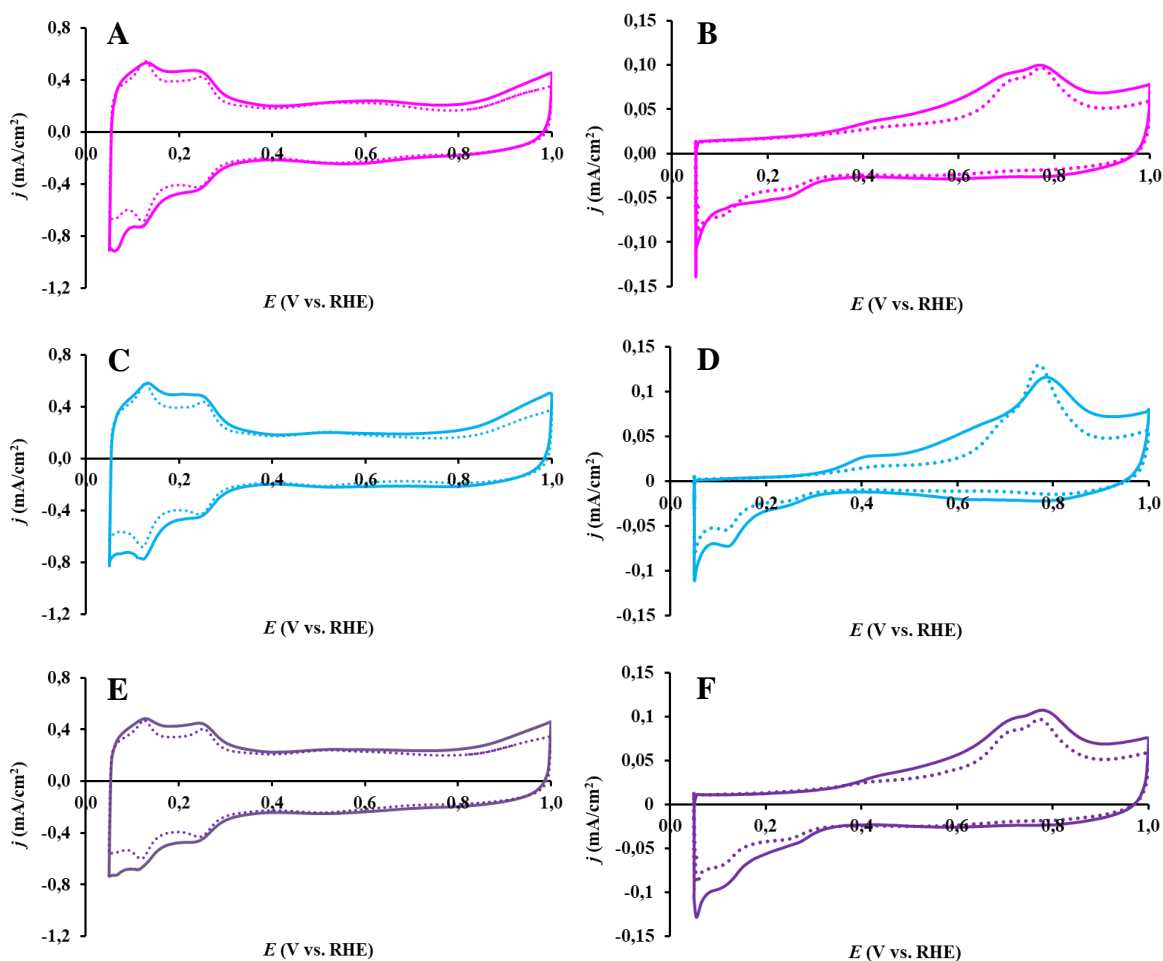


**Figure 29.** Cyclic voltammograms (A, C, E) and  $\text{CO}_{\text{ads}}$  stripping voltammograms (B, D, F) of the 20 wt.%  $\text{Pt}/\text{Ti}_{(1-x)}\text{Sn}_x\text{O}_2\text{-C}$  electrocatalysts obtained on fresh samples (solid lines) and after 500 cycle stability test (dotted lines) in 0.5 M  $\text{H}_2\text{SO}_4$ : Pt/75Sn01/A/600 (A, B), Pt/75Sn02/A/600 (C, D) and Pt/75Sn03/A/600 (E, F) catalysts. Pt loading of the electrodes was  $10 \mu\text{g}/\text{cm}^2$ . Sweep rate: (A, C, E) 100 mV/s and (B, D, F) 10 mV/s,  $T = 25^\circ\text{C}$ .

As shown in Figure 30, the electrochemical performance of the electrocatalysts did not depend on the nominal Ti/Sn ratio in composite materials. The  $\text{CO}_{\text{ads}}$  stripping voltammograms obtained on different catalysts were very similar; the observed difference is within the reproducibility of electrochemical measurements (see Figure 30.A). This behavior can be explained by the surface nature of non-incorporated amorphous tin/tin oxide located on the surface of the composite materials, as suggested by the XPS data. The presence of a thin highly dispersed layer of tin oxide covering the surface of all composites, regardless of the nominal Ti/Sn ratio, is probably the reason for the independence of the activity of the catalysts from the content of tin introduced into the  $\text{TiO}_2$ -lattice in the mixed oxide.

After 500 cycles of the stability test a small shift of the main CO stripping peak by ca. 10 mV toward less positive potential values in comparison to that obtained over fresh samples was observed only on the Pt/75Sn02/A/600 sample (Figures 29.D and 30.B). This kind of shift can be an indication of the agglomeration of Pt nanoparticles [172].

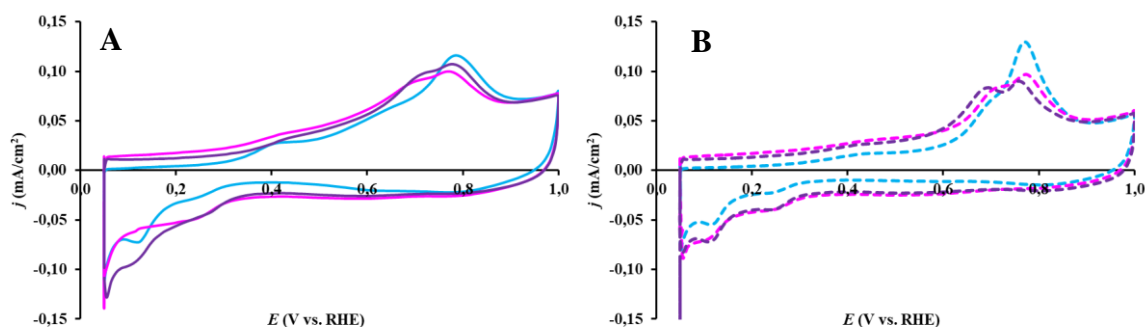


**Figure 30.** Influence of the Ti/Sn ratios of composite support materials on the electrochemical performance of the corresponding Pt catalysts.  $\text{CO}_{\text{ads}}$  stripping voltammograms of the Pt/75Sn01/A/600 (■), Pt/75Sn02/A/600 (■) and Pt/75Sn03/A/600 (■) electrocatalysts obtained before (A) and after the 500-cycle stability test (B). Recorded in 0.5 M  $\text{H}_2\text{SO}_4$  at 10 mV/s,  $T = 25^\circ\text{C}$ .

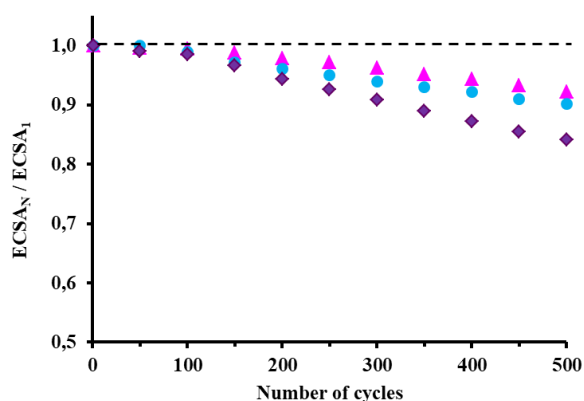


**Figure 31.** ECSA change during 500 CV cycles.  $\text{ECSA}_N/\text{ECSA}_1$ : comparison of the ECSA measured after N cycles normalized to ECSA measured in the 1<sup>st</sup> cycle on the 20 wt. Pt/75 wt.%  $\text{Ti}_{(1-x)}\text{Sn}_x\text{O}_2$ -25 wt.% C electrocatalysts as a function of the number of cycles (N): Pt/75Sn01/A/600 (▲), Pt/75Sn02/A/600 (●) and Pt/75Sn03/A/600 (◆) catalysts.

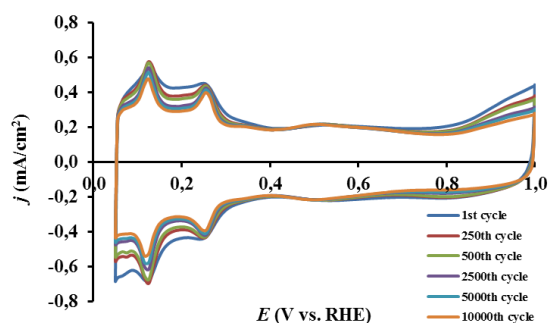


**Figure 32.** The results of the electrochemical 10,000-cycle stability test of the Pt/75Sn01/A/600 catalyst.

As shown in Figure 31, the stability of the Sn-containing composite supported Pt electrocatalysts decreased with increasing tin content in the composite materials. Similar tendency was observed on Mo-containing 20 wt.% Pt/75 wt.%  $\text{Ti}_{(1-x)}\text{Mo}_x\text{O}_2$ -25 wt.% C composite supported catalysts with Ti/Mo= 80/20, 70/30 and 60/40 ratios [144].

In an additional experiment (see Figure 32), the electrochemical stability was also studied for 10,000 cycles by cyclic polarization of the Pt/75Sn01/A/600 catalyst in Ar purged 0.5 M  $\text{H}_2\text{SO}_4$

solution between 50 and 1000 mV potential limits with 100 mV s<sup>-1</sup> sweep rate. As shown in Table 12 the loss in the ECSA<sub>H</sub> during 10,000-cycle stability test was 39.0 %. It should be noted that this value of the ECSA loss was quite comparable with the results recently obtained by the research group on Mo-containing 20 wt.% Pt/75 wt.% Ti<sub>0.8</sub>Mo<sub>0.2</sub>O<sub>2</sub>-25 wt.% C catalysts. As demonstrated in ref. [143] the degradation during the stability test of the Mo-containing BP-based composite supported Pt catalyst with Ti<sub>0.8</sub>Mo<sub>0.2</sub>O<sub>2</sub>/C= 75/25 ratio was a little bit lower ( $\Delta\text{ECSA}_{10,000} = 37.0\%$ ), but higher degradation was observed on Vulcan-based composite supported catalyst ( $\Delta\text{ECSA}_{10,000} = 43.6\%$ ) and reference Pt/C ( $\Delta\text{ECSA}_{10,000} = 47.8\%$ ).

### 5.3. Route B - physicochemical characterization of the Ti<sub>(1-x)</sub>Sn<sub>x</sub>O<sub>2</sub>-C composite support materials and related Pt electrocatalysts

As mentioned in chapter 5.1, first, to obtain a new type of tin-containing composites of various compositions, the technique developed by the research group for Mo-containing composite materials was adapted (route A). This method and the composites obtained in this way had the following drawbacks: (i) the formation of a small amount of metallic Sn phase, which disappears after Pt deposition, (ii) certain inhomogeneity of the composite materials (the formation of TiSnO<sub>x</sub> agglomerated in flower-like clusters), and (iii) relatively low electrochemically active Pt surface area of the catalysts (~30 m<sup>2</sup>/g<sub>Pt</sub>).

To avoid this, the synthesis of the composite was modified: the precursor of Sn was introduced immediately after the formation of the transparent Ti-sol, before the addition of the carbon and the aging step (Figure 6, route B).

In addition, using route B composite materials with high carbon content (75 wt.%) was also prepared (see Figure 7). As shown in Figure 7 the difference between the preparation of two 25Sn02/B/500 and 25Sn02/B-7/500 samples was the duration of the aging step, which was 4 and 7 days, respectively.

Bulk and surface microstructure of the obtained composite materials were characterized by different physicochemical methods including XRD, nitrogen adsorption measurements, TEM, SEM/EDX and XPS.

#### 5.3.1. X-ray powder diffraction (XRD)

As shown in Table 13 XRD revealed that these composites contain pure rutile phase; the formation of Sn<sup>0</sup> or SnO<sub>2</sub> was not observed.

**Table 13.** Structural properties of the Ti<sub>(1-x)</sub>Sn<sub>x</sub>O<sub>2</sub>-C composite materials determined by XRD analysis

| Sample ID      | HTT        |                                   | Lattice parameters, Å <sup>a)</sup> | Sn subst., % |
|----------------|------------|-----------------------------------|-------------------------------------|--------------|
|                | (Phase, %) |                                   |                                     |              |
|                | R/nm       | Sn <sup>0</sup> /SnO <sub>2</sub> |                                     |              |
| 75Sn01/B/500   | 100/18     | -                                 | $a = 4.608, c = 2.975$              | ~9           |
| 75Sn02/B/500   | 100/12     | -                                 | $a = 4.610, c = 2.982$              | ~10          |
| 75Sn03/B/500   | 100/11     | -                                 | $a = 4.625, c = 2.988$              | ~25          |
| 25Sn02/B/500   | 100/9.1    | -                                 | $a = 4.622, c = 3.004$              | ~20          |
| 25Sn02/B-7/500 | 100/10     | -                                 | $a = 4.622, c = 3.004$              | ~20          |

<sup>a)</sup> Lattice parameters of the rutile phase obtained after HTT (pure rutile TiO<sub>2</sub>:  $a = 4.593$  Å,  $c = 2.959$  Å).

XRD patterns of the composite materials with 75 wt.% and 25 wt.% of mixed oxide are shown in Figures 33 and 34, respectively. The measurements confirmed the success of the synthesis: diffraction patterns indicated the exclusive presence of rutile crystallites with slightly altered cell parameters due to Sn incorporation (see Table 13). Broad reflections from Pt and  $\text{Ti}_{(1-x)}\text{Sn}_x\text{O}_2$  mixed oxide demonstrated the presence of well-dispersed oxide and metal nanoparticles. As shown in Table 13 oxides are present in all samples in dispersed form (9.1 - 18 nm). Unfortunately, the relatively high signal/noise ratios make it difficult to accurately determine the cell parameters even in the presence of an internal standard. Therefore, the content of tin incorporated into the  $\text{TiO}_2$  lattice can only be determined approximately.

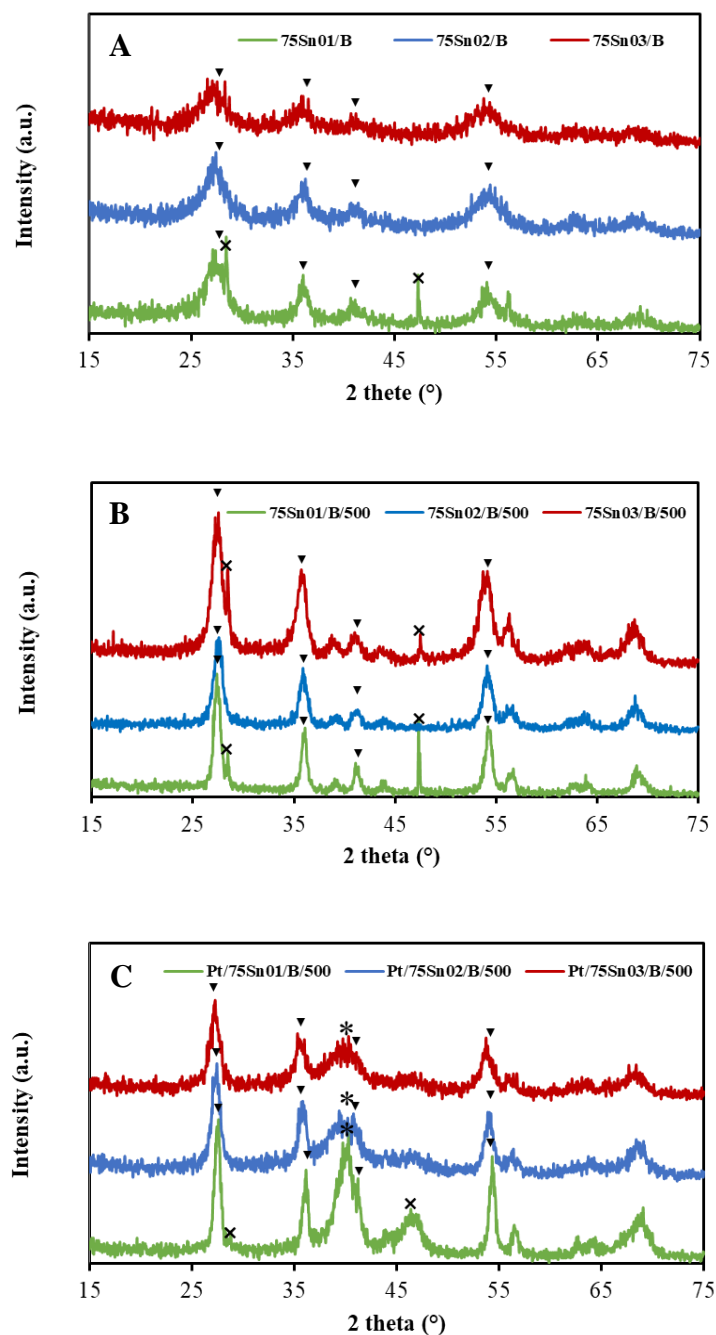


**Figure 33.** XRD patterns of 75 wt.%  $\text{Ti}_{(1-x)}\text{Sn}_x\text{O}_2$  – 25 wt.% C ( $x= 0.1, 0.2$  and  $0.3$ ) composite materials before (A) and after (B) HHT as well as after Pt loading (C):  $\text{Ti}_{0.9}\text{Sn}_{0.1}\text{O}_2$ –C (green),

$\text{Ti}_{0.8}\text{Sn}_{0.2}\text{O}_2\text{-C}$  (blue),  $\text{Ti}_{0.7}\text{Sn}_{0.3}\text{O}_2\text{-C}$  (red-brown). ▼- Rutile, \*- Pt, ×- internal standard (Si: narrow reflections around  $28^\circ$  and  $47^\circ$ ).

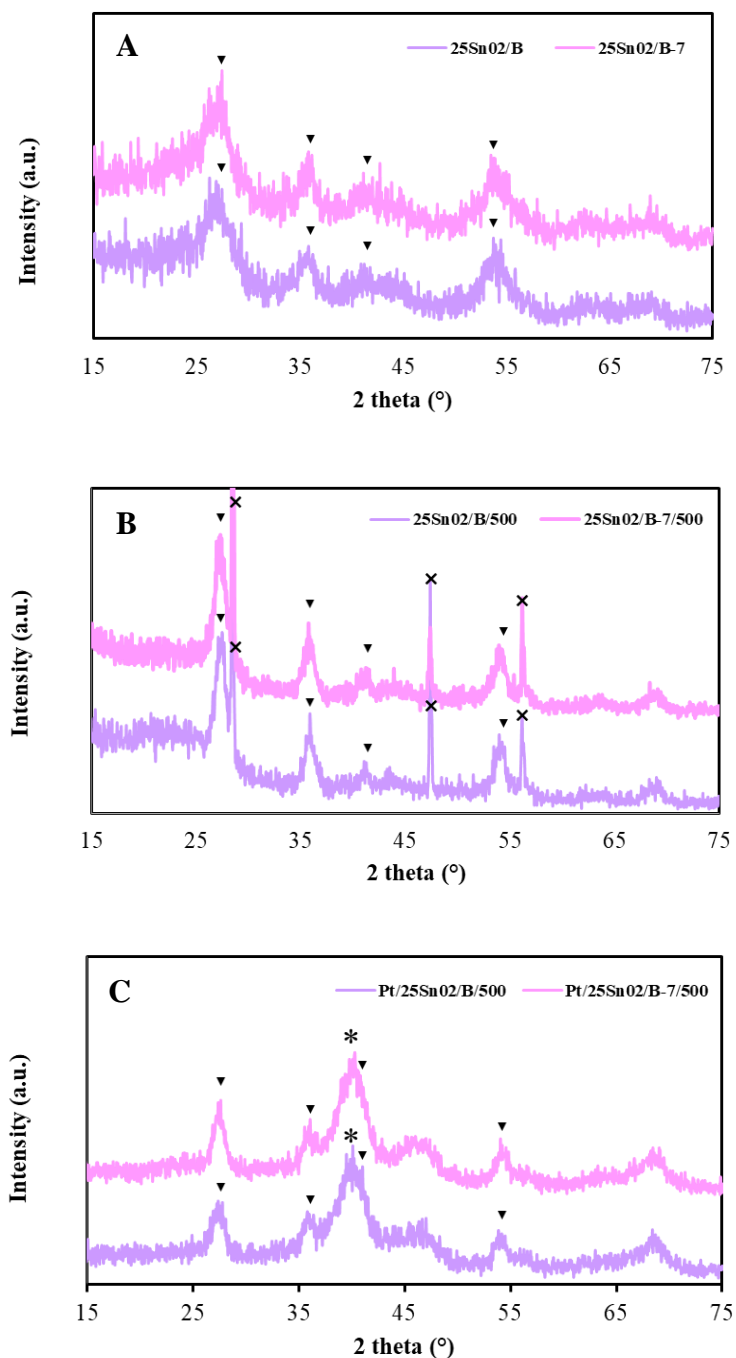


**Figure 34.** XRD patterns of 25 wt.%  $\text{Ti}_{0.8}\text{Sn}_{0.2}\text{O}_2$  – 75 wt.% C composite materials before (A) and after (B) HTT as well as after Pt loading (C): 25Sn02/B/500 (violet), 25Sn02/B-7/500 (pink). ▼- Rutile, \*- Pt, ×- internal standard (Si).

### 5.3.2. Nitrogen physisorption measurements

Table 14 summarizes the specific surface area and pore volume values of the composites prepared by route *B*. The data are rather similar to those obtained by route *A*. As can be seen from data in Table 14, in the case of using the same carbonaceous material (e.g., Black Pearls 2000) the specific surface

area (SSA) of  $\text{Ti}_{(1-x)}\text{Sn}_x\text{O}_2\text{-C}$  composites mainly depends on the ratio of mixed oxide and carbon. As the content of carbonaceous material in composites increases, the SSA also increases. It has to be mentioned that the SSA of the parent BP carbon is  $1635 \text{ m}^2/\text{g}$  [164].

**Table 14.** Results of nitrogen adsorption measurements

| Sample ID      | Ti/Sn | Surface area<br>( $\text{m}^2/\text{g}$ ) | Total pore volume<br>( $\text{cm}^3/\text{g}$ ) |
|----------------|-------|---|---|
| 75Sn01/B/500   | 90/10 | 377.6                                     | 0.78  |
| 75Sn02/B/500   | 80/20 | 390.4                                     | 0.67  |
| 75Sn03/B/500   | 70/30 | 424.3                                     | 0.68  |
| 25Sn02/B/500   | 80/20 | 1185.0                                    | 1.77  |
| 25Sn02/B-7/500 | 80/20 | 1168.2                                    | 1.68  |

### 5.3.3. Transmission electron microscopy (TEM) analysis

TEM images of Pt electrocatalysts supported on 75 wt.%  $\text{Ti}_{(1-x)}\text{Sn}_x\text{O}_2$  – 25 wt.% C composites with three different Sn content prepared by route **B** are presented in Figure 35. The microstructure of the supports was rather similar; no effect of the different Ti/Sn ratios was obvious. In contrast with the composites prepared by route **A**, the supports have a more homogeneous/uniform mixed oxide distribution. In particular, the nanorod-like oxide particles or the flower-like big  $\text{TiSnO}_x$  agglomerates, characteristic for the composite materials with high mixed oxide content (75 wt.%), were not observed. Instead, faceted oxide particles in the 10-15 nm size range as well as weakly crystallized and/or graphitized C-rich regions were evidenced. The supports were covered by 2-3 nm metallic Pt particles as confirmed by electron diffraction. There was no correlation between the sizes of either the Pt or the oxide particles and the nominal tin content of the supports.

Regarding the TEM image of the composite materials with high carbon content (75 wt.%), the even smaller mixed oxide nanoparticles with size lower than 10 nm was observed quite rarely (Figure 36). Taking into account the spatial distribution of oxide crystallites in these two samples, we can assume a fairly homogeneous oxide coating. The catalysts contained 2-3 nm metallic Pt particles uniformly dispersed over the composite surface.

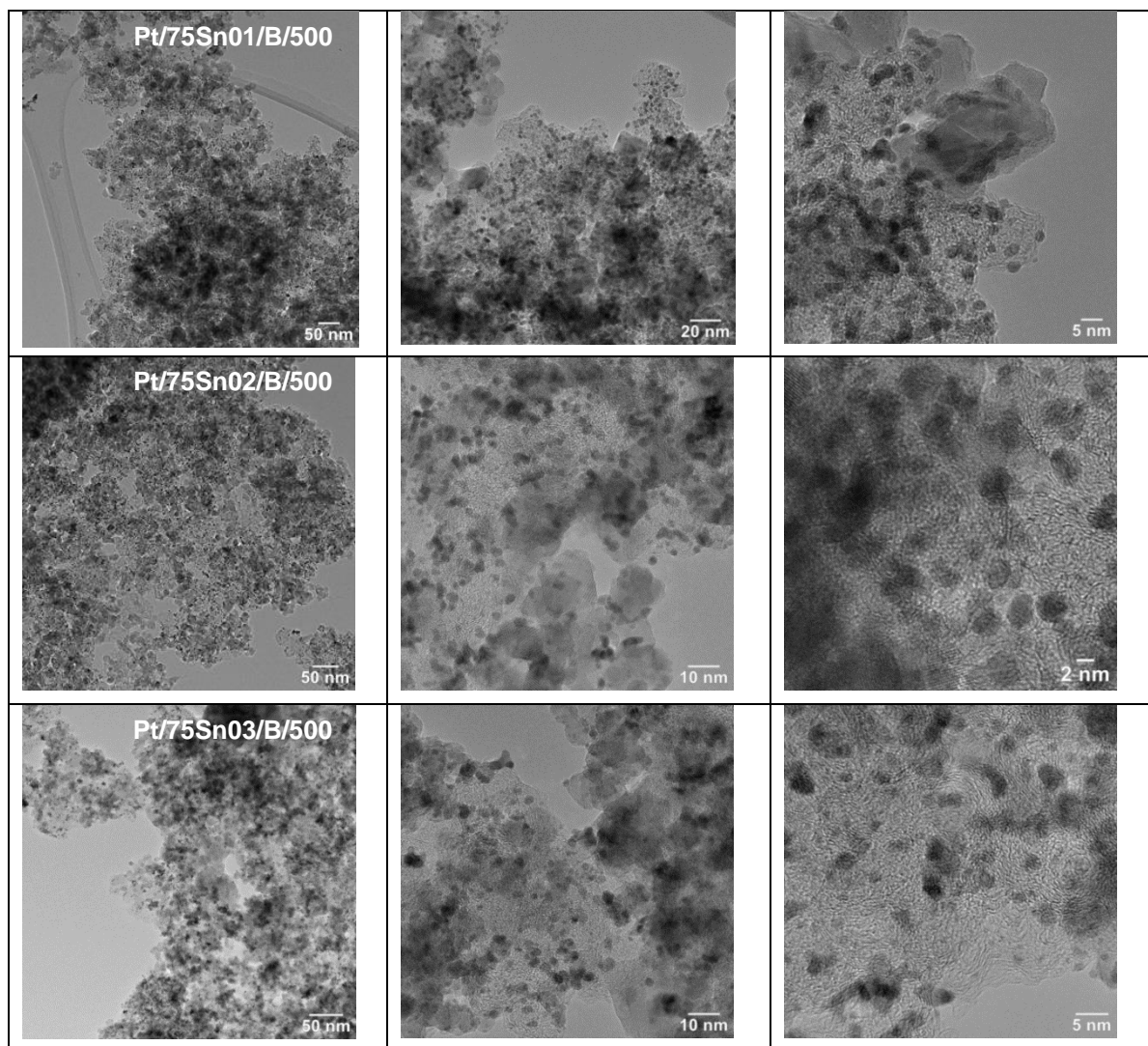


**Figure 35.** TEM images of the 20 wt. Pt/75 wt.%  $\text{Ti}_{(1-x)}\text{Sn}_x\text{O}_2$ -25 wt.% C electrocatalysts: Pt/75Sn01/B/500 (at the top), Pt/75Sn02/B/500 (in the middle) and Pt/75Sn03/B/500 (at the bottom).

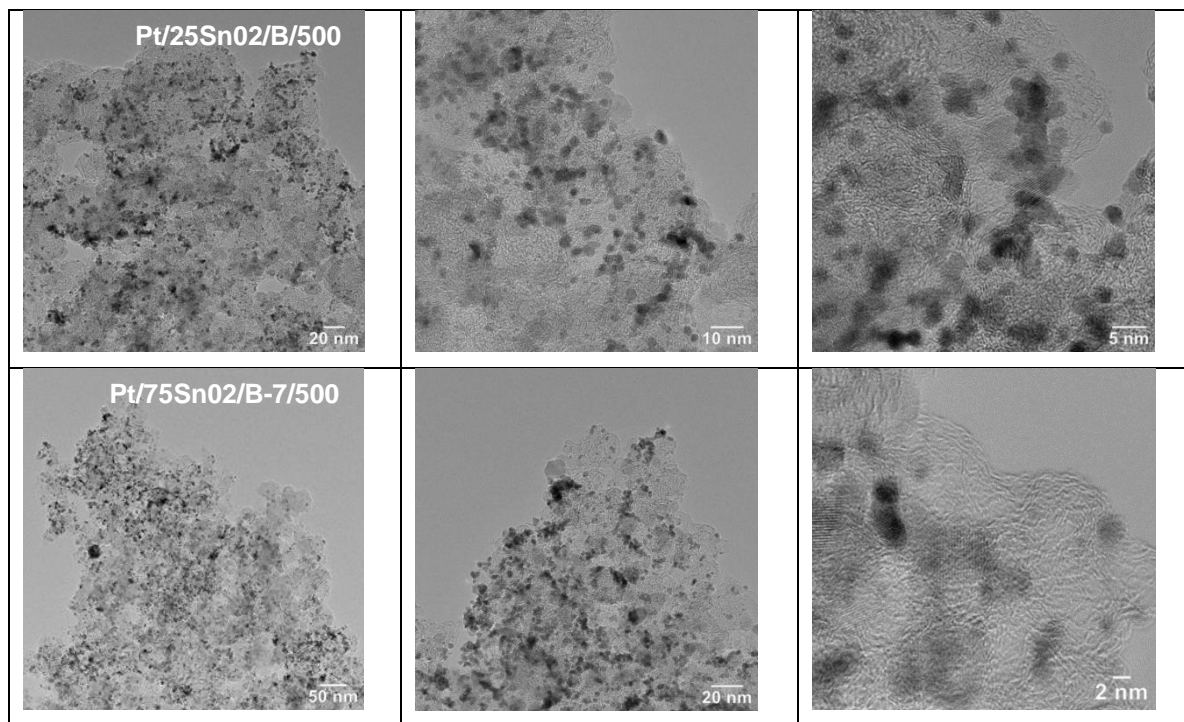


**Figure 36.** TEM images of the 20 wt. Pt/25 wt.%  $\text{Ti}_{0.8}\text{Sn}_{0.2}\text{O}_2$ -75 wt.% C electrocatalysts: Pt/25Sn02/B/500 (at the top) and Pt/25Sn02/B-7/500 (at the bottom).

#### 5.3.4. SEM/EDX measurements

SEM/EDX technique was used for the investigation of the morphology of composite supported Pt electrocatalysts (Figures 37-39). The results of the characterization of selected areas of  $\text{Ti}_{(1-x)}\text{Sn}_x\text{O}_2$ -C composite supported Pt catalysts by EDX was demonstrated in Table 15. Due to the fact that our preliminary experiments showed that Pt content is close to nominal only in mixed oxide-rich regions and carbon-rich regions contain less Pt, in this study we focused on oxide-rich regions. As shown in Table 15 the nominal and measured values of the content of Pt, Ti and Sn were in good agreement.

**Table 15.** Characterization of selected areas of  $\text{Ti}_{(1-x)}\text{Sn}_x\text{O}_2$ -C composite supported Pt catalysts by EDX; the nominal composition is given for comparison.

| Sample ID      | Ti (wt.%) |      | Sn (wt.%) |      | O (wt.%) |      | C (wt.%) |      | Pt (wt.%) |      |
|----------------|-----------|------|-----------|------|----------|------|----------|------|-----------|------|
|                | Nom.      | EDX  | Nom.      | EDX  | Nom.     | EDX  | Nom.     | EDX  | Nom.      | EDX  |
| 75Sn01/B/500   | 29.7      | 32.7 | 8.2       | 7.6  | 22.1     | 29.8 | 20.0     | 9.2  | 20.0      | 17.3 |
| 75Sn02/B/500   | 24.4      | 31.4 | 15.1      | 15.3 | 20.4     | 24.0 | 20.0     | 7.4  | 20.0      | 21.0 |
| 75Sn03/B/500   | 19.9      | 25.6 | 21.1      | 17.6 | 19.0     | 25.0 | 20.0     | 8.7  | 20.0      | 22.2 |
| 25Sn02/B/500   | 8.1       | 8.6  | 5.1       | 4.2  | 6.8      | 21.4 | 60.0     | 43.8 | 20.0      | 18.4 |
| 25Sn02/B-7/500 | 8.1       | 9.5  | 5.1       | 4.3  | 6.8      | 20.1 | 60.0     | 42.6 | 20.0      | 20.6 |

„Nom.“: nominal composition

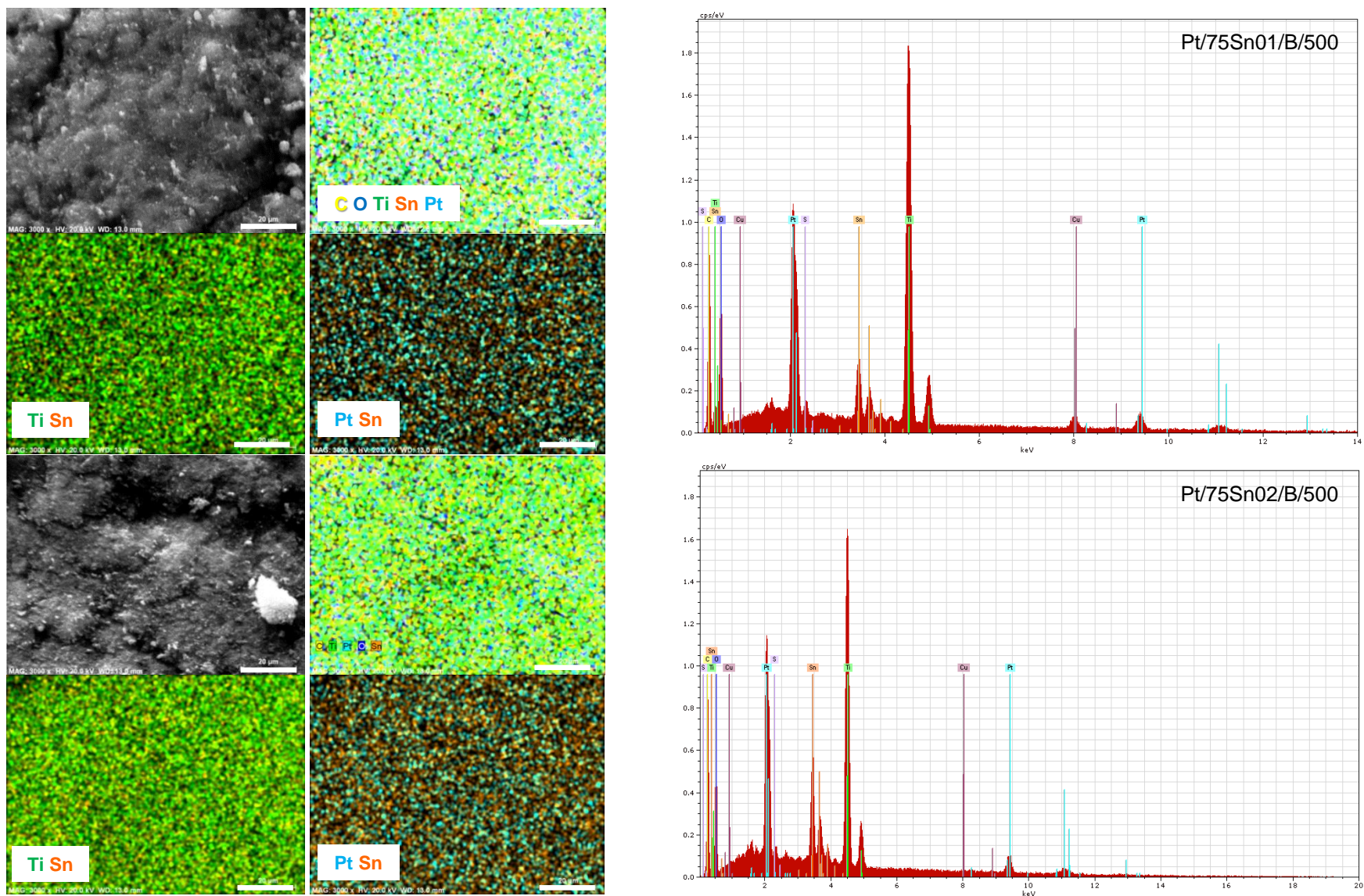


**Figure 37.** SEM micrographs and EDX elemental analysis of the Pt/75Sn01/B/500 (at the top) and the Pt/75Sn02/B/500 (at the bottom); scale bar: 20  $\mu$ m

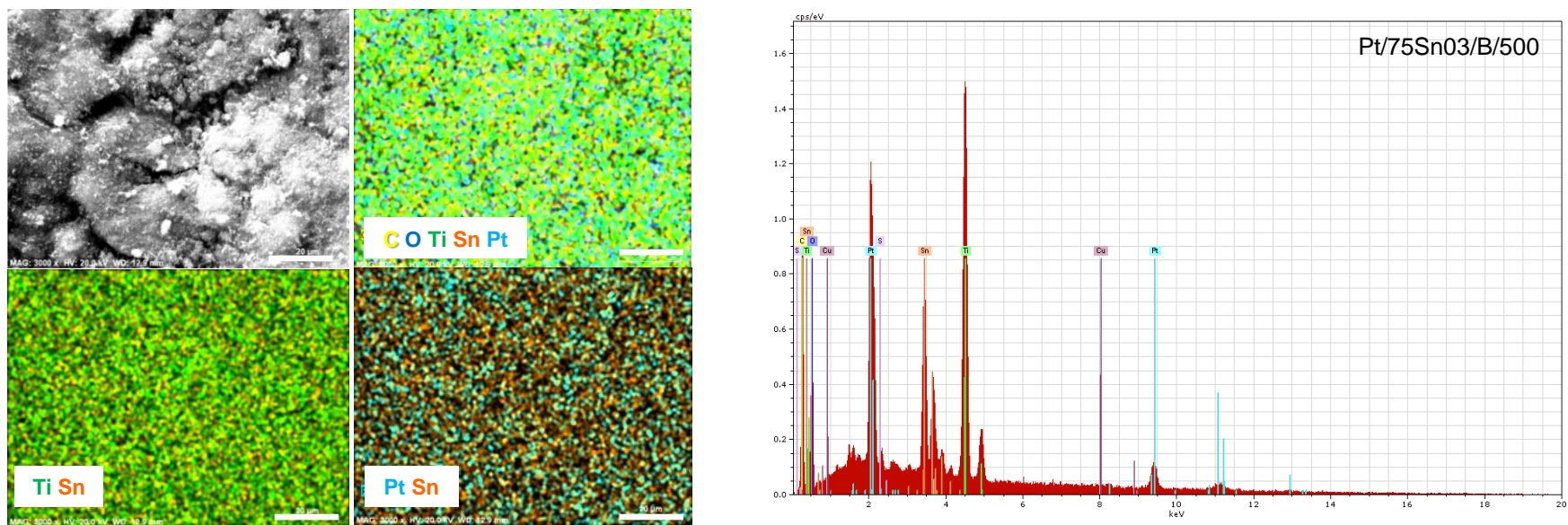


**Figure 38.** SEM micrographs and EDX elemental analysis of the Pt/75Sn03/B/500 catalyst; scale bar: 20  $\mu$ m

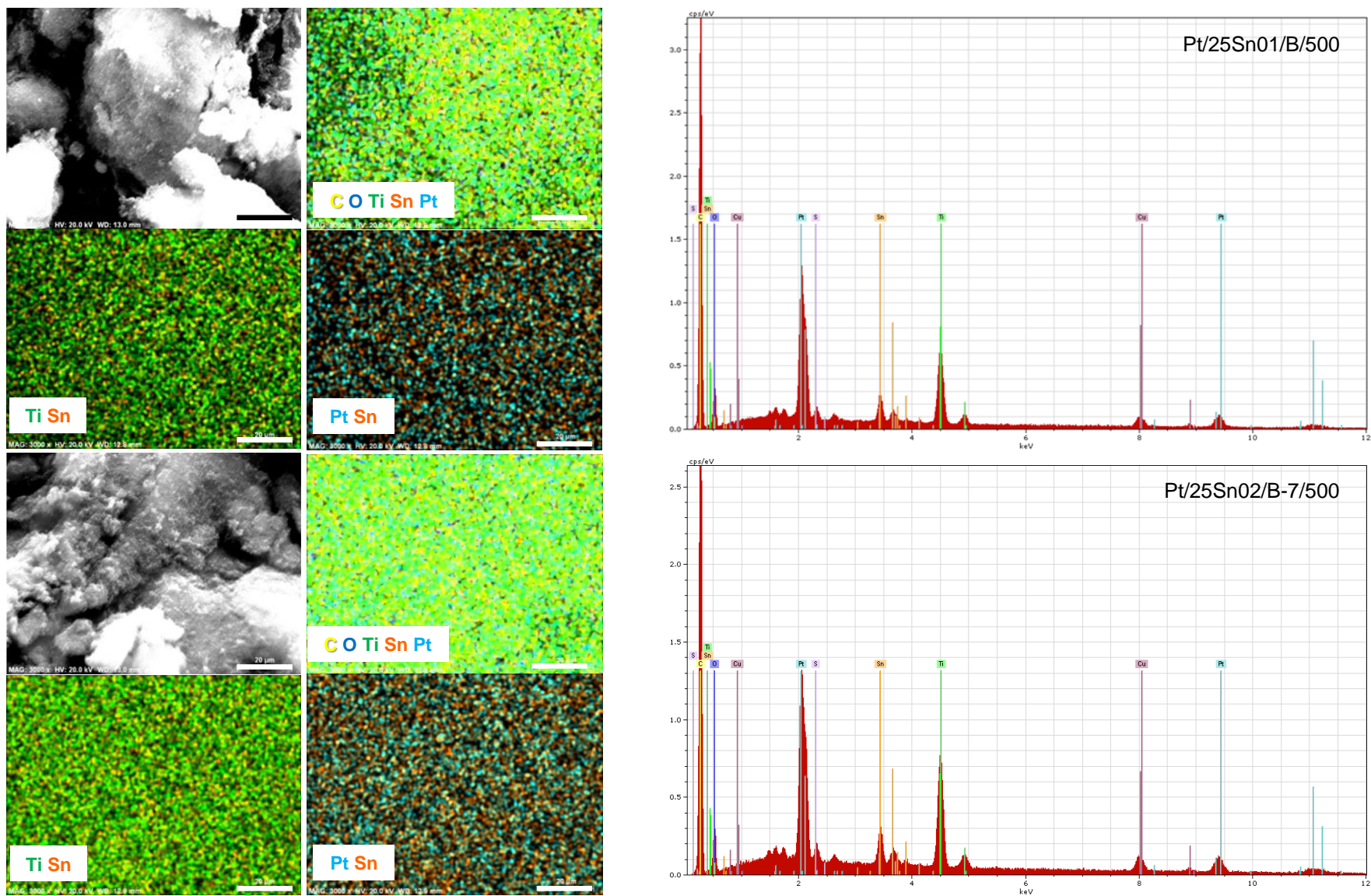


**Figure 39.** SEM micrographs and EDX elemental analysis of the Pt/25Sn02/B/500 (at the top) and the Pt/25Sn02/B-7/500 (at the bottom); scale bar: 20  $\mu$ m

**Table 16.** Composition of Sn-containing composite supported 20 wt.% Pt/Ti<sub>(1-x)</sub>Sn<sub>x</sub>O<sub>2</sub>-C electrocatalysts from EDX measurements (in comparison with nominal values).

| Sample ID         | Ti/Sn (at/at) |           | TiSnO <sub>x</sub> /C (wt.%/wt.%) |           | Pt (wt.%) |
|-------------------|---------------|-----------|-----------------------------------|-----------|-----------|
|                   | Nominal       | EDX       | Nominal                           | EDX       |           |
| Pt/75Sn01/B/500   | 90/10         | 91.4/8.6  | 75/25                             | 88.9/11.1 | 17.3      |
| Pt/75Sn02/B/500   | 80/20         | 83.6/16.4 | 75/25                             | 90.6/9.4  | 21.0      |
| Pt/75Sn03/B/500   | 70/30         | 78.0/22.0 | 75/25                             | 88.8/11.2 | 22.2      |
| Pt/25Sn02/B/500   | 80/20         | 83.5/16.5 | 25/75                             | 46.3/53.7 | 18.4      |
| Pt/25Sn02/B-7/500 | 80/20         | 83.5/16.5 | 25/75                             | 46.3/53.7 | 20.6      |

As shown in Table 16, the Ti/Sn ratios calculated from the EDX measurements are slightly higher than the nominal values. Similar results were obtained on the catalysts prepared by route **A** (see Table 10). As was mentioned above, a possible reason for the decrease in the Sn content may be the formation of volatile tin compounds during decomposition of tin (IV) chloride pentahydrate during the high temperature treatment. The obtained values of carbon content (see Table 16) are less than nominal, probably because in our studies we concentrated on regions rich in mixed oxide.

### 5.3.5. X-ray photoelectron spectroscopy (XPS) examination

XPS investigations were also performed on selected Ti<sub>0.8</sub>Sn<sub>0.2</sub>O<sub>2</sub>-C type supports and catalysts prepared by route **B**. Similarly to the case of the materials prepared by route **A**, no unexpected elements apart from Pt, Sn, Ti, O and C were observed. Exactly as in the former case, Pt was predominantly metallic, Ti was completely oxidized, and the carbon spectra corresponded to that of the Black Pearls 2000 material. However, clear surface composition differences demonstrated the effect of the preparation route on the microstructure of the support.

Table 17 contains the composition results from XPS obtained on supports and electrocatalysts synthesized by preparation route **B**.

**Table 17.** Surface composition data obtained on selected samples containing composites prepared by route **B**.

| Sample ID              | Nominal composition                                   | Nominal Ox/C <sup>a)</sup> | XPS Ox/C <sup>b)</sup> | XPS Ti/Sn | Metallic Sn fraction <sup>c)</sup> | XPS Pt/support ratio <sup>d)</sup> |
|------------------------|---|----------------------------|------------------------|-----------|------------------------------------|------------------------------------|
| <b>75Sn02/B/500</b>    | Ti <sub>0.8</sub> Sn <sub>0.2</sub> O <sub>2</sub> -C | 75/25                      | 73/27                  | 1.62:1    | <1%                                | --                                 |
| <b>Pt/75Sn02/B/500</b> | Ti <sub>0.8</sub> Sn <sub>0.2</sub> O <sub>2</sub> -C | 75/25                      | 82/18                  | 2.05:1    | <2%                                | 21/79                              |
| <b>Pt/25Sn02/B/500</b> | Ti <sub>0.8</sub> Sn <sub>0.2</sub> O <sub>2</sub> -C | 25/75                      | 24/76                  | 1.83:1    | 3%                                 | 21/79                              |

<sup>a)</sup> Ox/C: Ti<sub>(1-x)</sub>Sn<sub>x</sub>O<sub>2</sub>/C mass ratio (wt.%/wt.%)

<sup>b)</sup> calculated without the Pt content;

<sup>c)</sup> with respect to the total tin content;

<sup>d)</sup> Pt/support ratio: Pt/Ti<sub>(1-x)</sub>Sn<sub>x</sub>O<sub>2</sub>-C mass ratio (wt.%/wt.%)

In this case, very good agreement was experienced between the nominal and the apparent oxide/carbon ratio determined by XPS. The situation was similar concerning the Pt/support mass ratio in the studied electrocatalyst samples. In good agreement with the results demonstrated by TEM, this result suggests much better homogeneity of the samples on the length scale of the information depth of

XPS (10 nm). Thus, much better oxide dispersion and/or coverage of carbon with less predominance of the flower-like aggregates is confirmed also by XPS, along with homogeneous distribution of the Pt particles.

In comparison with the materials from support preparation route *A*, the surface tin excess in these samples was clearly lower, suggesting somewhat more homogeneous mixing of tin and titanium in the oxide phase. Nevertheless, the nominal 4:1 Ti/Sn ratio was still not approached. Although some change of the surface tin content upon Pt loading may have occurred, significant tin dissolution or re-deposition seems to be improbable.

The thermal stability of the 75SnO<sub>2</sub>/B/500 composite was investigated in a supporting experiment consisting of simulated high temperature treatment in Ar in the electron spectrometer between 500 °C and 700 °C. Up to 600 °C, practically no change occurred in the apparent oxide/carbon ratio, which can probably be explained by the stabilizing effect of the Ti-Sn mixing against oxide sintering during HTT. This behavior is in clear contrast with the composites prepared by route *A*, where oxide sintering was evident already after HTT at 300 °C-400 °C. Nevertheless, a slight but clear decrease of the oxide content of the 75SnO<sub>2</sub>/B/500 composite after annealing to 700 °C in Ar indicated that HTT above 600 °C may not be advisable.

Figure 40 compares the changes of the Sn 3d spectra of the 75SnO<sub>2</sub>/A and the 75SnO<sub>2</sub>/B composites during the simulated HTT series. The dominant chemical state in both cases was Sn<sup>4+</sup> with the Sn 3d<sub>5/2</sub> peak around 487.0 eV. However, once again the much better stability of the support prepared by route *B* is evident: while the carbothermal reduction resulting in metallic tin started around 400 °C and became quite significant after HTT at 500 °C in 75SnO<sub>2</sub>/A, the amount of metallic tin was undetectably small after 500 °C and remained marginal after 600 °C HTT in 75SnO<sub>2</sub>/B. Nevertheless, annealing of the latter composite above 600 °C resulted in strong reduction.

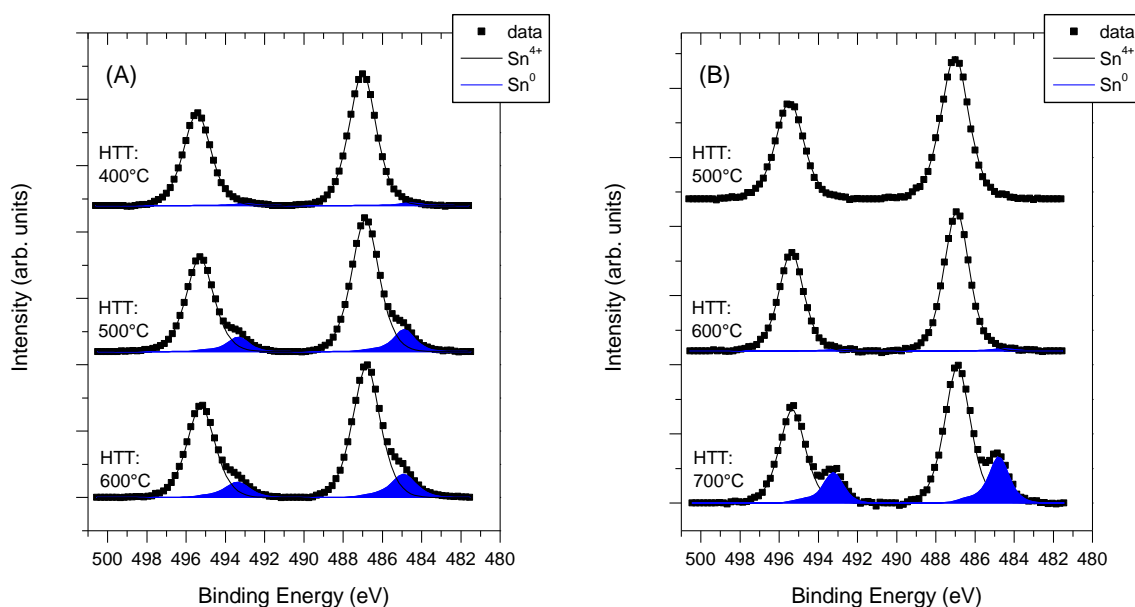


**Figure 40.** Sn 3d spectra of the 75SnO<sub>2</sub>/A (A) and the 75SnO<sub>2</sub>/B (B) composites during simulated HTT in 300 mbar Ar in the electron spectrometer. Please note the difference in the temperature range.

After Pt loading, a minimal amount of metallic tin may have appeared in the electrocatalyst supported on the 75SnO<sub>2</sub>/B/500 composite, while the presence of the metallic Sn component was somewhat more evident in the Pt/25SnO<sub>2</sub>/B/500 electrocatalyst. The role of direct Pt-Sn interactions (i.e. the very easy reducibility of tin in atomic closeness to Pt [173]) cannot be excluded in the formation of metallic tin in these systems.

#### 5.4. Route B - electrochemical characterization of the 20 wt.% Pt/Ti<sub>(1-x)</sub>Sn<sub>x</sub>O<sub>2</sub>-C electrocatalysts

The samples obtained by synthesis route **B** were characterized by electrochemical methods including cyclic voltammetry and CO<sub>ads</sub>-stripping voltammetry measurements combined with stability test involving 500 and 10,000 polarization cycles (see Table 18 and Figure 41-46).

**Table 18.** Electrochemical performance of the reference Pt/C and Pt/Ti<sub>(1-x)</sub>Sn<sub>x</sub>O<sub>2</sub>-C electrocatalysts prepared by route **B**.

| Sample ID         | E <sub>CO,onset</sub> , <sup>a)</sup><br>mV | E <sub>CO,max</sub> , <sup>b)</sup> mV | ECSA <sub>1</sub> , <sup>c)</sup><br>m <sup>2</sup> /g <sub>Pt</sub> | ΔECSA <sub>500</sub> ,<br>% <sup>d)</sup> | ΔECSA <sub>10,000</sub> ,<br>% <sup>d)</sup> |
|-------------------|---|--|--|---|--|
| Pt/75Sn01/B/500   | 245   | 785 ( <i>sh</i> : 675)                 | 58.5 ± 1.4   | 11.7                                      | 42.7   |
| Pt/75Sn02/B/500   | 245   | 775 ( <i>sh</i> : 675)                 | 59.3 ± 3.0   | 15.5                                      | 49.8   |
| Pt/75Sn03/B/500   | 245   | 775 ( <i>sh</i> : 675)                 | 54.6 ± 1.8   | 16.7                                      | n.d.   |
| Pt/25Sn02/B/500   | 245   | 775 ( <i>sh</i> : 435, 675)            | 68.7 ± 1.0   | 12.9                                      | 45.8   |
| Pt/25Sn02/B-7/500 | 245   | 775 ( <i>sh</i> : 435, 675)            | 78.2 ± 1.0   | 11.8                                      | n.d.   |
| Pt/C              | 625   | 795                                    | 87.2 ± 2.3   | 12.7 <sup>e)</sup>                        | 47.8   |

<sup>a)</sup> The onset potential for the CO electrooxidation;

<sup>b)</sup> The position of the main CO stripping peak measured on fresh catalysts;

<sup>c)</sup> The average ECSA value obtained on fresh catalysts in four parallel measurements;

<sup>d)</sup> ΔECSA<sub>500</sub> and ΔECSA<sub>10,000</sub> were calculated from the charges originated from the hydrogen desorption in the 1<sup>st</sup> and 500<sup>th</sup> or 10,000<sup>th</sup> cycles according to the Equation 10 (see Experimental part);

<sup>e)</sup> ΔECSA<sub>500</sub> value was calculated from the 10,000-cycle stability measurements;

*sh*= shoulder; n.d.= no data.

Influence of the order of adding tin precursor compound during the synthesis of composite materials along the route **A** and **B** on the electrochemical characteristics was demonstrated on Figure 41.

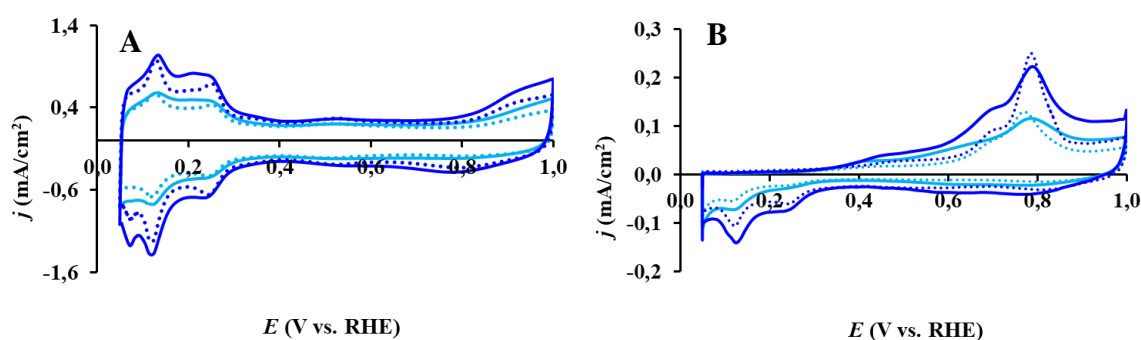


**Figure 41.** Influence of the preparation method on the electrochemical performance: comparison of the cyclic voltammograms (A) and CO<sub>ads</sub> stripping voltammograms (B) of the Pt/75Sn02/A/600 (light blue) and Pt/75Sn02/B/500 (dark blue) electrocatalysts obtained on fresh samples (solid lines) and after stability test (dotted lines) in 0.5 M H<sub>2</sub>SO<sub>4</sub>. Pt loading of the electrodes was 10 μg/cm<sup>2</sup>. Sweep rate: (A) 100 mV/s and (B) 10 mV/s, T= 25 °C.

As can be seen from Figure 41, mixing Sn and Ti precursors prior to the addition of carbon resulted in a marked increase in both the electrochemically active surface area of Pt and CO electrooxidation peaks. However, this did not affect the position of the maximum of the CO oxidation peaks in the voltammograms. It can be assumed that similar active centers are formed during the

preparation of composites by both methods, but the number of these centers in the composites obtained by synthesis route **B** is higher.

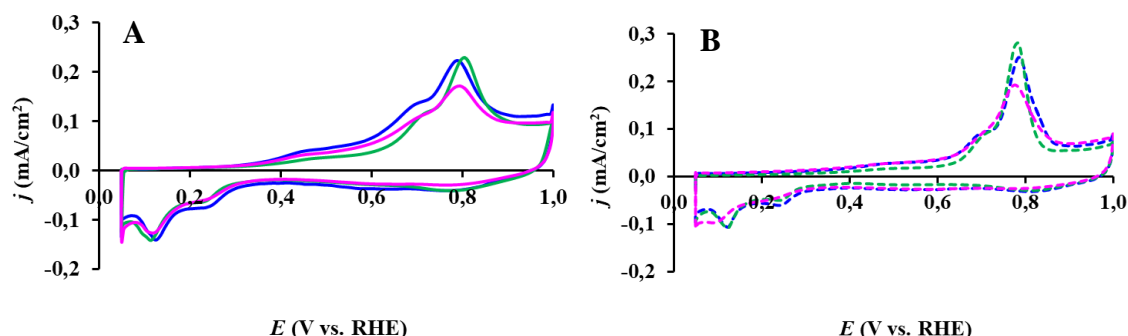


**Figure 42.** Influence of the Ti/Sn ratios of composite support materials on the electrochemical performance of the corresponding Pt catalysts with high mixed oxide content (75 wt.%).  $\text{CO}_{\text{ads}}$  stripping voltammograms of the Pt/75Sn01/B/500 (■), Pt/75Sn02/B/500 (■) and Pt/75Sn03/B/500 (■) electrocatalysts obtained before (A) and after the 500-cycle stability test (B). Recorded in 0.5 M  $\text{H}_2\text{SO}_4$  at 10 mV/s,  $T = 25^\circ\text{C}$ .

As shown in Figure 42 there is practically no difference in the behavior of electrocatalysts with various Ti/Sn ratios. Again, similar to the results obtained with the catalysts synthesized using route **A**, the  $\text{CO}_{\text{ads}}$  stripping voltammograms obtained on different catalysts were very similar; the observed difference is within the reproducibility of electrochemical measurements (see Figure 42). Perhaps, as shown in Figure 42.A and 42.B, only the catalyst with the highest tin content (Pt/75Sn03/B/500) has a lower activity.

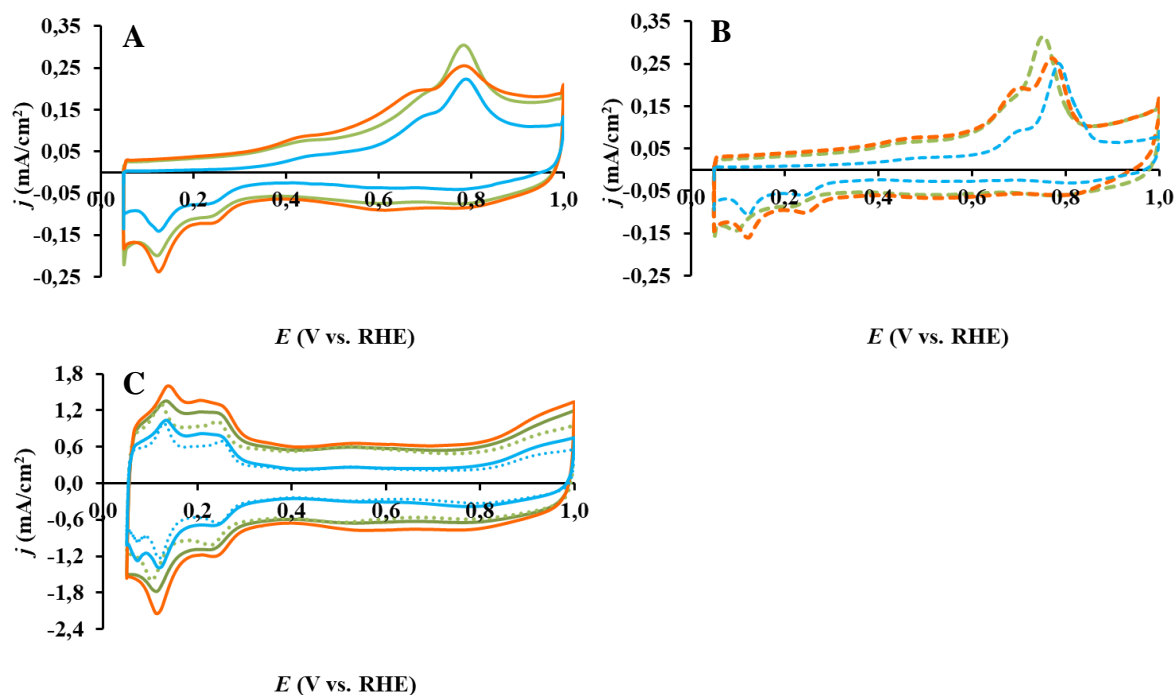


**Figure 43.** Influence of the duration of the aging step used during the synthesis composite support materials on the electrochemical performance of the Pt/25Sn02/B/500 (■) and Pt/25Sn02/B-7/500 (■) electrocatalysts with high carbon content (75 wt.%):  $\text{CO}_{\text{ads}}$  stripping voltammograms obtained before (A) and after the 500-cycle stability test (B); (C) comparison of the cyclic voltammograms obtained on fresh samples (solid lines) and after stability test (dotted lines). Results obtained on the

Pt/75SnO<sub>2</sub>/B/500 (■) catalyst are given for comparison. Recorded in 0.5 M H<sub>2</sub>SO<sub>4</sub> at 10 mV/s (A, B) and 100 mV/s (C), T= 25 °C.

Electrochemical characterization of two catalysts with high carbon content (75 wt.%) was presented in Figure 43; for comparison results obtained on the Pt/75SnO<sub>2</sub>/B/500 with 25 wt.% of carbon were also included. As can be seen from Figure 43.C, the increase of the carbon content in composite materials leads to the following increase of the ECSA of Pt in related catalysts.

As shown in Figure 43.A and 43.B, the position of the maximum of the CO oxidation peaks on the voltammograms does not depend on either the duration of the aging step or the carbon content in the composite supported catalyst. Based on these results, it can be assumed that an increase of the content of carbon in the composite materials prepared by route **B** leads to a further increase of the number of catalytically active sites responsible for enhanced CO tolerance.

In recent study of the research group it has been demonstrated [143] that the position of the main CO<sub>ads</sub> stripping peak on 20 wt.% Pt/Ti<sub>0.8</sub>Mo<sub>0.2</sub>O<sub>2</sub>-C catalysts with 75 wt.% mixed oxide in composite (705 mV) was shifted towards less positive potentials by 70 mV with respect to the main peak observed on the catalysts with 75 wt.% carbon (775 mV). However, in contrast to systems containing Mo, the results obtained on Sn-containing composite supported catalysts show that the position of the peaks in the CO<sub>ads</sub> stripping voltammograms does not depend on the oxide/carbon ratio.

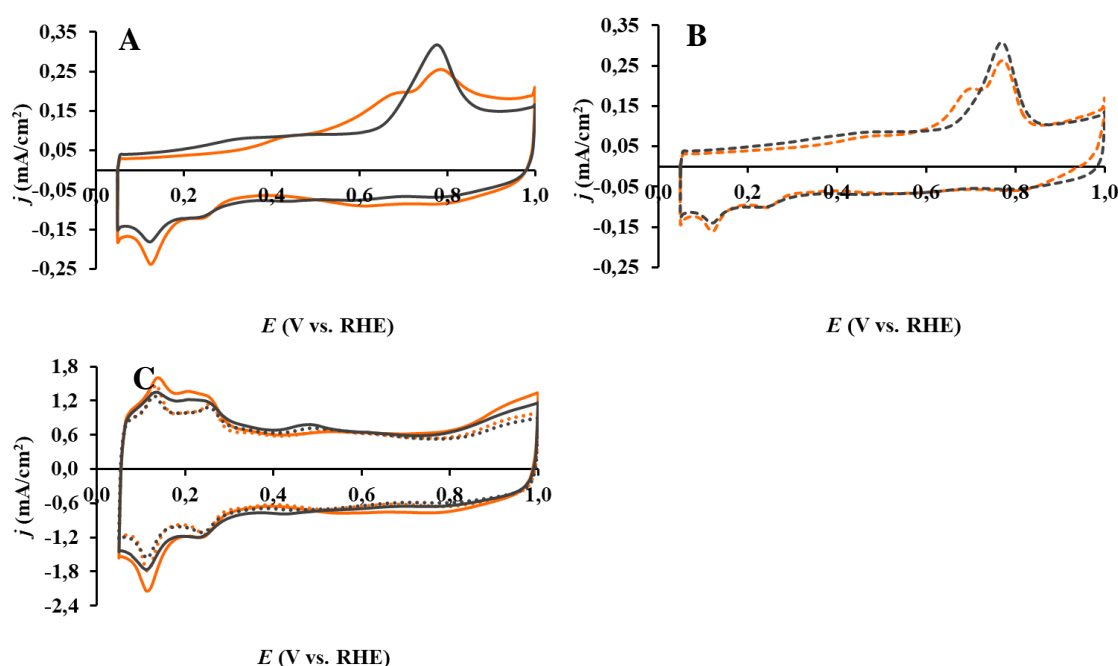


**Figure 44.** Comparison of electrocatalytic performance of 20 wt.% Pt/Ti<sub>0.8</sub>Mo<sub>0.2</sub>O<sub>2</sub>-C (M: Mo (■) and Sn (■)) electrocatalysts with high carbon content (75 wt.%): CO<sub>ads</sub> stripping voltammograms obtained before (A) and after the 500-cycle stability test (B); (C) comparison of the cyclic voltammograms obtained on fresh samples (solid lines) and after stability test (dotted lines). Recorded in 0.5 M H<sub>2</sub>SO<sub>4</sub> at 10 mV/s (A, B) and 100 mV/s (C), T= 25 °C.

Comparison of the electrocatalytic characteristics of molybdenum- and tin-containing 20 wt.% Pt/Ti<sub>0.8</sub>Mo<sub>0.2</sub>O<sub>2</sub>-C electrocatalysts with a high carbon content (75 wt.%) was presented in Figure 44. This comparison shows that Sn-containing electrocatalysts can also be promising CO-tolerant anode catalysts for potential use in PEM fuel cells.

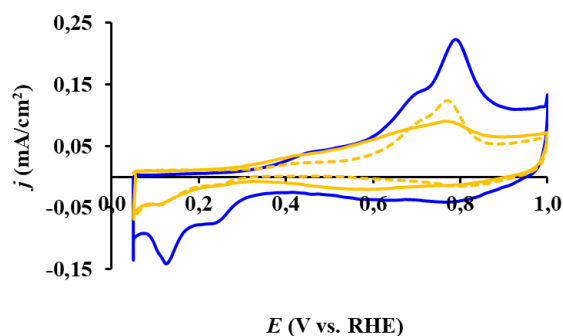


**Figure 45.** Comparison of the electrocatalytic performance of 75Sn02/B/500 composite supported Pt (blue) and alloy-type Sn-Pt/C catalysts reduced at 250 °C (dashed yellow line) and 350 °C (solid yellow line): CO<sub>ads</sub> stripping voltammograms obtained in 0.5 M H<sub>2</sub>SO<sub>4</sub> at 10 mV/s, T= 25 °C.

The presence of a small amount of the metallic tin in Pt catalysts prepared by route **B** was detected by XPS measurements. Comparison of the electrocatalytic performance of 75Sn02/B/500 composite supported Pt and alloy-type Sn-Pt/C catalysts is shown in Figure 45. Detailed information on the synthesis and characterization of alloy-type Sn-Pt/C electrocatalysts with a desired Pt/Sn ratio of 3 prepared using commercial 20 wt.% Pt/C catalyst by Controlled Surface Reactions was described in previous study of research group [173]. The similarity of the shape of the CO<sub>ads</sub> stripping voltammograms gives grounds to assume that the studied composite supported catalysts contain metallic tin in the close vicinity of Pt.

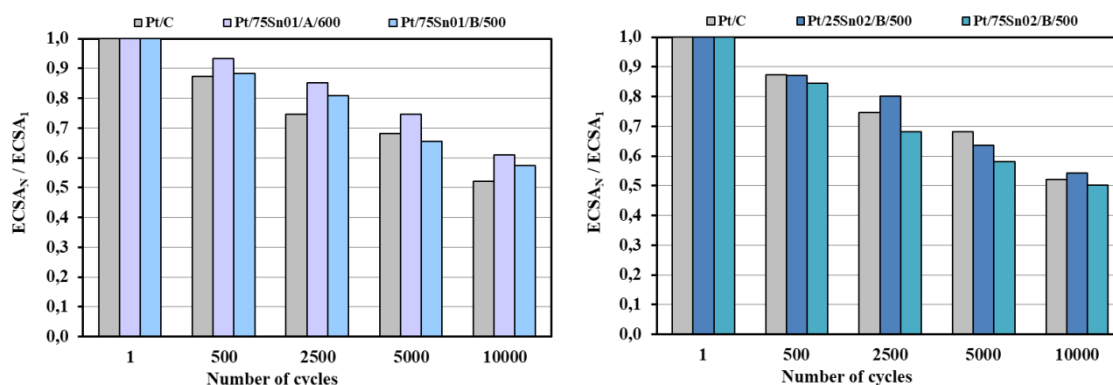


**Figure 46.** ECSA change during 10,000 CV cycles: comparison of the ECSA measured after N cycles normalized to ECSA measured in the 1<sup>st</sup> cycle ( $ECSA_N/ECSA_1$ ) as a function of the number of cycles (N).

As shown in Figure 46, in long-term stability tests over 10,000 cycles, Sn-containing composite supported Pt electrocatalysts showed very similar stability to the reference Pt/C. Since these experiments are very time consuming, not all of the obtained samples were measured; in addition, in order to draw conclusions, the reproducibility of these measurements will be verified.

### 5.5. *Electrochemical performance of the 20 wt.% Pt/Ti<sub>(1-x)</sub>Sn<sub>x</sub>O<sub>2</sub>-C electrocatalysts in the HOR and the ORR*

In order to clarify the possibility of using the Sn-containing Pt/Ti<sub>(1-x)</sub>Sn<sub>x</sub>O<sub>2</sub>-C catalysts (x: 0.1-0.3) as anode or cathode in PEM fuel cells, their electrocatalytic characteristics were investigated.

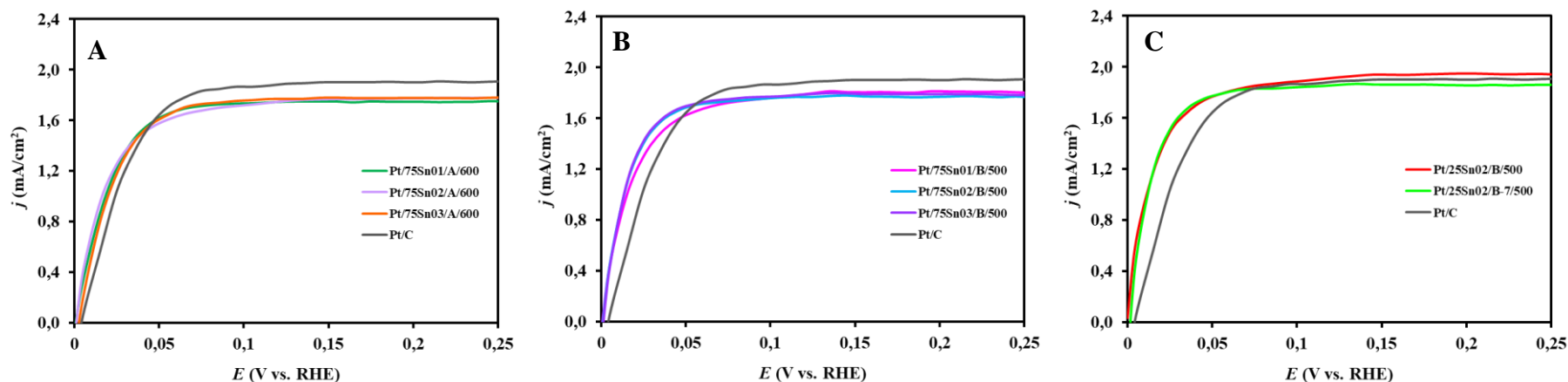


**Figure 47.** Electrochemical performance of the reference Pt/C and Sn-containing composite supported Pt catalysts by RDE measurements at 900 rpm in HOR. (A) and (B): effect of the Ti/Sn ratios in catalysts with 75 wt.% oxide content prepared by routes *A* and *B*; (C) the effect of the duration of the aging step on the performance of catalysts with 25 wt.% oxide content. HOR curves obtained in a  $\text{H}_2$ -saturated 0.5 M  $\text{H}_2\text{SO}_4$  at  $10 \text{ mV}\cdot\text{s}^{-1}$ .

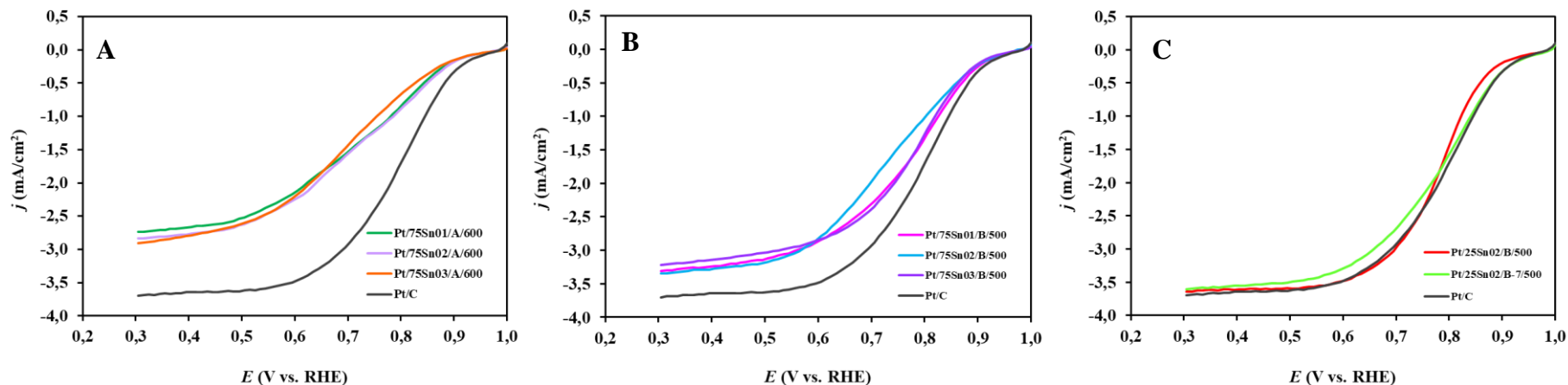


**Figure 48.** Electrochemical performance of the reference Pt/C and Sn-containing composite supported Pt catalysts by RDE measurements at 900 rpm in ORR. (A) and (B): effect of the Ti/Sn ratios in catalysts with 75 wt.% oxide content prepared by routes *A* and *B*; (C) the effect of the duration of the aging step on the performance of catalysts with 25 wt.% oxide content. ORR curves obtained in a  $\text{O}_2$ -saturated 0.5 M  $\text{H}_2\text{SO}_4$  at  $10 \text{ mV}\cdot\text{s}^{-1}$ .

The influence of the preparation method used in the synthesis of composite materials (**A** or **B**) on the performance in the HOR and the ORR was compared in Figures 47 and 48. Moreover, the effect of the duration of the aging step (4 or 7 days) used during composite preparation with a low mixed oxide content (25 wt.%) by route **B** on the electrochemical performance of catalysts was demonstrated in Figures 47.C and 48.C. For comparison, the behavior of a commercial Pt/C catalyst in both reactions was also shown under similar conditions.

Figure 47 shows HOR voltammograms (anodic scans) recorded via the RDE technique in H<sub>2</sub>-saturated 0.5 M H<sub>2</sub>SO<sub>4</sub> at  $\omega = 900$  rpm on the Pt/C and eight Sn-containing electrocatalysts. The currents were normalized to the geometric area of the glassy carbon electrode. As might be expected based on the results of cyclic voltammetry and CO<sub>ads</sub>-stripping voltammetry measurements the electrochemical performance of the Pt/Ti<sub>(1-x)</sub>Sn<sub>x</sub>O<sub>2</sub>-C catalysts prepared by the same preparation method was very similar (see Figures 47.A and 47.B), while the reference Pt/C catalyst shows a slightly higher HOR limiting current compared to the catalysts with high mixed oxide content. The reason for the somewhat lower diffusion limiting current density in composite supported Pt catalysts may be the slow diffusion of hydrogen through the oxide layer covering the Pt nanoparticles.

In accordance with this, as shown in Figure 47.C, the difference in diffusion limiting current density between reference Pt/C and composite supported Pt catalysts with high carbon content (75 wt.%) disappears. In addition, as seen in Fig. 47.C, on the Pt/25Sn02/B/500 catalyst the current increases more sharply compared to Pt/C, showing a higher activity.

Electrochemical performance of three Sn-containing composite supported Pt catalysts with Ti/Sn= 80/20 ratio was compared in Figure 49. As shown in Figure 49, a sharp increase in current is characteristic of all three Sn-containing platinum catalysts.

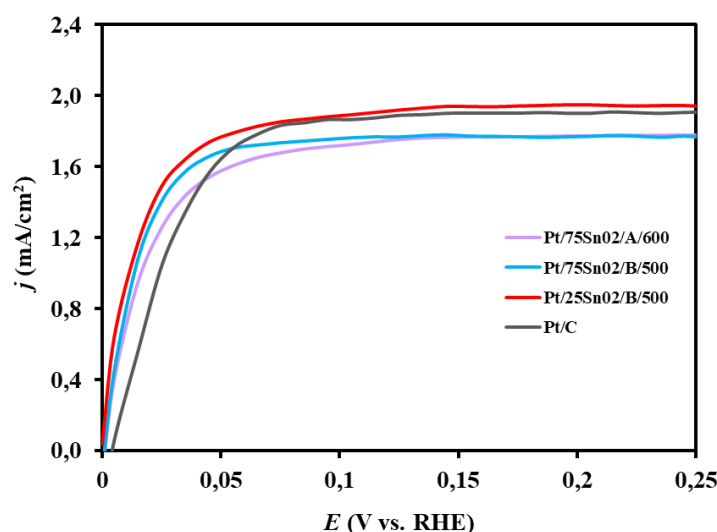


**Figure 49.** Electrochemical characterization of the reference Pt/C (■) and Sn-containing composite supported Pt catalysts with Ti/Sn= 80/20 ratio by RDE measurements at 900 rpm in HOR: Pt/75Sn02/A/600 (■), Pt/75Sn02/B/500 (■) and Pt/25Sn02/B/500 (■). HOR curves obtained in a H<sub>2</sub>-saturated 0.5 M H<sub>2</sub>SO<sub>4</sub> at 10 mV·s<sup>-1</sup>, T= 25 °C.

Similar trends are observed in the behavior of the studied catalysts in the ORR. As shown in Figure 48.A and 48.B, current density of the ORR in the mixed kinetic-diffusion controlled region on the fresh reference Pt/C catalyst was higher compared to the composite supported Pt catalysts with 75 wt.% mixed oxide and identical diffusion limited currents were reached on oxide-containing

catalysts prepared by the same synthesis route. As shown in Figure 48.C, the difference between the reference Pt/C and two catalysts with 75 wt.% carbon almost disappears.

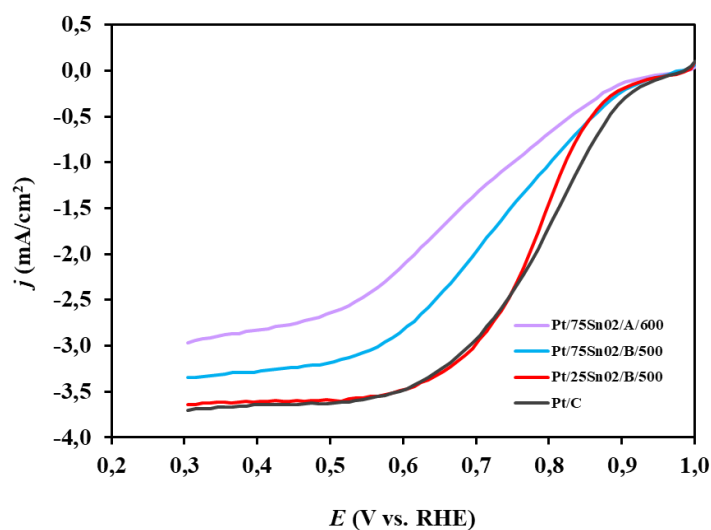


**Figure 50.** Electrochemical characterization of the reference Pt/C (■) and Sn-containing composite supported Pt catalysts with Ti/Sn= 80/20 ratio by RDE measurements at 900 rpm in ORR: Pt/75Sn02/A/600 (■), Pt/75Sn02/B/500 (■) and Pt/25Sn02/B/500 (■). ORR curves obtained in a O<sub>2</sub>-saturated 0.5 M H<sub>2</sub>SO<sub>4</sub> at 10 mV·s<sup>-1</sup>, T= 25 °C.

Figure 50 compares the electrochemical performance of Pt/Ti<sub>0.8</sub>Sn<sub>0.2</sub>O<sub>2</sub>-C catalysts prepared by route **A** and **B**, as well as catalysts having different Ti<sub>0.8</sub>Sn<sub>0.2</sub>O<sub>2</sub>/C ratios. According to the literature smaller limiting current density observed on oxide-containing can be originated from slower diffusion of oxygen through the oxide layer covering the Pt nanoparticles [174,175].

## 6. Summary

For the preparation of tin-containing composites, the technique previously developed by the research group for Mo-containing composite materials was adapted (route **A**). XRD, nitrogen adsorption measurements, TEM, SEM/EDX, XPS and Raman spectroscopy were used to characterize the bulk and surface microstructure of the composites and their Pt-loaded counterparts. The change in the TiO<sub>2</sub> lattice parameters measured by XRD, after high-temperature treatment (HTT) at 600 °C, confirmed the incorporation of tin into the rutile unit cell. The degree of Sn incorporation was in good accordance with the amount of tin precursor (for Ti<sub>(1-x)</sub>Sn<sub>x</sub>O<sub>2</sub>-C with x= 0.1, 0.2 and 0.3, the concentration of tin cations substituting titanium ones, i.e. Sn<sub>subst</sub>, was 7, 14 and 23%, respectively). TEM investigations indicated the coexistence of large mixed oxide nanorods and their agglomerates with much better dispersed oxide nanoparticles. XPS confirmed that the vast majority of tin was in the +4 oxidation state, although the composite surface shows significant tin enrichment. Presence of metallic Sn in small (1-2%) quantity was revealed in all samples by both XRD and XPS. XPS experiments pointed out that reduction of tin to the metallic state started around 400 °C in Ar atmosphere, which was explained by a carbothermal reduction process. Electrochemical investigations revealed unusually low electrochemically active Pt surface area in the catalysts (~30 m<sup>2</sup>/g<sub>Pt</sub>). Thus, the composites and electrocatalysts obtained in the preparation route **A** had the following drawbacks: (i) the formation of a small amount of metallic Sn phase (ii) certain inhomogeneity of the composite materials (the coexistence of TiSnO<sub>x</sub> agglomerated in flower-like clusters with more evenly dispersed oxide), and (iii) relatively low electrochemically active Pt surface area.

To avoid the formation of Sn<sup>0</sup> and to obtain better oxide homogeneity the synthesis of the composite was modified: the precursor of Sn was introduced immediately after the formation of the transparent Ti-sol, before the addition of the carbon and the aging step (route **B**).

XRD revealed that these composites contain pure rutile phase; the formation of Sn<sup>0</sup> or SnO<sub>2</sub> was not observed. XPS also suggested the lack of reduced tin species, while indicated better thermal stability of the composite. Based on TEM results, in contrast to the composites prepared by route **A**, the supports have a more homogeneous/uniform mixed oxide distribution. In particular, the nanorod-like oxide particles or the flower-like big TiSnO<sub>x</sub> agglomerates, characteristic for the composite materials with high mixed oxide content (75 wt.%), were not observed. Instead, faceted oxide particles in the 10-15 nm size range as well as weakly crystallized and/or graphitized C-rich regions were evidenced. The supports were decorated by 2-3 nm metallic Pt particles as confirmed by electron diffraction.

Results of SEM/EDX elemental analysis demonstrated that the Pt content measured by the EDX method in the regions of the catalyst enriched in mixed oxide is in good agreement with the nominal value. This finding indicated that areas rich in Pt and poor in Pt may also exist on the surface of the composite supports and Pt nanoparticles have high affinity to concentrate on the mixed oxide.

The samples obtained by synthesis routes **A** and **B** were characterized by electrochemical methods including cyclic voltammetry and CO<sub>ads</sub>-stripping voltammetry measurements combined with stability test involving 500 and 10,000 polarization cycles. Based on the electrochemical results, it can be concluded that the behavior of electrocatalysts strongly depends on the synthesis route used in the preparation of the composite support materials and does not depend on the Ti/Sn ratio. The use of method **B** for the preparation of catalysts leads to a noticeable increase in both the ECSA and the activity in CO electrooxidation. The similarity of the shape of voltammograms obtained on the catalysts prepared by both methods allows to assume that similar active species are formed, but in the composites obtained by synthesis route **B** the number of these species is higher. An increase of the carbon content in the composite materials prepared by route **B** leads to a further increase of the number of catalytically active species responsible for enhanced CO tolerance. Moreover, the similarity

of the shape of the  $\text{CO}_{\text{ads}}$  stripping voltammograms to that one obtained on alloy-type Sn-Pt/C catalysts gives grounds to assume that the studied composite supported catalysts contain tin in the close vicinity of Pt. Comparison of the electrocatalytic characteristics of Mo- and Sn-containing 20 wt.% Pt/Ti<sub>0.8</sub>M<sub>0.2</sub>O<sub>2</sub>-C electrocatalysts with a high carbon content (75 wt.%) revealed that Sn-containing electrocatalysts can also be promising CO-tolerant anode catalysts for potential use in PEM fuel cells.

## Acknowledgements

I would like to thank everyone who assisted with my research and dissertation completion.

I would like to thank my advisor, Dr. *András Tompos*, for his insightful guidance as I worked on my Master's thesis. As an internal supervisor, I am grateful to Dr. *Imre Miklós Szilágyi* for his helpful comments and ideas. My heartfelt appreciation goes to Dr. *Irina Borbáth*, my consultant, for her constructive direction and invaluable counsel in evaluating my results. Additionally, I would like to thank Dr. *Emilia Tálás* for all of her assistance and for providing me with insight into different study topics. Dr. *Zoltán Pászti* deserves special recognition for the XPS measurements and the analysis of the results. Dr. *Ágnes Szegedi* and *Wellischné Farkas Agnes* for the nitrogen physisorption measurements, as well as Dr. *Zoltán May* for the ICP-OES measurements are also acknowledged. Thanks to Dr. *István E. Sajó* for the help in the evaluation of XRD results. I am thankful to the Romanian colleagues from the National Institute of Materials Physics for their measurements in catalyst characterization and for their help in the evaluation of results (Dr. *Ștefan Neațu* - Raman spectroscopy, Dr. *Andrei Kuncser* – TEM/EDS, *Anca G. Mirea* – SEM/EDX).

Thank you very much to Dr. *Gábor Szijjártó* and *Ildikó Turi* for their technical aid in the preparation of the catalysts and for their assistance in my daily work.

I'd like to thank the other members of the Renewable Energy Research Group and all of my other coworkers for their contribution to my work as well as their kind and supportive attitude.

The financial supports by the following projects are greatly acknowledged:

This work was performed within the framework of the “Holistic design of fuel cell electrocatalysts for the least power applications” (CATALEAST) M-ERA.NET project. Project No. NNE 131270 has been implemented with the support provided from the National Research, Development and Innovation Fund of Hungary financed under the M-ERA.NET funding scheme.

Project no. NNE130004 has been implemented with the support provided from the National Research, Development and Innovation Fund of Hungary, financed under the TR-NN-17 funding scheme.

VEKOP-2.3.2-16-2017-00013. “The excellence of strategic R & D workshops, Material science excellence workshop: development of environmentally friendly processes for efficient use of renewable energy and raw materials and for controlled release of their energy content”.

Lastly, I am grateful to my family for their support, understanding, and the peaceful and secure environment I required to perform my duties.

## References

- [1] L. P. Bicelli, "Hydrogen: A Clean Energy Source," *Int. J. Hydrog. Energy*, vol. 11, no. 9, pp. 555–562, 1986.
- [2] The FreedomCAR and Fuel Partnership, "Hydrogen production: Overview of technology options," NY, U.S., 2009.
- [3] M. El-Shafie, S. Kambara, and Y. Hayakawa, "Hydrogen Production Technologies Overview," *J. Power Energy Eng.*, vol. 07, no. 01, pp. 107–154, 2019, doi: 10.4236/jpee.2019.71007.
- [4] B. G. Pollet, S. S. Kocha, and I. Staffell, "Current status of automotive fuel cells for sustainable transport," *Curr. Opin. Electrochem.*, vol. 16, pp. 90–95, 2019, doi: 10.1016/j.coelec.2019.04.021.
- [5] D. K. Madheswaran and A. Jayakumar, "Recent Advancements on Non-Platinum Based Catalyst Electrode Material for Polymer Electrolyte Membrane Fuel Cells: a Mini Techno-Economic Review," *Bull. Mater. Sci.*, vol. 44, 2021, doi: 10.1007/s12034-021-02572-6.
- [6] B. Vishwanathan and M. A. Scibioh, *Fuell Cells: Principles and Applications*. Himayatnagar, Hyderabad: Universities Press (india) Private Limited.
- [7] M. Ebrahimi, W. Kujawski, K. Fatyeyeva, and J. Kujawa, "A review on ionic liquids-based membranes for middle and high temperature polymer electrolyte membrane fuel cells (Pem fcs)," *Int. J. Mol. Sci.*, vol. 22, no. 11, 2021, doi: 10.3390/ijms22115430.
- [8] O. Celikbilek, "An experimental and numerical approach for tuning the cathode for high performance IT-SOFC," 2016.
- [9] A. Lanz, J. Heffel, and C. Messer, "Module 4: Fuel Cell Technology," in *Hydrogen Fuel Cell Engines and Related Technologies*, CA: College of the Desert, Energy Technology Training Center, 2001.
- [10] Y. Wang, K. S. Chen, J. Mishler, S. C. Cho, and X. C. Adroher, "A review of polymer electrolyte membrane fuel cells: Technology, applications, and needs on fundamental research," *Appl. Energy*, vol. 88, no. 4, pp. 981–1007, 2011, doi: 10.1016/j.apenergy.2010.09.030.
- [11] S. Mekhilef, R. Saidur, and A. Safari, "Comparative study of different fuel cell technologies," *Renew. Sustain. Energy Rev.*, vol. 16, no. 1, pp. 981–989, 2012, doi: 10.1016/j.rser.2011.09.020.
- [12] M. Gurz, E. Baltacioglu, Y. Hames, and K. Kaya, "The meeting of hydrogen and automotive: A review," *Int. J. Hydrogen Energy*, vol. 42, no. 36, pp. 23334–23346, 2017, doi: 10.1016/j.ijhydene.2017.02.124.
- [13] M. Ji and Z. Wei, "A Review of Water Management in Polymer Electrolyte Membrane Fuel Cells," *Energies*, vol. 2, pp. 1057–1106, 2009, doi: 10.3390/en20401057.
- [14] M. Wazikoe, A. O. Velev, and S. Shrinivasan, "Analysis of proton exchange membrane fuel

- cell performance with alternate membranes,” *Electrochim Acta*, vol. 40, p. 335, 1995.
- [15] X. Glipa and M. Hogarth, “Department of Trade and Industry,” 2014. <http://www.dti.gov.uk/renewable/pdf/f0200189..> (accessed Apr. 20, 2022).
- [16] T. Maiyalagan and S. Pasupathi, “Components for PEM Fuel cells : An Overview,” *Mater. Sci. Forum*, vol. 657, pp. 143–189, 2010, doi: 10.4028/www.scientific.net/MSF.657.143.
- [17] S. J. Peighambardoust, S. Rowshanzamir, and M. Amjadi, “Review of the proton exchange membranes for fuel cell applications,” *Int. J. Hydrogen Energy*, vol. 35, no. 17, pp. 9349–9384, 2010, doi: 10.1016/j.ijhydene.2010.05.017.
- [18] O. Z. Sharaf and M. F. Orhan, “An overview of fuel cell technology: Fundamentals and applications,” *Renew. Sustain. Energy Rev.*, vol. 32, pp. 810–853, 2014, doi: 10.1016/j.rser.2014.01.012.
- [19] V. Bagotsky, *Fuel Cells*. Moscow: John Wiley & Sons Inc, 2012.
- [20] Z. Zhang, J. Liu, J. Gu, L. Su, and L. Cheng, “An overview of metal oxide materials as electrocatalysts and supports for polymer electrolyte fuel cells,” *Energy Environ. Sci*, vol. 7, p. 2535, 2014, doi: 10.1039/C3EE43886D.
- [21] J. K. Nørskov, J. Rossmeisl, A. Logadottir, L. Lindqvist, J. R. Kitchin, T. Bligaard, H. Jónsson, “Origin of the overpotential for oxygen reduction at a fuel-cell cathode,” *J. Phys. Chem. B*, vol. 108, no. 46, pp. 17886–17892, 2004, doi: 10.1021/jp047349j.
- [22] Z. W. She, J. Kibsgaard, C. F. Dickens, I. Chorkendorff, J. K. Nørskov, and T. F. Jaramillo, “Combining theory and experiment in electrocatalysis: Insights into materials design,” *Science*, vol. 355, no. 6321, 2017, doi: 10.1126/science.aad4998.
- [23] M. Tang, S. Zhang, and S. Chen, “Pt Utilization In Proton Exchange Membrane Fuel Cells: Structure Impacting Factors and Mechanistic Insights,” *Chem. Soc. Rev.*, vol. 51, pp. 1529–1546, 2022, doi: 10.1039/d1cs00981h.
- [24] J. C. Meier, C. Galeano, I. Katsounaros, A. A. Topalov, A. Kostka, F. Schu, K. J. J Mayrhofer, “Degradation Mechanisms of Pt/C Fuel Cell Catalysts under Simulated Start – Stop Conditions,” *ACS Catal.*, vol. 2, no. 5, pp. 832–843, 2012.
- [25] P. C. Okonkwo, O. O. Ige, E. M. Barhoumi, P. C. Uzoma, W. Emori, A. Benamor, A. M. Abdullah, “Platinum degradation mechanisms in proton exchange membrane fuel cell (PEMFC) system: A review,” *Int. J. Hydrogen Energy*, vol. 46, no. 29, pp. 15850–15865, 2021, doi: 10.1016/j.ijhydene.2021.02.078.
- [26] P. J. Ferreira, G. J. la O, Y. Shao-Horn, D. Morgan, R. Makharia, S. Kocha, H. A. Gasteiger, “Instability of Pt/C Electrocatalysts in Proton Exchange Membrane Fuel Cells A Mechanistic Investigation,” *J. Electrochemical Soc.*, vol. 152, no. 11, pp. 2256–2271, 2005, doi: 10.1149/1.2050347.
- [27] C. A. Reiser, L. Bregoli, T. W. Patterson, J. S. Yi, J. D. Yang, M. L. Perry, T. D. Jarvi, “A Reverse-Current Decay Mechanism for Fuel Cells,” *Electrochemical Solid-state Lett.*, vol. 8,

- no. 6, pp. 273–276, 2005, doi: 10.1149/1.1896466.
- [28] M. F. Mathias, R. Makharia, H. A. Gasteiger, J. J. Conley, T. J. Fuller, C. J. Gittleman, S. S. Kocha, D. P. Miller, C. K. Mittelsteadt, T. Xie, S.G. Yan, P. T. Yu, “Two Fuel Cell Cars In Every Garage ?,” *Electrochem. Soc. Interface*, vol. 14, no. 3, pp. 24–35, 2005.
- [29] N. R. Elezović, L. M. Gajić-Krstajić, L. M. Vračar, and N. V. Krstajić, “Effect of chemisorbed CO on MoO<sub>x</sub>-Pt/C electrode on the kinetics of hydrogen oxidation reaction,” *Int. J. Hydrogen Energy*, vol. 35, no. 23, pp. 12878–12887, 2010, doi: 10.1016/j.ijhydene.2010.09.004.
- [30] E. I. Santiago, M. S. Batista, E. M. Assaf, and E. A. Ticianelli, “Mechanism of CO Tolerance on Molybdenum-Based Electrocatalysts for PEMFC,” *J. Electrochem. Soc.*, vol. 151, no. 7, pp. 944–949, 2004, doi: 10.1149/1.1753579.
- [31] Z. Yan, J. Xie, J. Jing, M. Zhang, W. Wei, and S. Yin, “MoO<sub>2</sub> nanocrystals down to 5 nm as Pt electrocatalyst promoter for stable oxygen reduction reaction,” *Int. J. Hydrogen Energy*, vol. 37, no. 21, pp. 15948–15955, 2012, doi: 10.1016/j.ijhydene.2012.08.033.
- [32] P. F. B. D. Martins and E. A. Ticianelli, “Electrocatalytic Activity and Stability of Platinum Nanoparticles Supported on Carbon – Molybdenum Oxides for the Oxygen Reduction Reaction,” *ChemElectroChem*, vol. 2, no. 9, pp. 1298–1306, 2015, doi: 10.1002/celc.201500196.
- [33] E. Antolini, “Catalysts for direct ethanol fuel cells,” *J. Power Sources*, vol. 170, no. 1, pp. 1–12, 2007, doi: 10.1016/j.jpowsour.2007.04.009.
- [34] L. G. S. Pereira, V. A. Paganin, and E. A. Ticianelli, “Investigation of the CO tolerance mechanism at several Pt-based bimetallic anode electrocatalysts in a PEM fuel cell,” *Electrochim. Acta*, vol. 54, no. 7, pp. 1992–1998, 2009, doi: 10.1016/j.electacta.2008.07.003.
- [35] S. Huang and C. Chang, “Promotion of Platinum-Ruthenium Catalyst for Electrooxidation of Methanol by Crystalline Ruthenium Dioxide,” *ChemPhysChem*, vol. 8, no. 12, pp. 1774–1777, 2007, doi: 10.1002/cphc.200700238.
- [36] H. A. Gasteiger, N. M. Markovic, and P. N. Ross, “H<sub>2</sub> and CO electrooxidation on well-characterized Pt, Ru, and Pt-Ru. 2. Rotating disk electrode studies of CO/H<sub>2</sub> mixtures at 62 °C,” *J. Phys. Chem.*, vol. 99, no. 45, pp. 16757–16767, 1995, doi: 10.1021/j100045a042.
- [37] P. N. Ross, K. Kinoshita, A. J. Scarpellino, and P. Stonehart, “Electrocatalysis on binary alloys II. Oxidation of of molecular hydrogen on supported Pt + Ru alloys,” *J Electroanal Chem*, vol. 63, pp. 97–110, 1975.
- [38] S. Jones, S. Jones, K. Tedsree, M. Sawangphruk, J. S. Foord, J. Fisher, D. Thompsett, S. Chi, E. Tsang, “Promotion of Direct Methanol Electro-oxidation by Ru Terraces on Pt by using a Reversed Spillover Mechanism,” *ChemCatChem*, vol. 2, no. 9, pp. 1089–1095, 2010, doi: 10.1002/cctc.201000106.
- [39] Y. Takasu, T. Kawaguchi, W. Sugimoto, and Y. Murakami, “Effects of the surface area of carbon support on the characteristics of highly-dispersed Pt-Ru particles as catalysts for

- methanol oxidation,” *Electrochim. Acta*, vol. 48, no. 25–26, pp. 3861–3868, 2003, doi: 10.1016/S0013-4686(03)00521-8.
- [40] T. Iwasita, H. Hoster, A. John-Anacker, W. F. Lin, and W. Vielstich, “Methanol oxidation on PtRu electrodes. Influence of surface structure and Pt-Ru atom distribution,” *Langmuir*, vol. 16, no. 2, pp. 522–529, 2000, doi: 10.1021/la990594n.
- [41] K. J. J. Mayrhofer, K. Hartl, V. Juhart, and M. Arenz, “Degradation of carbon-supported Pt bimetallic nanoparticles by surface segregation,” *J. Am. Chem. Soc.*, vol. 131, no. 45, pp. 16348–16349, 2009, doi: 10.1021/ja9074216.
- [42] S. Knights, S. Knights, R. Bashyam, P. He, M. Lauritzen, C. Startek, V. Colbow, J. Kolodziej, S. Wessel, “PEMFC MEA and System Design Considerations,” *ECS Meet. Abstr.*, vol. MA2011-02, no. 16, pp. 774–774, 2011, doi: 10.1149/ma2011-02/16/774.
- [43] J. H. Kim, Y. Y. Jo, E. A. Cho, J. H. Jang, H. J. Kim, T. Lim, I. Oh, J. J. Ko, I. J. Son, “Effects of Cathode Inlet Relative Humidity on PEMFC Durability during Startup – Shutdown Cycling II . Diagnostic Study,” *J. Electrochem. Soc.*, vol. 157, no. 5, pp. 633–642, 2010, doi: 10.1149/1.3327888.
- [44] Q. Lv, M. Yin, X. Zhao, C. Li, C. Liu, and W. Xing, “Promotion effect of TiO<sub>2</sub> on catalytic activity and stability of Pt catalyst for electrooxidation of methanol,” *J. Power Sources*, vol. 218, pp. 93–99, 2012, doi: 10.1016/j.jpowsour.2012.06.051.
- [45] S. Y. Huang, P. Ganesan, S. Park, and B. N. Popov, “Development of a titanium dioxide-supported platinum catalyst with ultrahigh stability for polymer electrolyte membrane fuel cell applications,” *J. Am. Chem. Soc.*, vol. 131, no. 39, pp. 13898–13899, 2009, doi: 10.1021/ja904810h.
- [46] R. Ganesan and J. S. Lee, “An electrocatalyst for methanol oxidation based on tungsten trioxide microspheres and platinum,” *J. Power Sources*, vol. 157, no. 1, pp. 217–221, 2006, doi: 10.1016/j.jpowsour.2005.07.069.
- [47] X. Cui, H. Zhang, X. Dong, H. Chen, L. Zhang, and J. Shi, “Electrochemical catalytic activity for the hydrogen oxidation of mesoporous WO<sub>3</sub> and WO<sub>3</sub>/C composites,” *J. Mater. Chem.*, vol. 30, pp. 3575–3580, 2008, doi: 10.1039/b806115g.
- [48] A. Bonnefont, F. Micoud, and M. Chatenet, “The role of the support in CO<sub>ads</sub> monolayer electrooxidation on Pt nanoparticles : Pt/WO<sub>x</sub> vs . Pt/C,” *Phys. Chem. Chem. Phys.*, no. 5, pp. 1182–1193, 2010, doi: 10.1039/b915244j.
- [49] F. Micoud, F. Maillard, A. Gourgaud, and M. Chatenet, “Unique CO-tolerance of Pt-WO<sub>x</sub> materials,” *Electrochem. commun.*, vol. 11, no. 3, pp. 651–654, 2009, doi: 10.1016/j.elecom.2009.01.007.
- [50] R. Fachini, G. Cruz, Y. Zhu, Y. Ishikawa, J. A. Colucci, and C. R. Cabrera, “Effect of Surface Composition of Electrochemically Codeposited Platinum/Molybdenum Oxide on Methanol Oxidation,” *J. Electrochem. Soc.*, vol. 148, pp. 222–226, 2001, doi: 10.1149/1.1349881.

- [51] R. Li, H. Hao, T. Huang, and A. Yu, "Electrodeposited Pd-MoO<sub>x</sub> catalysts with enhanced catalytic activity for formic acid electrooxidation," *Electrochim. Acta*, vol. 76, pp. 292–299, 2012, doi: 10.1016/j.electacta.2012.05.041.
- [52] Y. Takabatake, Z. Noda, S. M. Lyth, A. Hayashi, and K. Sasaki, "Cycle durability of metal oxide supports for PEFC electrocatalysts," *Int. J. Hydrogen Energy*, vol. 39, no. 10, pp. 5074–5082, 2014, doi: 10.1016/j.ijhydene.2014.01.094.
- [53] H. Zhang, C. Hu, X. He, L. Hong, G. Du, and Y. Zhang, "Pt support of multidimensional active sites and radial channels formed by SnO<sub>2</sub> flower-like crystals for methanol and ethanol oxidation," *J. Power Sources*, vol. 196, no. 10, pp. 4499–4505, 2011, doi: 10.1016/j.jpowsour.2011.01.030.
- [54] W. S. Baker, J. J. Pietron, M. E. Teliska, P. J. Bouwman, D. E. Ramaker, and K. E. Swiderlyons, "Enhanced Oxygen Reduction Activity in Acid by Tin-Oxide Supported Au Nanoparticle Catalysts," *J. Electrochem. Soc.*, vol. 153, no. 9, pp. 1702–1707, 2006, doi: 10.1149/1.2216527.
- [55] S. Sharma and B. G. Pollet, "Support materials for PEMFC and DMFC electrocatalysts - A review," *J. Power Sources*, vol. 208, pp. 96–119, 2012, doi: 10.1016/j.jpowsour.2012.02.011.
- [56] Z. M. Jarzebski and J. P. Marton, "Physical Properties of SnO<sub>2</sub> Materials I. Preparation and Defect Structure," *J. Electrochem. Soc.*, vol. 123, no. 7, pp. 199–205, 1976.
- [57] Z. M. Jarzebski and J. P. Marton, "Physical Properties of SnO<sub>2</sub> Materials II. Electrical Properties," *J. Electrochem. Soc.*, vol. 123, no. 9, pp. 299C–310C, 1976.
- [58] F. Ye, J. Li, T. Wang, Y. Liu, H. Wei, J. Li, X. Wang, "Electrocatalytic properties of platinum catalysts prepared by pulse electrodeposition method using SnO<sub>2</sub> as an assisting reagent," *J. Phys. Chem. C*, vol. 112, no. 33, pp. 12894–12898, 2008, doi: 10.1021/jp803188s.
- [59] T. Matsui, K. Fujiwara, T. Okanishi, R. Kikuchi, T. Takeguchi, and K. Eguchi, "Electrochemical oxidation of CO over tin oxide supported platinum catalysts," *J. Power Sources*, vol. 155, no. 2, pp. 152–156, 2006, doi: 10.1016/j.jpowsour.2005.05.003.
- [60] E. Antolini and E. R. Gonzalez, "Ceramic materials as supports for low-temperature fuel cell catalysts," *Solid State Ionics*, vol. 180, no. 9–10, pp. 746–763, 2009, doi: 10.1016/j.ssi.2009.03.007.
- [61] T. Takeguchi, Y. Anzai, R. Kikuchi, and K. Eguchi, "Preparation and Characterization of CO-Tolerant Pt and Pd Anodes Modified with SnO<sub>2</sub> Nanoparticles for PEFC," *J. Electrochem. Soc.*, vol. 154, no. 11, pp. 1132–1137, 2007, doi: 10.1149/1.2775161.
- [62] M. Nakada, A. Ishihara, S. Mitsushima, N. Kamiya, and K. I. Ota, "Effect of tin oxides on oxide formation and reduction of platinum particles," *Electrochem. Solid-State Lett.*, vol. 10, no. 1, pp. 4–7, 2007, doi: 10.1149/1.2382263.
- [63] P. Zhang, S. Huang, and B. N. Popov, "Mesoporous Tin Oxide as an Oxidation-Resistant

- Catalyst Support for Proton Exchange Membrane Fuel Cells,” *J. Electrochem. Soc.*, vol. 157, no. 8, pp. 1163–1172, 2010, doi: 10.1149/1.3442371.
- [64] T. Matsui, T. Okanishi, K. Fujiwara, K. Tsutsui, T. Takeguchi, K. Eguchi, T. Matsui, T. Okanishi, K. Fujiwara, K. Tsutsui, “Effect of reduction – oxidation treatment on the catalytic activity over tin oxide supported platinum catalysts,” *Sci. Technol. Adv. Mater.*, vol. 7, no. 6, pp. 524–530, 2006, doi: 10.1016/j.stam.2006.02.020.
- [65] A. Masao, S. Noda, F. Takasaki, K. Ito, and K. Sasaki, “Carbon-Free Pt Electrocatalysts Supported on SnO<sub>2</sub> for Polymer Electrolyte Fuel Cells,” *Electrochem. Solid-State Lett.*, vol. 12, no. 9, pp. 119–122, 2009, doi: 10.1149/1.3152325.
- [66] T. Daio, A. Staykov, L. Guo, J. Liu, M. Tanaka, Masaki, S. M. Lyth, K. Sasaki, “Lattice Strain Mapping of Platinum Nanoparticles on Carbon and SnO<sub>2</sub> Supports,” *Sci. Rep.*, vol. 5, pp. 1–10, 2015, doi: 10.1038/srep13126.
- [67] M. Dou, M. Hou, D. Liang, W. Lu, Z. Shao, and B. Yi, “SnO<sub>2</sub> nanocluster supported Pt catalyst with high stability for proton exchange membrane fuel cells,” *Electrochim. Acta*, vol. 92, pp. 468–473, 2013, doi: 10.1016/j.electacta.2013.01.070.
- [68] T. Okanishi, T. Matsui, T. Takeguchi, R. Kikuchi, and K. Eguchi, “Chemical interaction between Pt and SnO<sub>2</sub> and influence on adsorptive properties of carbon monoxide,” *Appl. Catal. A Gen.*, vol. 298, no. 1–2, pp. 181–187, 2006, doi: 10.1016/j.apcata.2005.09.035.
- [69] D. Wang, C. V. Subban, H. Wang, E. Rus, F. J. Disalvo, and H. D. Abruña, “Highly stable and CO-tolerant Pt/Ti<sub>0.7</sub>W<sub>0.3</sub>O<sub>2</sub> Electrocatalyst for proton-exchange membrane fuel cells,” *J. Am. Chem. Soc.*, vol. 132, no. 30, pp. 10218–10220, 2010, doi: 10.1021/ja102931d.
- [70] X. Cui, F. Cui, Q. He, L. Guo, M. Ruan, and J. Shi, “Graphitized mesoporous carbon supported Pt-SnO<sub>2</sub> nanoparticles as a catalyst for methanol oxidation,” *Fuel*, vol. 89, no. 2, pp. 372–377, 2010, doi: 10.1016/j.fuel.2009.09.006.
- [71] L. Jiang, L. Colmenares, Z. Jusys, G. Q. Sun, and R. J. Behm, “Ethanol electrooxidation on novel carbon supported Pt/SnO<sub>x</sub>/C catalysts with varied Pt:Sn ratio,” *Electrochim. Acta*, vol. 53, no. 2, pp. 377–389, 2007, doi: 10.1016/j.electacta.2007.01.047.
- [72] A. Sandoval-Gonzalez, E. Borja-Arco, J. Escalante, O. Jimenez-Sandoval, and S. A. Gamboa, “Methanol oxidation reaction on PtSnO<sub>2</sub> obtained by microwave-assisted chemical reduction,” *Int. J. Hydrogen Energy*, vol. 37, pp. 1752–1759, 2011, doi: 10.1016/j.ijhydene.2011.10.049.
- [73] D. F. Silva, A. N. Geraldes, A. Oliveira, E. S. Pino, M. Linardi, E. V. Spinacé, W. A. A. Macedo, J. D. Ardisson, “Preparation of PtSnO<sub>2</sub>/C electrocatalysts using electron beam irradiation,” *Mater. Sci. Eng.*, vol. 175, pp. 261–265, 2010, doi: 10.1016/j.mseb.2010.08.002.
- [74] L. Jiang, G. Sun, Z. Zhou, S. Sun, Q. Wang, S. Yan, H. Li, J. Tian, J. Guo, B. Zhou, Q. Xin, “Size-Controllable Synthesis of Monodispersed SnO<sub>2</sub> Nanoparticles and Application in Electrocatalysts,” *J. Phys. Chem. B*, vol. 109, pp. 8774–8778, 2005, doi: 10.1021/jp050334g.
- [75] E. Higuchi, K. Miyata, T. Takase, and H. Inoue, “Ethanol oxidation reaction activity of highly

- dispersed Pt/SnO<sub>2</sub> double nanoparticles on carbon black,” *J. Power Sources*, vol. 196, no. 4, pp. 1730–1737, 2011, doi: 10.1016/j.jpowsour.2010.10.008.
- [76] A. Bach Delpeuch, F. Maillard, M. Chatenet, P. Soudant, and C. Cremers, “Ethanol oxidation reaction (EOR) investigation on Pt/C, Rh/C, and Pt-based bi- and tri-metallic electrocatalysts: A DEMS and in situ FTIR study,” *Appl. Catal. B Environ.*, vol. 181, pp. 672–680, 2016, doi: 10.1016/j.apcatb.2015.08.041.
- [77] K. Ke and K. Waki, “Fabrication and Characterization of Multiwalled Carbon Nanotubes-Supported Pt/SnO<sub>x</sub> Nanocomposites as Catalysts for Electro-oxidation of Methanol,” *J. Electrochem. Soc.*, vol. 154, no. 3, pp. 207–212, 2007, doi: 10.1149/1.2426873.
- [78] M. Li, W. P. Zhou, N. S. Marinkovic, K. Sasaki, and R. R. Adzic, “The role of rhodium and tin oxide in the platinum-based electrocatalysts for ethanol oxidation to CO<sub>2</sub>,” *Electrochim. Acta*, vol. 104, pp. 454–461, 2013, doi: 10.1016/j.electacta.2012.10.046.
- [79] S. von Kraemer, K. Wikander, G. Lindbergh, A. Lundblad, and A. E. C. Palmqvist, “Evaluation of TiO<sub>2</sub> as catalyst support in Pt-TiO<sub>2</sub>/C composite cathodes for the proton exchange membrane fuel cell,” *J. Power Sources*, vol. 180, no. 1, pp. 185–190, 2008, doi: 10.1016/j.jpowsour.2008.02.023.
- [80] X. Liu, J. Chen, G. Liu, L. Zhang, H. Zhang, and B. Yi, “Enhanced long-term durability of proton exchange membrane fuel cell cathode by employing Pt/TiO<sub>2</sub>/C catalysts,” *J. Power Sources*, vol. 195, no. 13, pp. 4098–4103, 2010, doi: 10.1016/j.jpowsour.2010.01.077.
- [81] W. Vogel, L. Timperman, and N. Alonso-Vante, “Probing metal substrate interaction of Pt nanoparticles: Structural XRD analysis and oxygen reduction reaction,” *Appl. Catal. A Gen.*, vol. 377, no. 1–2, pp. 167–173, 2010, doi: 10.1016/j.apcata.2010.01.034.
- [82] A. Bauer, C. Song, A. Ignaszak, R. Hui, and J. Zhang, “Improved stability of mesoporous carbon fuel cell catalyst support through incorporation of TiO<sub>2</sub> Electrochimica Acta Improved stability of mesoporous carbon fuel cell catalyst support through inco,” *Electrochim Acta*, vol. 55, no. 28, pp. 8365–8370, 2010, doi: 10.1016/j.electacta.2010.07.025.
- [83] B. Abida, L. Chirchi, S. Baranton, T. W. Napporn, H. Kochkar, J. M. Léger, and A. Ghorbel, “Preparation and characterization of Pt/TiO<sub>2</sub> nanotubes catalyst for methanol electro-oxidation,” *Appl. Catal. B Environ.*, vol. 106, no. 3–4, pp. 609–615, 2011, doi: 10.1016/j.apcatb.2011.06.022.
- [84] X. L. Sui, Z. B. Wang, M. Yang, L. Huo, D. M. Gu, and G. P. Yin, “Investigation on C-TiO<sub>2</sub> nanotubes composite as Pt catalyst support for methanol electrooxidation,” *J. Power Sources*, vol. 255, pp. 43–51, 2014, doi: 10.1016/j.jpowsour.2014.01.001.
- [85] C. Marichy, G. Ercolano, G. Caputo, M. G. Willinger, D. Jones, and J. Rozi, “ALD SnO<sub>2</sub> protective decoration enhances the durability of a Pt based electrocatalyst †,” *J. Mater. Chem. A*, vol. 3, 2016, doi: 10.1039/C5TA08432F.
- [86] R. Li and X. Sun, “Composite of Pt – Ru supported SnO<sub>2</sub> nanowires grown on carbon paper for

- electrocatalytic oxidation of methanol,” *Electrochem. commun.*, vol. 9, pp. 2229–2234, 2007, doi: 10.1016/j.elecom.2007.06.032.
- [87] S. Sago, A. B. Suryamas, G. M. Anilkumar, T. Ogi, and K. Okuyama, “In situ growth of Pt nanoparticles on electrospun SnO<sub>2</sub> fibers for anode electrocatalyst application,” *Mater. Lett.*, vol. 105, pp. 202–205, 2013, doi: 10.1016/j.matlet.2013.04.007.
- [88] A. B. Suryamas, G. M. Anilkumar, S. Sago, T. Ogi, and K. Okuyama, “Electrospun Pt/SnO<sub>2</sub> nanofibers as an excellent electrocatalysts for hydrogen oxidation reaction with ORR-blocking characteristic,” *Catal. Commun.*, vol. 33, pp. 11–14, 2013, doi: 10.1016/j.catcom.2012.12.014.
- [89] C. V. Subban, Q. Zhou, A. Hu, T. E. Moylan, F. T. Wagner, and F. J. Disalvo, “Sol-gel synthesis, electrochemical characterization, and stability testing of Ti<sub>0.7</sub>W<sub>0.3</sub>O<sub>2</sub> nanoparticles for catalyst support applications in proton-exchange membrane fuel cells,” *J. Am. Chem. Soc.*, vol. 132, no. 49, pp. 17531–17536, 2010, doi: 10.1021/ja1074163.
- [90] V. T. T. Ho, C. J. Pan, J. Rick, W. N. Su, and B. J. Hwang, “Nanostructured Ti<sub>0.7</sub>Mo<sub>0.3</sub>O<sub>2</sub> support enhances electron transfer to Pt: High-performance catalyst for oxygen reduction reaction,” *J. Am. Chem. Soc.*, vol. 133, no. 30, pp. 11716–11724, 2011, doi: 10.1021/ja2039562.
- [91] T. T. Nguyen, V. T. T. Ho, C. J. Pan, J. Y. Liu, H. L. Chou, J. Rick, W. N. Su, and B. J. Hwang, “Synthesis of Ti<sub>0.7</sub>Mo<sub>0.3</sub>O<sub>2</sub> supported-Pt nanodendrites and their catalytic activity and stability for oxygen reduction reaction,” *Appl. Catal. B Environ.*, vol. 154–155, pp. 183–189, 2014, doi: 10.1016/j.apcatb.2014.02.018.
- [92] K. W. Park and K. S. Seol, “Nb-TiO<sub>2</sub> supported Pt cathode catalyst for polymer electrolyte membrane fuel cells,” *Electrochem. commun.*, vol. 9, no. 9, pp. 2256–2260, 2007, doi: 10.1016/j.elecom.2007.06.027.
- [93] S. Y. Huang, P. Ganesan, and B. N. Popov, “Electrocatalytic activity and stability of niobium-doped titanium oxide supported platinum catalyst for polymer electrolyte membrane fuel cells,” *Appl. Catal. B Environ.*, vol. 96, no. 1–2, pp. 224–231, 2010, doi: 10.1016/j.apcatb.2010.02.025.
- [94] S. T. Nguyen, Y. Yang, and X. Wang, “Ethanol electro-oxidation activity of Nb-doped-TiO<sub>2</sub> supported PdAg catalysts in alkaline media,” *Appl. Catal. B Environ.*, vol. 113–114, pp. 261–270, 2012, doi: 10.1016/j.apcatb.2011.11.046.
- [95] A. Kumar and V. Ramani, “Ta<sub>0.3</sub>Ti<sub>0.7</sub>O<sub>2</sub> Electrocatalyst Supports Exhibit Exceptional Electrochemical Stability,” *J. Electrochem. Soc.*, vol. 160, no. 11, pp. F1207–F1215, 2013, doi: 10.1149/2.038311jes.
- [96] X. Liu, X. Wu, and K. Scott, “Study of niobium and tantalum doped titania supported Pt electrocatalysts for methanol oxidation and oxygen reduction reactions,” *Catal. Sci. Technol.*, vol. 4, pp. 3891–3898, 2014, doi: 10.1039/C4CY00393D.
- [97] Y. Gao, M. Hou, Z. Shao, C. Zhang, X. Qin, and B. Yi, “Preparation and characterization of

- Ti<sub>0.7</sub>Sn<sub>0.3</sub>O<sub>2</sub> as catalyst support for oxygen reduction reaction,” *J. Energy Chem*, vol. 23, pp. 331–337, 2014.
- [98] Y. Y. Feng, W. Q. Kong, Q. Y. Yin, L. X. Du, Y. T. Zheng, and D. S. Kong, “Platinum catalysts promoted by in doped SnO<sub>2</sub> support for methanol electrooxidation in alkaline electrolyte,” *J. Power Sources*, vol. 252, pp. 156–163, 2014, doi: 10.1016/j.jpowsour.2013.12.008.
- [99] H. Tomonaga and T. Morimoto, “Indium-tin oxide coatings via chemical solution deposition,” *Thin Solid Films*, vol. 392, no. 2, pp. 243–248, 2001, doi: 10.1016/S0040-6090(01)01035-5.
- [100] C. Pan, Y. Li, Y. Ma, X. Zhao, and Q. Zhang, “Platinum-antimony doped tin oxide nanoparticles supported on carbon black as anode catalysts for direct methanol fuel cells,” *J. Power Sources*, vol. 196, no. 15, pp. 6228–6231, 2011, doi: 10.1016/j.jpowsour.2011.03.027.
- [101] K. S. Lee, I. S. Park, Y. H. Cho, D. S. Jung, N. Jung, H. Y. Park, and Y. E. Sung “Electrocatalytic activity and stability of Pt supported on Sb-doped SnO<sub>2</sub> nanoparticles for direct alcohol fuel cells,” *J. Catal.*, vol. 258, no. 1, pp. 143–152, 2008, doi: 10.1016/j.jcat.2008.06.007.
- [102] K. Kakinuma, M. Uchida, T. Kamino, H. Uchida, and M. Watanabe, “Synthesis and electrochemical characterization of Pt catalyst supported on Sn<sub>0.96</sub>Sb<sub>0.04</sub>O<sub>2-δ</sub> with a network structure,” *Electrochim. Acta*, vol. 56, no. 7, pp. 2881–2887, 2011, doi: 10.1016/j.electacta.2010.12.077.
- [103] H. L. Pang, X. H. Zhang, X. X. Zhong, B. Liu, X. G. Wei, Y. F. Kuang, and J. H. Chen, “Preparation of Ru-doped SnO<sub>2</sub>-supported Pt catalysts and their electrocatalytic properties for methanol oxidation,” *J. Colloid Interface Sci.*, vol. 319, no. 1, pp. 193–198, 2008, doi: 10.1016/j.jcis.2007.10.046.
- [104] K. Sasaki, F. Takasaki, and Z. Noda, “Alternative Electrocatalyst Support Materials for Polymer Electrolyte Fuel Cells Thermochemical stability of support materials,” *J. Electrochem. Soc.*, vol. 33, no. 1, pp. 473–482, 2010.
- [105] E. C. S. Transactions and T. E. Society, “Carbon-free Pt Electrocatalysts Supported on Doped SnO<sub>2</sub> for Polymer Electrolyte Fuel Cells F. Takasaki,” *J. Electrochem. Soc.*, vol. 25, no. 1, pp. 831–837, 2009.
- [106] K. Ravichandran and K. Thirumurugan, “Type Inversion and Certain Physical Properties of Spray Pyrolysed SnO<sub>2</sub>: Al Films for Novel Transparent Electronics Applications,” *J. Mater. Sci. Technol.*, vol. 30, no. 2, pp. 97–102, 2014, doi: 10.1016/j.jmst.2013.09.019.
- [107] T. Tsukatsune, Y. Takabatake, Z. Noda, T. Daio, A. Zaitso, S. M. Lyth, A. Hayashi, and K. S. Sasaki “Platinum-Decorated Tin Oxide and Niobium-Doped Tin Oxide PEFC Electrocatalysts: Oxygen Reduction Reaction Activity,” *J. Electrochemical Soc.*, vol. 161, no. 12, pp. 1208–1213, 2014, doi: 10.1149/2.0431412jes.
- [108] F. Takasaki, S. Matsuie, Y. Takabatake, Z. Noda, A. Hayashi, Y. Shiratori, K. Ito, F.

- Takasaki, S. Matsuie, Y. Takabatake, Z. Noda, A. Hayashi, and Y. Shiratori, “Carbon-Free Pt Electrocatalysts Supported on SnO<sub>2</sub> for Polymer Electrolyte Fuel Cells: Electrocatalytic Activity and Durability Carbon-Free Pt Electrocatalysts Supported on SnO<sub>2</sub> for Polymer Electrolyte Fuel Cells: Electrocatalytic Activity and Durability,” *J. Electrochemical Soc.*, vol. 158, no. 10, pp. 1270–1275, 2011, doi: 10.1149/1.3625918.
- [109] M. Torabi and S. K. Sadrezaad, “Electrochemical evaluation of nanocrystalline Zn-doped tin oxides as anodes for lithium ion microbatteries,” *J. Power Sources*, vol. 196, no. 1, pp. 399–404, 2011, doi: 10.1016/j.jpowsour.2010.06.028.
- [110] Y. Gu, C. Liu, Y. Li, X. Sui, K. Wang, and Z. Wang, “Ce<sub>0.8</sub>Sn<sub>0.2</sub>O<sub>2-δ</sub>-C composite as a co-catalytic support for Pt catalysts toward methanol electrooxidation,” *J. Power Sources*, vol. 265, pp. 335–344, 2014, doi: 10.1016/j.jpowsour.2014.04.137.
- [111] K. Zakrzewska, M. Radecka, and M. Rekas, “Effect of Nb, Cr, Sn additions on gas sensing properties of TiO<sub>2</sub> thin films,” *Thin Solid Films*, vol. 310, pp. 161–166, 1997.
- [112] Y. Li, C. Liu, Y. Liu, B. Feng, L. Li, H. Pan, W. Kellogg, D. Higgins, and G. Wu, “Sn-doped TiO<sub>2</sub> modified carbon to support Pt anode catalysts for direct methanol fuel cells,” *J. Power Sources*, vol. 286, pp. 354–361, 2015, doi: 10.1016/j.jpowsour.2015.03.155.
- [113] C. Wang, C. Shao, X. Zhang, and Y. Liu, “SnO<sub>2</sub> Nanostructures-TiO<sub>2</sub> Nanofibers Heterostructures: Controlled Fabrication and High Photocatalytic Properties,” *Inorg. Chem.*, no. 48, pp. 7261–7268, 2009, doi: 10.1021/ic9005983.
- [114] J. Li and H. C. Zeng, “Hollowing Sn-doped TiO<sub>2</sub> nanospheres via Ostwald ripening,” *J. Am. Chem. Soc.*, vol. 129, no. 51, pp. 15839–15847, 2007, doi: 10.1021/ja073521w.
- [115] S. L. Gojković, T. R. Vidaković, and D. R. Durović, “Kinetic study of methanol oxidation on carbon-supported PtRu electrocatalyst,” *Electrochim. Acta*, vol. 48, no. 24, pp. 3607–3614, 2003, doi: 10.1016/S0013-4686(03)00481-X.
- [116] G. Wu, L. Li, and B. Xu, “Effect of electrochemical polarization of PtRu/C catalysts on methanol electrooxidation,” *Electrochim. Acta*, vol. 50, pp. 1–10, 2004, doi: 10.1016/j.electacta.2004.07.006.
- [117] K. N. P. Kumar, D. J. Fray, J. Nair, F. Mizukami, and T. Okubo, “Enhanced anatase-to-rutile phase transformation without exaggerated particle growth in nanostructured titania-tin oxide composites,” *Scr. Mater.*, vol. 57, no. 8, pp. 771–774, 2007, doi: 10.1016/j.scriptamat.2007.06.039.
- [118] Y. Cao, T. He, L. Zhao, E. Wang, W. Yang, and Y. Cao, “Structure and phase transition behavior of Sn<sup>4+</sup>-doped TiO<sub>2</sub> nanoparticles,” *J. Phys. Chem. C*, vol. 113, no. 42, pp. 18121–18124, 2009, doi: 10.1021/jp9069288.
- [119] A. Sengele, D. Robert, N. Keller, C. Colbeau-Justin, and V. Keller, “Sn-doped and porogen-modified TiO<sub>2</sub> photocatalyst for solar light elimination of sulfure diethyle as a model for chemical warfare agent,” *Appl. Catal. B Environ.*, vol. 245, pp. 279–289, 2019, doi:

- 10.1016/j.apcatb.2018.12.071.
- [120] I. Rangel-Vázquez, G. Del Angel, V. Bertin, F. González, A. Vázquez-Zavala, A. Arrieta, J. M. Padilla, A. Barrera, and E. Ramos-Ramirez, "Synthesis and characterization of Sn doped TiO<sub>2</sub> photocatalysts: Effect of Sn concentration on the textural properties and on the photocatalytic degradation of 2,4-dichlorophenoxyacetic acid," *J. Alloys Compd.*, vol. 643, no. S1, pp. S144–S149, 2015, doi: 10.1016/j.jallcom.2014.12.065.
- [121] M. M. Oliveira, D. C. Schnitzler, and A. J. G. Zarbin, "(Ti,Sn)O<sub>2</sub> Mixed Oxides Nanoparticles Obtained by the Sol - Gel Route," *Chem. Mater*, vol. 15, pp. 1903–1909, 2003.
- [122] S. Mahanty, S. Roy, and S. Sen, "Effect of Sn doping on the structural and optical properties of sol-gel TiO<sub>2</sub> thin films," *J. Cryst. Growth*, vol. 261, no. 1, pp. 77–81, 2004, doi: 10.1016/j.jcrysgro.2003.09.023.
- [123] M. Afuyoni, G. Nashed, and I. M. Nasser, "TiO<sub>2</sub> doped with SnO<sub>2</sub> and studing its structural and electrical properties," *Energy Procedia*, vol. 6, pp. 11–20, 2011, doi: 10.1016/j.egypro.2011.05.002.
- [124] S. K. Kulshreshtha, R. Sasikala, and V. Sudarsan, "Non-random distribution of cations in Sn<sub>1-x</sub>Ti<sub>x</sub>O<sub>2</sub> (0.0 ≤ x ≤ 1.0): a <sup>119</sup>Sn MAS NMR study," *J. Mater. Chem*, vol. 11, pp. 930–935, 2001.
- [125] B. Sun, T. Shi, Z. Peng, W. Sheng, T. Jiang, and G. Liao, "Controlled fabrication of Sn/TiO<sub>2</sub> nanorods for photoelectrochemical water splitting," *Nanoscale Res. Lett.*, vol. 8, no. 1, pp. 1–8, 2013, doi: 10.1186/1556-276X-8-462.
- [126] L. B. Kong, J. Ma, and H. Huang, "Preparation of the solid solution Sn<sub>0.5</sub>Ti<sub>0.5</sub>O<sub>2</sub> from an oxide mixture via a mechanochemical process," *J. Alloys Compd.*, vol. 336, pp. 315–319, 2002.
- [127] P. R. Bueno, M. R. Cassia-Santos, L. G. P. Simoes, J. W. Gomes, and E. Longo, "Low-Voltage Varistor Based on (Sn,Ti)O<sub>2</sub> Ceramics," *J. Am. Ceram. Soc.*, vol. 85, no. 1, pp. 282–284, 2002.
- [128] F. D. Speck, M. T. Y. Paul, F. Ruiz-Zepeda, M. Gatalo, H. Kim, H. C. Kwon, K. J. J. Mayrhofer, M. Choi, C. H. Choi, N. Hodnik, and S. Cherevko, "Atomistic Insights into the Stability of Pt Single-Atom Electrocatalysts," *J. Am. Chem. Soc.*, vol. 142, no. 36, pp. 15496–15504, 2020, doi: 10.1021/jacs.0c07138.
- [129] Y. Cao, W. Yang, W. Zhang, G. Liu, and P. Yue, "Improved photocatalytic activity of Sn<sup>4+</sup> doped TiO<sub>2</sub> nanoparticulate films prepared by plasma-enhanced chemical vapor deposition," *New. J. Chem*, vol. 28, pp. 218–222, 2004.
- [130] Y. F. Tu, S. Y. Huang, J. P. Sang, and X. W. Zou, "Synthesis and photocatalytic properties of Sn-doped TiO<sub>2</sub> nanotube arrays," *J. Alloys Compd.*, vol. 482, no. 1–2, pp. 382–387, 2009, doi: 10.1016/j.jallcom.2009.04.027.
- [131] J. Yu, S. Liu, and M. Zhou, "Enhanced photocatalytic activity of hollow anatase microspheres by Sn<sup>4+</sup> incorporation," *J. Phys. Chem. C*, vol. 112, no. 6, pp. 2050–2057, 2008, doi: 10.1021/jp0770007.
- [132] Y. L. Wang, X. C. Jiang, Y. N. Xia, and A. Solution-phase, "Precursor route to polycrystalline

- SnO<sub>2</sub> nanowires that can be used for gas sensing under ambient conditions, J,” *Am. Chem. Soc.*, vol. 125, pp. 16176–16177, 2003.
- [133] X. Jiang, Y. Wang, and Y. Xia, “Ethylene glycol-mediated synthesis of metal oxide nanowires,” *J. Mater. Chem.*, vol. 4, pp. 695–703, 2004.
- [134] R. Sui, J. L. Young, and C. P. Berlinguette, “Sol – gel synthesis of linear Sn-doped TiO<sub>2</sub> nanostructures,” *J. Mater. Chem.*, vol. 3, pp. 498–503, 2010, doi: 10.1039/b915349g.
- [135] F. Fresno, D. Tudela, J. M. Coronado, M. Ferna, A. B. Hungri, and J. Soria, “Influence of Sn<sup>4+</sup> on the structural and electronic properties of Ti<sub>1-x</sub>Sn<sub>x</sub>O<sub>2</sub> nanoparticles used as photocatalysts,” *Phys. Chem. Chem. Phys.*, vol. 11, no. 58, pp. 2421–2430, 2006, doi: 10.1039/b601920j.
- [136] F. E. Oropeza, B. Davies, R. G. Palgrave, and R. G. Egdell, “Electronic basis of visible region activity in high area Sn-doped rutile,” *Phys. Chem. Chem. Phys.*, vol. 13, pp. 7882–7891, 2011, doi: 10.1039/c0cp02639e.
- [137] H. P. Naidu and A. B. Virkar, “Low-Temperature TiO<sub>2</sub>-SnO<sub>2</sub> Phase Diagram Using the Molten-Salt Method,” *J. Am. Ceram. Soc.*, vol. 81, pp. 2176–2180, 1998.
- [138] R. Long, Y. Dai, and B. Huang, “Geometric and Electronic Properties of Sn-Doped TiO<sub>2</sub> from First-Principles Calculations,” *J. Phys. Chem. C*, vol. 113, pp. 650–653, 2009.
- [139] D. Gubán, I. Borbáth, Z. Pászti, I. Sajó, E. Drotár, M. Hegedus, and A. Tompos, “Preparation and characterization of novel Ti<sub>0.7</sub>W<sub>0.3</sub>O<sub>2</sub>-C composite materials for Pt-based anode electrocatalysts with enhanced CO tolerance,” *Appl. Catal. B Environ.*, vol. 174–175, pp. 455–470, 2015, doi: 10.1016/j.apcatb.2015.03.031.
- [140] Vass, I. Borbáth, I. Bakos, Z. Pászti, I. E. Sajó, and A. Tompos, “Novel Pt Electrocatalysts: Multifunctional Composite Supports for Enhanced Corrosion Resistance and Improved CO Tolerance,” *Top. Catal.*, vol. 61, no. 12–13, pp. 1300–1312, 2018, doi: 10.1007/s11244-018-0988-0.
- [141] D. Gubán, Z. Pászti, I. Borbáth, I. Bakos, E. Drotár, I. Sajó, and A. Tompos, “Design and preparation of CO tolerant anode electrocatalysts for PEM fuel cells,” *Period. Polytech. Chem. Eng.*, vol. 60, no. 1, pp. 29–39, 2016, doi: 10.3311/PPch.8227.
- [142] I. Borbáth, K. Zelenka, Á. Vass, Z. Pászti, G. P. Szijjártó, Z. Sebestyén, Gy. Sáfrán, and A. Tompos, “CO tolerant Pt electrocatalysts for PEM fuel cells with enhanced stability against electrocorrosion,” *Int. J. Hydrogen Energy*, vol. 46, no. 25, pp. 13534–13547, 2021, doi: 10.1016/j.ijhydene.2020.08.002.
- [143] I. Borbáth, E. Tálas, Z. Pászti, K. Zelenka, I. Ayyubov, K. Salmanzade, I. E. Sajó, Gy. Sáfrán, and A. Tompos, “Investigation of Ti-Mo mixed oxide-carbon composite supported Pt electrocatalysts: Effect of the type of carbonaceous materials,” *Appl. Catal. A Gen.*, vol. 620, no. March, 2021, doi: 10.1016/j.apcata.2021.118155.
- [144] Á. Vass, I. Borbáth, Z. Pászti, I. Bakos, I. E. Sajó, P. Németh, and A. Tompos, “Effect of Mo incorporation on the electrocatalytic performance of Ti–Mo mixed oxide–carbon

- composite supported Pt electrocatalysts,” *React. Kinet. Mech. Catal.*, vol. 121, no. 1, pp. 141–160, 2017, doi: 10.1007/s11144-017-1155-5.
- [145] Á. Vass, I. Borbáth, I. Bakos, Z. Pászti, G. Sáfrán, and A. Tompos, “Stability issues of CO tolerant Pt-based electrocatalysts for polymer electrolyte membrane fuel cells: comparison of Pt/Ti<sub>0.8</sub>Mo<sub>0.2</sub>O<sub>2</sub>-C with PtRu/C,” *React. Kinet. Mech. Catal.*, vol. 126, no. 2, pp. 679–699, 2019, doi: 10.1007/s11144-018-1512-z.
- [146] D. Gubán, A. Tompos, I. Bakos, Á. Vass, Z. Pászti, E. Gy. Szabó, I. E. Sajó, and I. Borbáth, “Preparation of CO-tolerant anode electrocatalysts for polymer electrolyte membrane fuel cells,” *Int. J. Hydrogen Energy*, vol. 42, no. 19, pp. 13741–13753, 2017, doi: 10.1016/j.ijhydene.2017.03.080.
- [147] M. S. Yazici, S. Dursun, I. Borbáth, and A. Tompos, “Reformate gas composition and pressure effect on CO tolerant Pt/Ti<sub>0.8</sub>Mo<sub>0.2</sub>O<sub>2</sub>-C electrocatalyst for PEM fuel cells,” *Int. J. Hydrogen Energy*, vol. 46, no. 25, pp. 13524–13533, 2021, doi: 10.1016/j.ijhydene.2020.08.226.
- [148] N. Fairely, “CasaXPS Manual 2.3. 15,” *Casa Softw. Ltd*, pp. 1–177, 2009, [Online]. Available: <http://scholar.google.com/scholar?hl=en&btnG=Search&q=intitle:CasaXPS+Manual+2.3.15#2>
- [149] M. Mohai, “XPS MultiQuant: Multimodel XPS quantification software,” *Surf. Interface Anal.*, vol. 36, no. 8, pp. 828–832, 2004, doi: 10.1002/sia.1775.
- [150] M. Mohai, “XPS MultiQuant: Multi-model X-ray photoelectron spectroscopy quantification program.” 2011.
- [151] C. D. Wagner, A. V. Naumkin, A. Kraut-Vass, J. W. Allison, C. J. Powell, and J. R. R. Jr, “NIST X-ray Photoelectron Spectroscopy Database.” National Institute of Standards and Technology, Gaithersburg, MD, 2003. [Online]. Available: <http://srdata.nist.gov/xps/>
- [152] J. F. Moulder, W. F. Stickle, P. E. Sobol, and K. D. Bombe, *Handbook of X-ray Photoelectron Spectroscopy*. Minnesota, USA: Perkin-Elmer Corp. Eden Prairie, 1992.
- [153] T. Takayuki, “Electrochemistry & Spectroelectrochemistry,” 2022.
- [154] L. B. Vian and E. G. Ciapina, “Free software for the determination of the real surface area of Fuel Cell electrocatalysts.” São Paulo State University (UNESP), School of Engineering, Guaratinguetá, SP, Brazil.
- [155] K. J. J. Mayrhofer, D. Strmcnik, B. B. Blizanac, V. Stamenkovic, M. Arenz, and N. M. Markovic, “Measurement of oxygen reduction activities via the rotating disc electrode method: From Pt model surfaces to carbon-supported high surface area catalysts,” *Electrochim. Acta*, vol. 53, no. 7, pp. 3181–3188, 2008, doi: 10.1016/j.electacta.2007.11.057.
- [156] R. Woods, *Electroanalytical chemistry: a series of advances*, vol. 9. Marcell Dekker, New York, 1976.
- [157] K. Shinozaki, J. W. Zack, R. M. Richards, B. S. Pivovar, and S. S. Kocha, “Oxygen Reduction Reaction Measurements on Platinum Electrocatalysts Utilizing Rotating Disk Electrode Technique,” *J. Electrochem. Soc.*, vol. 162, no. 10, pp. F1144–F1158, 2015, doi:

10.1149/2.1071509jes.

- [158] K. J. J. Mayrhofer, "Oxygen Reduction and Carbon Monoxide Oxidation on Pt - from Model to Real Systems for Fuel Cell Electrocatalysis," Vienna University of Technology, 2006.
- [159] A. Brew, *Electrochemical studies of the oxygen reduction reaction: platinum and platinum bimetallic single crystal electrodes*. Cardiff, 2015. [Online]. Available: [https://orca.cf.ac.uk/88050/1/Brew A Final PhD Thesis.pdf](https://orca.cf.ac.uk/88050/1/Brew%20A%20Final%20PhD%20Thesis.pdf)
- [160] A. J. Bard and L. R. Faulkner, *Electrochemical Methods Fundamentals and Applications.*, New York: Department of Chemistry and Biochemistry: University of Texas at Austin, 2001.
- [161] I. Bakos, I. Borbáth, Á. Vass, Z. Pászti, and A. Tompos, "Design and investigation of molybdenum modified platinum surfaces for modeling of CO tolerant electrocatalysts," *Top Catal*, vol. 61, pp. 1385–1395, 2018.
- [162] P. M. Kleszyk, *Rapid screening of Proton Exchange Membrane Fuel Cell Cathode Catalysts*. Southampton, 2009.
- [163] A. R. Mitchell and R. H. Parker, "The Reduction of SnO<sub>2</sub> and Fe<sub>2</sub>O<sub>3</sub> by Solid Carbon," *Miner. Eng.*, vol. 1, no. 1, pp. 53–66, 1988.
- [164] D. Pantea, H. Darmstadt, S. Kaliaguine, and C. Roy, "Electrical conductivity of conductive carbon blacks: Influence of surface chemistry and topology," *Appl. Surf. Sci.*, vol. 217, no. 1–4, pp. 181–193, 2003, doi: 10.1016/S0169-4332(03)00550-6.
- [165] M. Carmo, A. R. dos Santos, J. G. R. Poco, and M. Linardi, "Physical and electrochemical evaluation of commercial carbon black as electrocatalysts supports for DMFC applications," *J. Power Sources*, vol. 173, no. 2 SPEC. ISS., pp. 860–866, 2007, doi: 10.1016/j.jpowsour.2007.08.032.
- [166] S. P. S. Porto, P. A. Fleury, and T. C. Damen, "Raman spectra of TiO<sub>2</sub>, MgF<sub>2</sub>, ZnF<sub>2</sub>, FeF<sub>2</sub>, and MnF<sub>2</sub>," *Phys. Rev.*, vol. 154, no. 2, pp. 522–526, 1967, doi: 10.1103/PhysRev.154.522.
- [167] A. C. Ferrari and J. Robertson, "Interpretation of Raman spectra of disordered and smorphous carbon," *Phys. Rev. B*, vol. 61, no. 20, p. 14095, 2000, doi: 10.1007/BF02543692.
- [168] K. N. Kudin, B. Ozbas, H. C. Schniepp, R. K. Prud'homme, I. A. Aksay, and R. Car, "Raman spectra of graphite oxide and functionalized graphene sheets," *Nano Lett.*, vol. 8, no. 1, pp. 36–41, 2008, doi: 10.1021/nl071822y.
- [169] Z. Tian, C. Liu, Q. Li, J. Hou, Y. Li, and S. Ai, "Nitrogen- and oxygen-functionalized carbon nanotubes supported Pt-based catalyst for the selective hydrogenation of cinnamaldehyde," *Appl. Catal. A Gen.*, vol. 506, pp. 134–142, 2015, doi: 10.1016/j.apcata.2015.08.023.
- [170] F. Tuinstra and J. L. Koenig, "Raman Spectrum of Graphite," *J. Chem. Phys.*, vol. 53, no. 1126, 1970, doi: 10.1063/1.1674108.
- [171] D. Diczházi, I. Borbáth, I. Bakos, G. P. Szijjártó, A. Tompos, and Z. Pászti, "Design of Mo-doped mixed oxide–carbon composite supports for Pt-based electrocatalysts: the nature of the Mo-Pt interaction," *Catal. Today*, vol. 366, pp. 31–40, 2021, doi:

- 10.1016/j.cattod.2020.04.004.
- [172] F. Maillard, S. Schreier, M. Hanzlik, E. R. Savinova, S. Weinkauf, and U. Stimming, “Influence of particle agglomeration on the catalytic activity of carbon-supported Pt nanoparticles in CO monolayer oxidation,” *Phys. Chem. Chem. Phys.*, pp. 375–383, 2005, doi: 10.1039/b411377b.
- [173] I. Borbáth, D. Gubán, I. Bakos, Z. Pászti, G. Gajdos, I. E. Sajó, Á. Vass, and A. Tompos, “Exclusive formation of alloy phases via anchoring technique—From bimetallic catalysts to electrocatalysis,” *Catal. Today*, vol. 306, pp. 58–70, 2018, doi: 10.1016/j.cattod.2017.01.011.
- [174] T. N. Geppert, M. Bosund, M. Putkonen, B. M. Stühmeier, A. T. Pasanen, P. Heikkilä, H. A. Gasteiger, and H. A. El-Sayed, “HOR Activity of Pt-TiO<sub>2</sub>-Y at Unconventionally High Potentials Explained: The Influence of SMSI on the Electrochemical Behavior of Pt,” *J. Electrochem. Soc.*, vol. 167, no. 8, p. 084517, 2020, doi: 10.1149/1945-7111/ab90ae.
- [175] M. Eckardt, C. Gebauer, Z. Jusys, M. Wassner, N. Hüsing, and R. J. Behm, “Oxygen reduction reaction activity and long-term stability of platinum nanoparticles supported on titania and titania-carbon nanotube composites,” *J. Power Sources*, vol. 400, no. August, pp. 580–591, 2018, doi: 10.1016/j.jpowsour.2018.08.036.